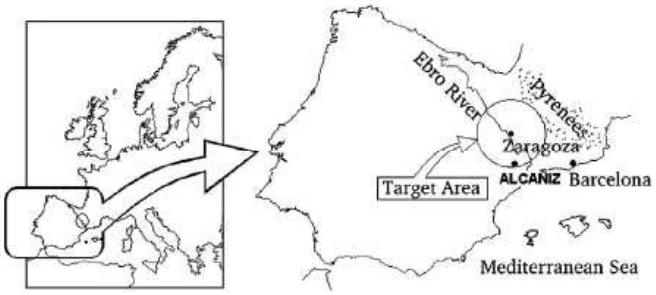

Figure 4.1.1: Target area

Font (1983), basing his studies on the analysis of maps on a synoptic scale, attributes the development of thunderstorms to the release of latent instability by strong surface heating. This author claims that the topography plays a fundamental role in this development when there is cold air at medium and high tropospheric levels. However, more recent studies including numerical simulations of a mesoscale system, such as the one carried out by Ramis et al. (1999), demonstrate the importance of a thermal mesolow in a hail event in Catalonia. A similar mesoscale structure was the triggering factor in the catastrophic flash flood over the Spanish Pyrenees in the summer of 1996 (Romero et al., 2001). Tudurí et al. (2003) also conclude that the presence of a mesolow of thermal origin is a fundamental factor in the development of a chain of hailstorms in the Ebro Valley in the summer of 2001.

4.1.1 Extreme hail event on August 16th 2003

The impacts and sensitivities of these kind of phenomenas are examined in the August 16th 2003 severe hail event occurred in the town of Alcañiz in the Ebro Valley in Spain (García-Ortega et al., 2007). This storm brought with it intense rain and hail precipitation that caused severe floods, damaged cars and street furniture. On August 16th 2003, between 1525 and 1820 UTC, a severe storm broke over the town of Alcañiz (41.02° N, 0.08° W), province of Teruel (in the Ebro Valley, figure 4.1.1). Rain gauges registered a maximum accumulated precipitation of 115 mm in slightly over 3 h. Within this time span, an intense hail fall affected the town and its surroundings for over half an hour, and hailstones of up to 12 cm were registered. Satellite images (not shown) provided information of the storms which originated over the Central part of the Ebro Valley and the existence of a mesoscale convective system generated over the Alborán Sea (southern part of the Spanish Mediterranean coast) that moved northwards. A C-band radar with a high time resolution was used to follow up the horizontal and vertical structure of the storm.

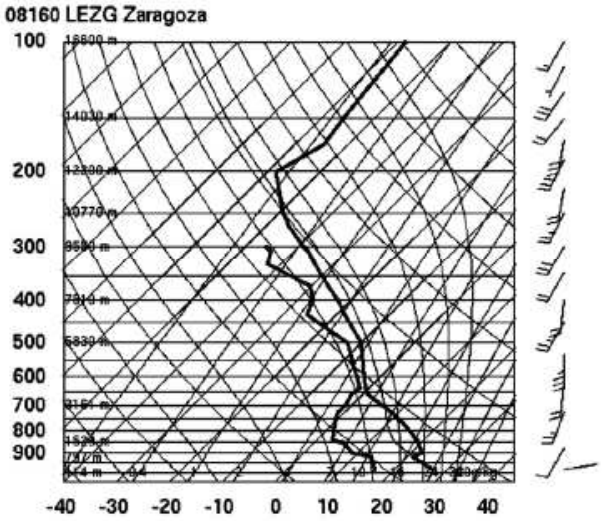

Figure 4.1.2: Skew-T plot of the Zaragoza sounding on 16th August 2003 at 12^{00} UTC

Observations

Infrared images from Meteosat show that by 10^{30} UTC a convective cloud mass started developing in the Central Ebro Valley, moving from NW to SE. Between 15^{30} and 18^{30} UTC the satellite images confirm that the cloud top temperature of the air mass over Alcañiz was between -60 and -65 $^{\circ}C$. The cloud band associated with this air mass was subsequently pushed northwards by mid and high tropospheric winds, causing small disperse storms in the Pyrenees in the late evening. The 12^{00} UTC sounding in Zaragoza (figure 4.1.2) registered winds from the south at mid and high tropospheric levels. There is also a layer of instability in the lower first meters, and an area of conditional instability around 925 hPa, just before a layer of stability at 900 hPa. The Convective Available Potential Energy (CAPE) reveals favourable conditions for convective developments, going from 161.4 Jkg^{-1} at 00^{00} UTC to 672.5 Jkg^{-1} at 12^{00} UTC. In this same time interval, the Lifted Index went from -0.82 to -1.46.

A C-band radar with a high time resolution was installed close to Zaragoza, about 100 km from Alcañiz. This radar provided information on the horizontal and vertical structure of the storm with a spatial resolution of 1 km. The radar images show that the storm originated at approximately 15^{25} UTC. The radar echoes were almost stationary, indicating that the storm moved very little during its active life. At 15^{40} UTC, the maximum reflectivity factor of the storm reached 48 dBZ at an altitude of 11,000 MSL, with an echo top of 18 km. These values remained nearly unchanged for about an hour. At approximately 16^{50} UTC, the intensity of the storm decreased, but from 17^{10} UTC the storm gained renewed intensity, with a maximum reflectivity factor, Zmax, between 42

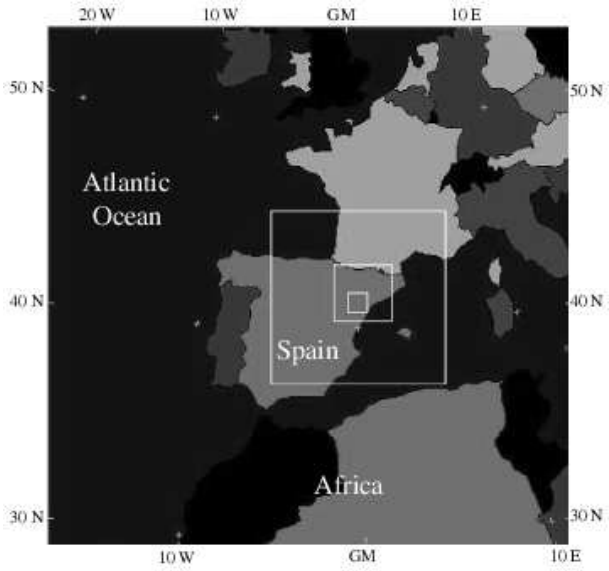

Figure 4.1.3: The four domains used for numerical simulations

and 47 dBZ until 17^{40} UTC, when the storm started dwindling until it was completely dispersed by 18^{30} UTC. Rain gauges in Alcañiz registered a maximum accumulated precipitation of 115 mm in just over 3 h. In this time there was an intense hail fall in Alcañiz that lasted over half an hour, with hailstones between 5 and 12 cm.

4.1.2 Sensitivity to orography and solar radiation

A number of numerical simulations were carried out in four domains that include synoptic, and mesoscales. The first aim of this study was to test whether or not the model could represent the conditions in which the severe storm in Alcañiz occurred, at both synoptic and mesoscale. Furthermore, it aims at studying whether or not the simulation at a higher resolution is capable of reproducing the event well enough. The information provided by the radar has been essential in order to locate the storm in time and space, and thus establish a comparison with the output of the model. Finally, the importance of topography and solar radiation has been studied in relation with the origin of this particular severe storm, considering not only their individual relevance, but also the contribution of the combination of both factors in locating the storm in time and space.

Four 151 × 151 grid domains, using Lambert's conformal projection, were set up to obtain the highest resolution over the area of interest (figure 4.1.3). The coarse domain has a resolution of 18 km, covering western Mediterranean areas, eastern mid-latitude Atlantic areas and the north of Africa (domain 1). The three other nested domains (do-

mains 2, 3 and 4) are centred in the study area with a resolution of 6, 2 and 0.67 km, respectively. Vertically, 23 terrain-following-levels have been considered. The model output intervals used are 6, 3, 1 and 0.5 h, respectively. The four domains interact with each other through a two-way nesting strategy. Initial and boundary conditions for the coarse domain a reconstructed from the analysis of the ECMWF. The source data of the 25-category classified global coverage USGS (see table 2.1.b). As for the period of time covered by the experiments, a 36-h long simulation was performed, from August 16th at 00^{00} UTC to August 17th at 12^{00} UTC, to ensure a stable behaviour of the model during the time of the storm.

MM5v3 simulations were performed with the Kain-Fritsch convective parameterisation scheme was used for domain 1. In domains 2, 3 and 4, no convective scheme has been introduced and convective processes are fully explicit simulated with the primitive model equations. The moisture scheme used was the Reisner graupel scheme, the parameterisation scheme used to represent the planetary boundary layer processes is the MRF scheme (see section 2.1.1 for a better explanation).

Model validation and diagnosis

The numerical study requires a control run that reproduces closely the observed meteorological aspects of the event. The model simulation must reproduce the observations for a run to be considered useful, keeping in mind the difficulty involved in achieving accuracy in the results when simulating an event on a convective scale with four domains, with the smallest one having a grid domain of only 0.67 km.

The simulation results show that the model reproduced reasonably well the evolution on a synoptic scale of the domains observed in the ECMWF analysis at all tropospheric levels. The simulation in domain 1 (left panel in figure 4.1.4) shows that at 300 hPa and at 12^{00} UTC there is a trough over the Iberian Peninsula with a low over Galicia moving eastward until 18^{00} UTC. As a result, an upper-level flow from SSW is found over the study zone. A similar topography is observed at 500 hPa, with a cold air mass affecting the region of Aragón and the Mediterranean coast, with temperatures below -12 °C to the east of the geopotential trough moving eastward (right panel in figure 4.1.4). This cold air mass has to be taken into account, as it will cause increasing instability before the trough arrives.

On the other hand, left panel in figure 4.1.5 shows a strong temperature gradient over the Iberian Peninsula at 850 hPa moving NWSE, with temperatures from 10 °C in the north Atlantic coast of Galicia to 19 °C in the Mediterranean coast, with a maximum of 22 °C to the south of Alcañiz. Right panel in figure 4.1.5 corresponds to domain 2 and shows a thermal mesolow at 12^{00} UTC over the Central Ebro Valley. This low becomes

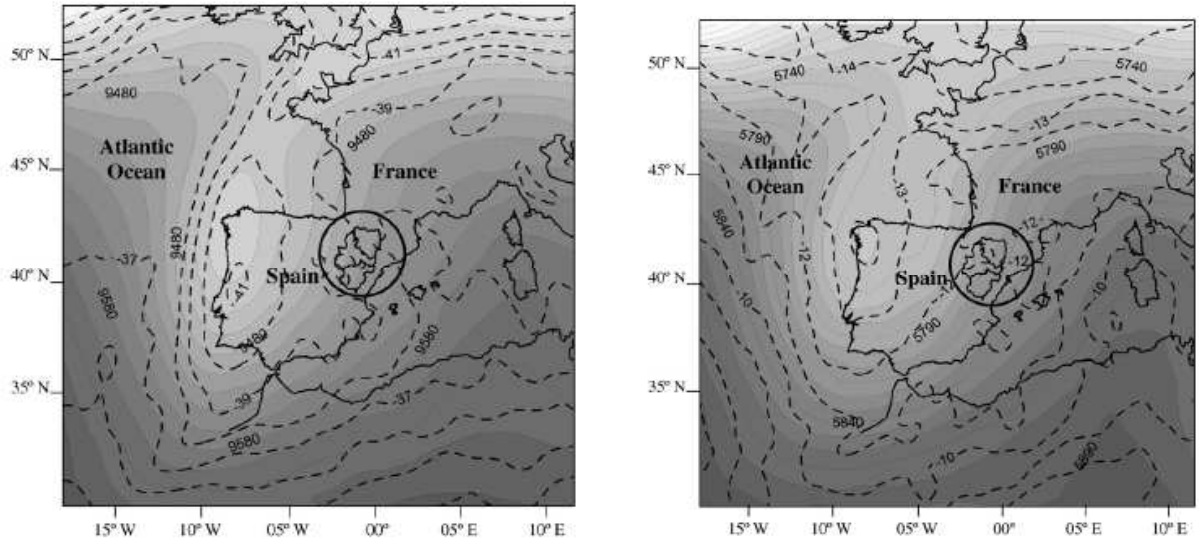

Figure 4.1.4: Left panel: Geopotential height (gpm, shaded areas) and temperature (°C, dashed line) at 300 hPa at 12^{00} UTC on 16th August 2003, as simulated by the model (domain 1). Right panel: Geopotential height (gpm, shaded areas) and temperature (°C, dashed line) at 500 hPa at 12^{00} UTC on 16th August 2003, as simulated by the model (domain 1). The circle comprises the area of study

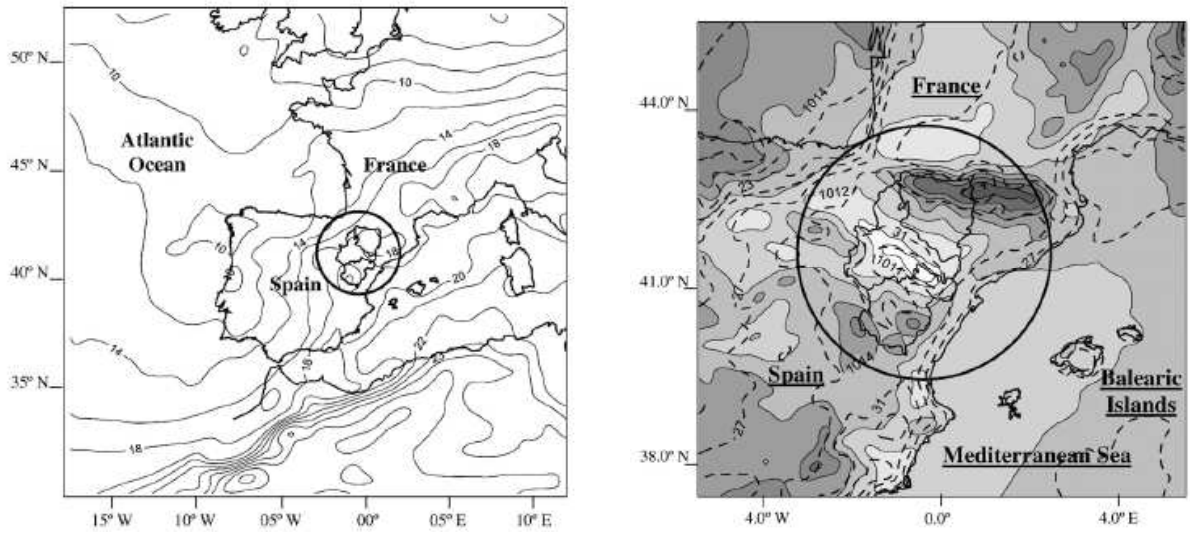

Figure 4.1.5: Left panel: Temperature (°C) at 850 hPa at 12^{00} UTC on 16th August 2003, as simulated by the model (domain 1). Right panel: Sea level pressure (hPa, shaded) and surface temperature (°C, dashed line) at 12^{00} UTC on 16th August 2003, as simulated by the model (domain 2). The circle comprises the area of study

more marked in the study zone. The figure highlights that the area of Alcañiz registers temperatures of over 31 °C. Between 12^{00} and 15^{00} UTC there is a strong increase in the relative surface humidity in the study zone (not shown), soaring from 40% to over 75%. Left panel in figure 4.1.6 corresponds to domain 3 and shows the surface wind field from the Mediterranean Sea entering the Ebro Valley, and reaching Alcañiz by 12^{00} UTC. This wind field associated with the thermal mesolow supplies warm air from the Mediterranean Sea, which had in those days temperatures higher than average in that time of the year, with a high content of water vapour. The surface inflow, the convergence area shown in figure 4.1.6 (left panel) around Alcañiz, and the thermal mesolow, overlapping on a favourable synoptic environment, with a deep trough and a cold front arriving from NW, are enough to trigger convection.

Figure 4.1.6 also shows the total precipitation field. This field comprises, on the one hand, the northern part of the domain until the Pyrenees, and on the other hand, the Ebro Valley near Alcañiz. The shaded areas over Alcañiz indicate the highest intensity in precipitation. As far as precipitation in the Pyrenees is concerned, there were some isolated storms, but the radar range and the mountainous profile of this area have hindered the gathering of additional information about this fact. If we compare the results of the simulation with the actual study zone, according to the radar data (right panel figure

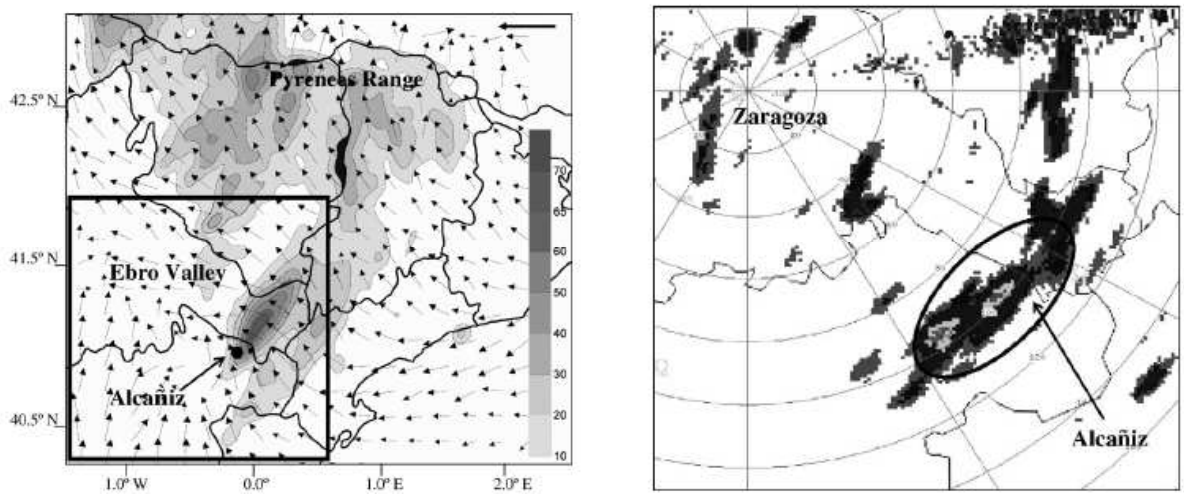

Figure 4.1.6: Left panel: Simulated surface wind field at 12^{00} UTC. Arrow on upper right-hand corner corresponds to 12 $ms{-}^{1}$. Simulated precipitation field (control simulation) recorded from 00^{00} UTC to 19^{00} UTC on 16th August 2003. Precipitation is in mm (domain 3). The box in the lower left is shown enlarged in right panel. Left panel: Accumulated precipitation areas provided by the C-band radar in Zaragoza recorded from 00^{00} UTC to 19^{00} UTC on 16th August 2003. The highlighted area indicates the zone affected by the severe storm

4.1.6) it may be stated that the simulation reproduces quite closely the area affected by the severe storm. The point that establishes the maximum precipitation estimated by the radar moves only 15 km to the SW of the maximum precipitation point, according to the model. However, the maximum precipitation recorded by the rain gauges in Alcañiz was 115 mm, whereas the model gives a maximum precipitation value of 85 mm.

In addition, the model simulates reasonably well the environment and the convective activity causing the severe hail event in the area of Alcañiz. The model locates very precisely the area with the most intense precipitation, although it underestimates the amount registered. Taking into account that the present study is focused on one single severe storm, and considering the difficulty of reproducing these events on a convective scale, the results found are so satisfactory that a more in-depth analysis of the causes of the event will be done, using this simulation as a control simulation for a sensitivity study.

Radar vs. simulation

The radar was simulated on domain 4 between 15^{30} and 18^{30} UTC to analyse whether or not the model was capable of reproducing the spatial and temporal evolution of the storm. Radar data are supplied every 3.5 min approximately, while the model output interval in domain 4 is 30 min. Because of this, a statistical comparison was carried out. The average values of the radar reflectivity factor were calculated at intervals of 30 min, and the data were compared to the simulation of the radar reflectivity factor averaged every 30 min.

In reference to spatial evolution, it is interesting to observe (figures 4.1.7 to 4.1.11) that there is quite a high degree of similarity. Between 15^{30} and 17^{00} UTC the radar shows how the storm moves slowly towards the NE. The same behaviour is observed in the simulation.

The radar images show that around 17^{00} UTC the storm starts dissipating in its central and northeastern parts, whereas the southwest regains activity, although to a smaller extent. Similarly, the simulation shows a decrease in the intensity of the storm, followed by a renewed activity in the SW of domain 4. The intensity of this new nucleus increases between 17^{00} and 17^{30} (figure 4.1.10).

The most intense hail event occurred between 16^{00} and 16^{30} UTC. The maximum value of the maximum radar reflectivity factor, $Zmax = 54dBZ$, was registered at 16^{13} UTC (not shown). The simulation shows that the intensity of the storm reaches its maximum values between 16^{00} and 16^{30} UTC, coinciding with the data from the radar.

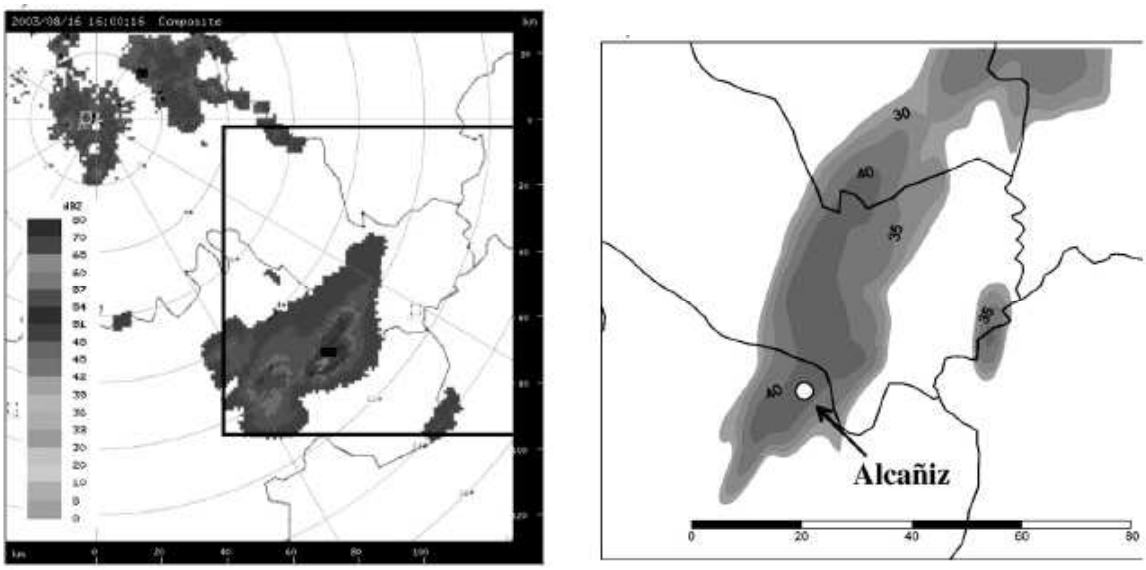

Figure 4.1.7: Composite reflectivity factor (dBZ, according to the scale) provided by the radar at 16^{00} UTC. b) Zoom to the box in figure 4.1.7a showing the simulated reflectivity factor averaged between 15^{30} and 16^{00} UTC (domain 4)

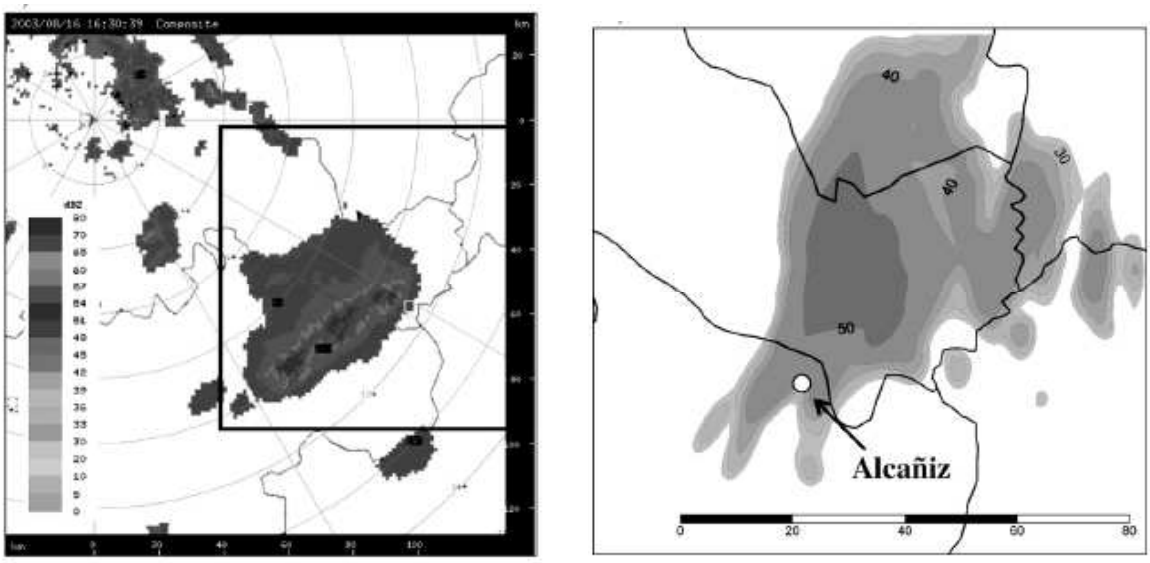

Figure 4.1.8: The same as in figure 4.1.7, but at time radar 16^{30} UTC and zoomed averaged reflectivity between 16^{00} and 16^{30} UTC

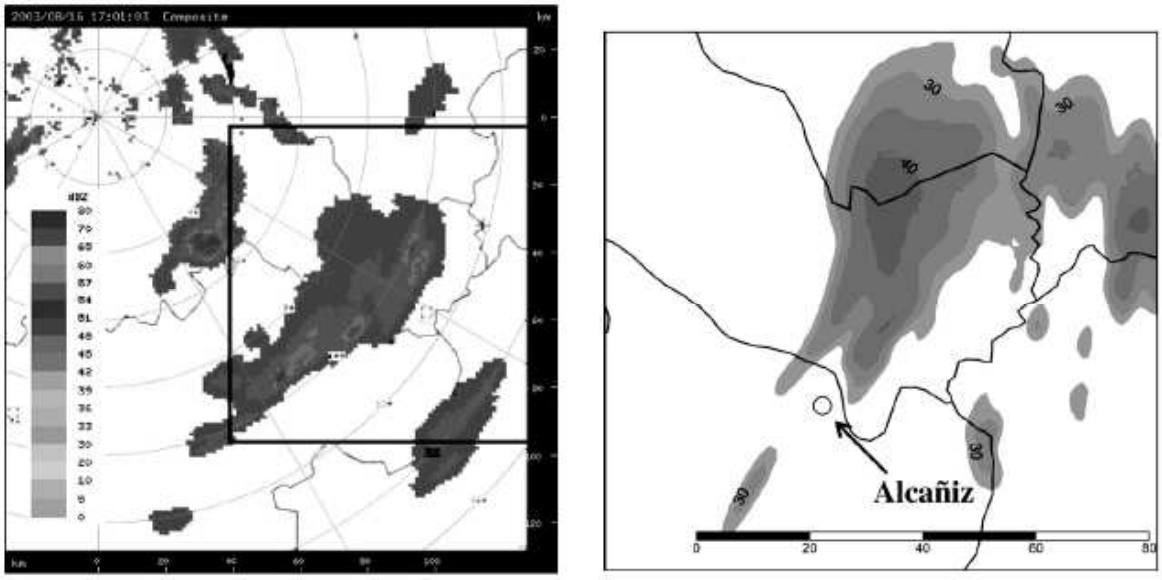

Figure 4.1.9: The same as in figure 4.1.7, but at time radar 17^{00} UTC and zoomed averaged reflectivity between 16^{30} and 17^{00} UTC

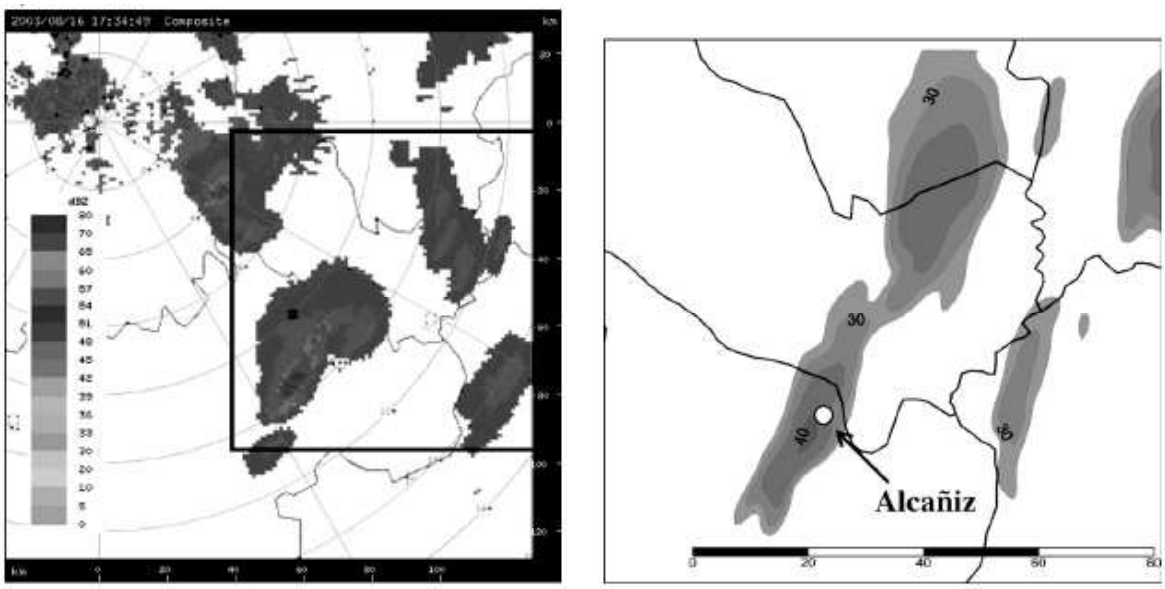

Figure 4.1.10: The same as in figure 4.1.7, but at time radar 17^{30} UTC and zoomed averaged reflectivity between 17^{00} and 17^{30} UTC

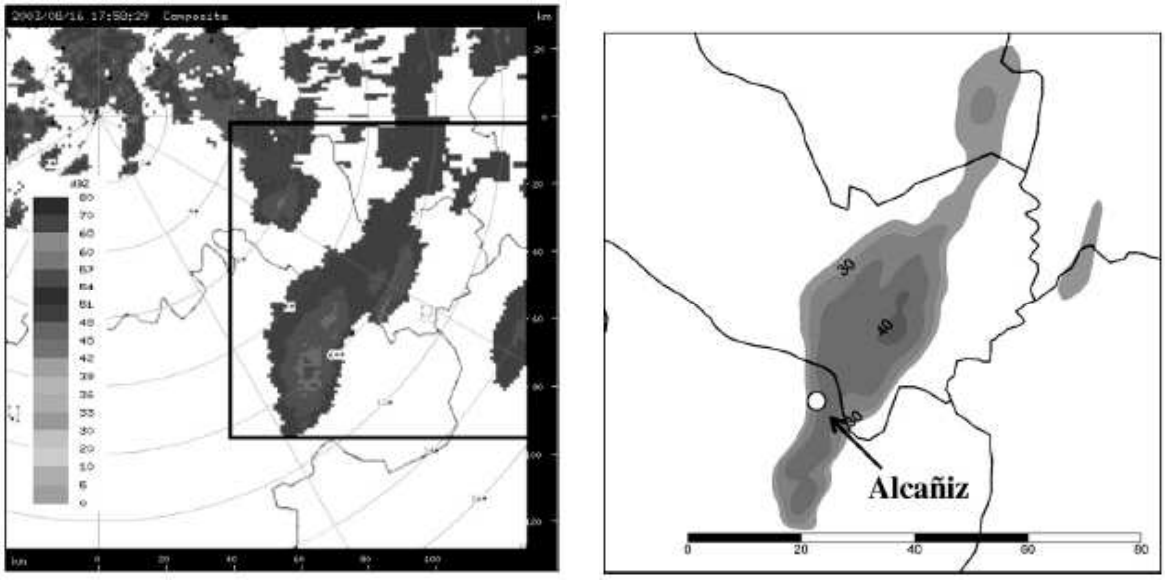

Figure 4.1.11: The same as in figure 4.1.7, but at time radar 18^{00} UTC and zoomed averaged reflectivity between 17^{30} and 18^{00} UTC

Sensitivity experiments

Once the most relevant synoptic and mesoscale-scale components in the development of the episode have been diagnosed, and once the satisfactory performance of the model in the simulation of the storm has been confirmed, it would be interesting to determine which factor has the strongest impact on the formation of the storm.

As mentioned above, the occurrence of a thermal mesolow is a feature common to various cases of severe convective phenomena studied in the Ebro Valley, and it was also present in the storm in Alcañiz. The peculiar topography of Alcañiz, to the south of a valley that forms a corridor to the Mediterranean Sea between the Pyrenees and the Iberian Mountains, fosters the inflow of warm and humid air from the sea and the lifting of low-level parcels. In other words, the topography induces changes in the low-tropospheric wind field. The high temperatures of the summer (solar radiation) influence the development of the thermal mesolow and play a fundamental role in the convective episode. These two factors, solar radiation (factor 1) and topography (factor 2), have been studied with respect to the effects they may have on the formation of the mesolow, as well as on the spatial distribution and the intensity of the precipitation.

The factor separation technique by (Stein and Albert, 1993) has been used in order to determine the quantitative of these effects (See section 2.3).

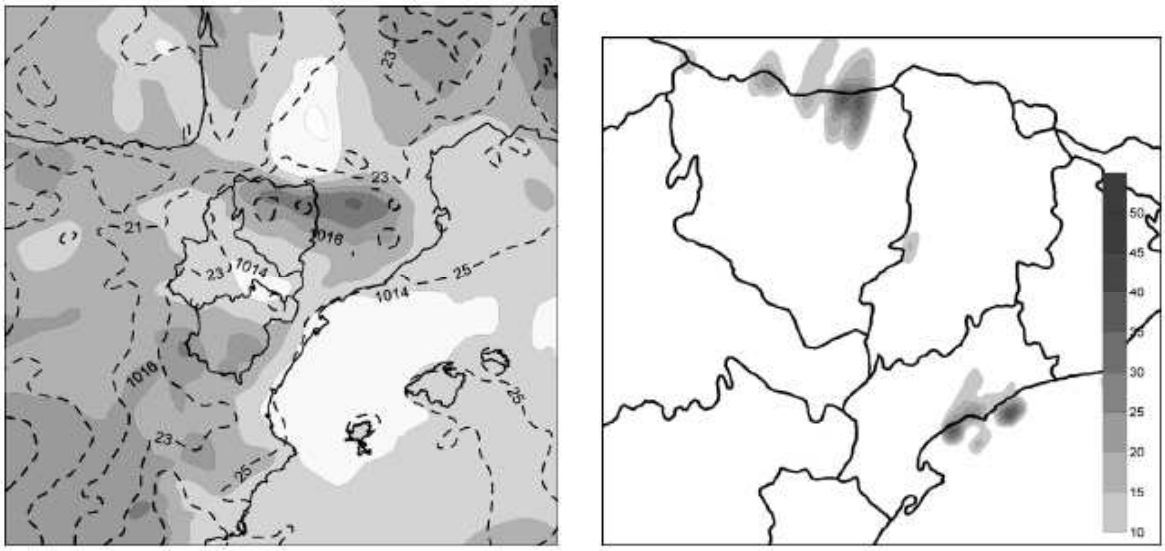

Figure 4.1.12: Left panel: Sea level pressure (hPa, shaded) and surface temperature (°C) at 12^{00} UTC on 16th August 2003, as simulated by the no-radiation experiment S2 (domain 2). Right panel: Simulated precipitation field induced by terrain (e_2) from 00^{00} UTC to 19^{00} UTC on 16th August 2003. Precipitation is in mm (domain 3)

The experiment with neither solar radiation nor topography S0 (not shown) shows no precipitation at all in Northeastern Spain, with only a maximum of 10 mm in a very small area over the Mediterranean Sea.

If solar radiation is left out (experiment S2, left panel in figure 4.1.12), the mesolow is less intense than in SC. The temperature in the area of Alcañiz at 12^{00} UTC is only 24 °C (compared to 33 °C in the control simulation). As far as topography is concerned, it clearly influences the form of the mesolow along the Ebro Valley. As a result, the total precipitation field induced by topography (e_2, right panel in figure 4.1.12) is substantially different from the one obtained in the control simulation, with less precipitation in the Pyrenees. In addition, no precipitation occurs in the area of Alcañiz and it is limited to only a small area of the Mediterranean coast, where the temperature is higher. This precipitation starts at a later time than in the control simulation, at 18^{00} UTC, coinciding with the arrival of a high cold front.

In the simulation with flat terrain (experiment S1, left panel in figure 4.1.13) the mesolow spreads in all directions, since its geometry is not conditioned by the valley. The temperature in Alcañiz is somewhat lower than in the control simulation, reaching T =

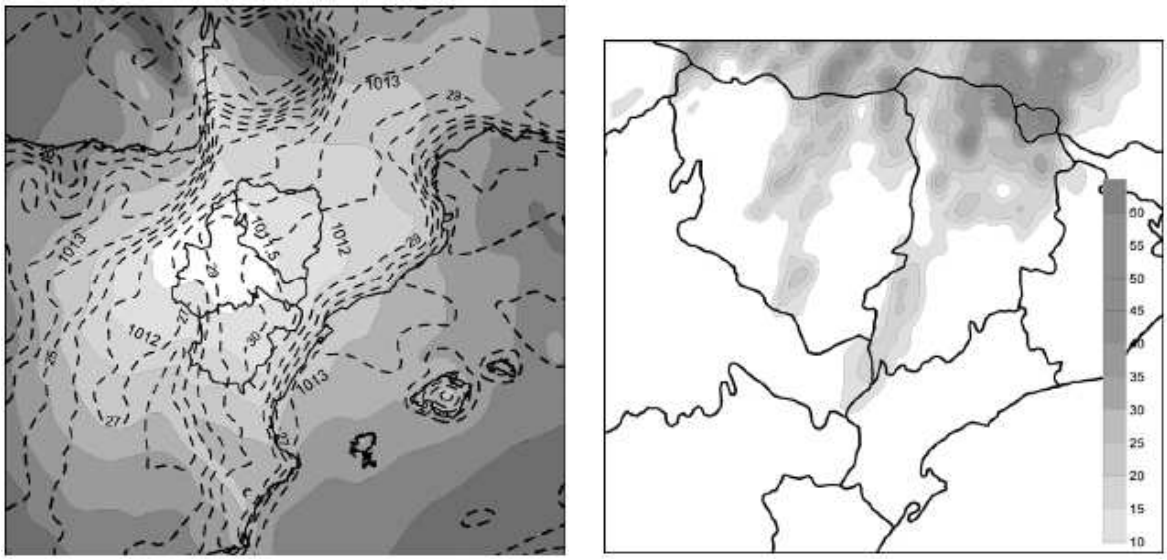

Figure 4.1.13: Left panel: Sea level pressure (hPa, shaded) and surface temperature (°C) at 12^{00} UTC on 16th August 2003, as simulated by the flat terrain experiment S1 (domain 2). Right panel: Simulated precipitation field induced by solar radiation (e_1) from 00^{00} UTC to 19^{00} UTC on 16th August 2003. Precipitation is in mm (domain 3)

30°C, and the low-level inflow from the Mediterranean Sea is not present. Consequently, the total precipitation field induced by solar radiation (e_1, right panel in figure 4.1.13) comprises a larger area than in e_2, drawing a map similar to the control simulation in the Pyrenees, but with lower precipitation rates, and affecting Alcañiz only to a small extent with 10-15 mm.

These results show that neither of the two factors in isolation can explain the precipitation caused by the severe storm in Alcañiz. Therefore, synergic effects of the two factors have been studied. The interaction of topography and solar radiation is essential to determine the places where rain actually fell and those where it did not fall.

In figure 4.1.14 we see that positive values correspond to a positive contribution to the total precipitation field. It is precisely in the area where the model locates the storm in Alcañiz that the combined effects of topography and solar radiation are more important (darker shaded areas). In contrast, the interaction of these two factors causes the opposite effect in other areas of Northeastern Spain, as shown in figure 4.1.14 shaded in light grey.

This case study leads to the conclusion that the mesoscale synoptic situation seems to have a rain potential by itself, but the thermal low of the valley causes an inflow of

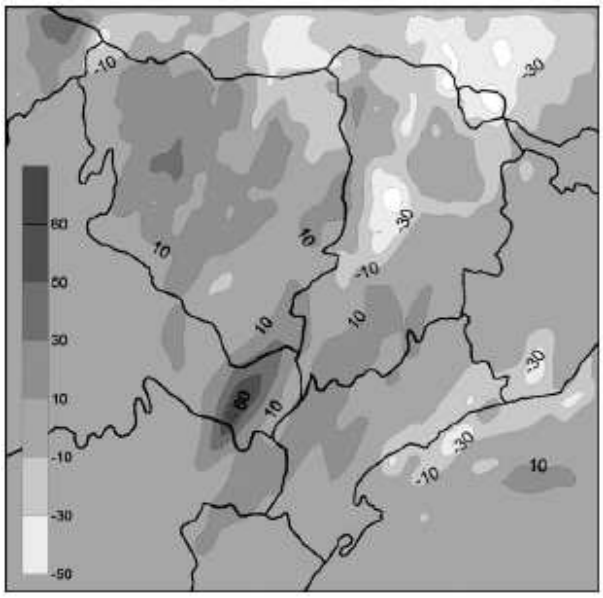

Figure 4.1.14: Simulated precipitation field induced by the interaction between topography and solar radiation (e_{12}) from 00^{00} to 19^{00} UTC on 16th August 2003. Precipitation is in mm (domain 3)

moist air from the Mediterranean Sea and updrafts in the area, occasionally generating convective clouds. The topography, together with solar radiation, contributes to highly localised and intense precipitation in the study zone.

4.1.3 Sensitivity to thermal anomaly using PV inversion

PV anomalies theory (Thorpe, 1986) indicates that above a positive PV anomaly there is a thermal positive anomaly above and a cold one below. This characteristics of the thermal anomaly will be used to study the sensitivity to the surface thermal anomaly present in the initial conditions of the simulation. Namely, it was shown (Hoskins et al., 1985) that a surface thermal anomaly can be regarded as an equivalent to a concentrated PV anomaly contained in a thin surface layer. The term surrogate PV has been introduced and widely used in referring to the surface potential temperature anomaly (Reed et al., 1992; Huo et al., 1998), since the potential temperature anomaly is mathematically treated like a PV anomaly under the ground surface (Bretherton, 1966).

In order to study the sensitivity to this 'formal' PV anomaly, piecewise PV inversion technique will be used. In this case surface thermal anomaly is identified as the signature instead of a PV anomaly. Piecewise PV inversion technique (Davis and Emanuel, 1991)

usually apply zero bottom conditions. If a given thermal anomaly is chosen as the bottom conditions and no PV anomaly is selected, PV inversion technique will provide the inverted fields related to the bottom condition. This could also be understood as the inversion of the surrogate PV related to the thermal anomaly. Inverted fields of a surface thermal anomaly of November 11-14th 2004 case are shown in figure 4.1.15. It is show how a positive surface thermal anomaly is related to a cyclonic rotation of the flow (bottom right panel in figure 4.1.15) and a pressure fall (top right panel in figure 4.1.15).

Thermal anomaly in November 11-14th 2004 case

The cyclone of the November 2004 episode (Horvath et al., 2006) was initiated over the hot and dry environment of the Atlas lee. Due to the characteristics of the zone, it could be said, that it was initially formed as a thermal low (see figure 4.2.2).

Sensitivity studies to thermal low anomalies with the piecewise PV inversion technique are carried out in the study of the November 11-14th 2004 episode described in the following section. It has also been applied in the baroclinic study of the November 9-12th 2001 cyclone episode (see chapter 3).

It is carried out a simulation where initial surface thermal anomaly has been weakened (figure 4.1.15). Resultant initial cyclone is about 5 hPa lower and 4 K colder at 925 hPa, and shifted to the north than the initial cyclone (see figure 4.1.16). Although the initial cyclone has been changed, the evolution of this cyclone does not vary significantly from the original one. This results can be a signature of the strong role of the surface thermal anomaly in the formation of the cyclone, but with a low impact in the trajectory of the cyclone.

It was shown in the control run that the cyclone was attached to the small barotropic area in the beginning of the cyclogenesis. However, this area also corresponded to the strongest low-level PV values, associated with the strong primary PV banner near the SW edge of the mountain. In order to separate the influence of the thermal anomaly and low-level PV, a simulation with orography, but without thermal anomaly was performed.

The difference between initial low-level temperatures of the sensitivity simulation and the control run is shown on figure 4.1.16a. The broad Atlas-scale thermal anomaly perturbation reached 4 K in the temperature field at 925 hPa, with associated mean sea level pressure increase of 5 hPa. Accordingly, the long baroclinic zone in the Atlas lee was significantly weakened. On a smaller scale, the shape of the isolines near the SW Atlas edge indicated weakening of the "secondary" thermal anomaly in the lee of the High Atlas, the place where the cyclone was initiated.

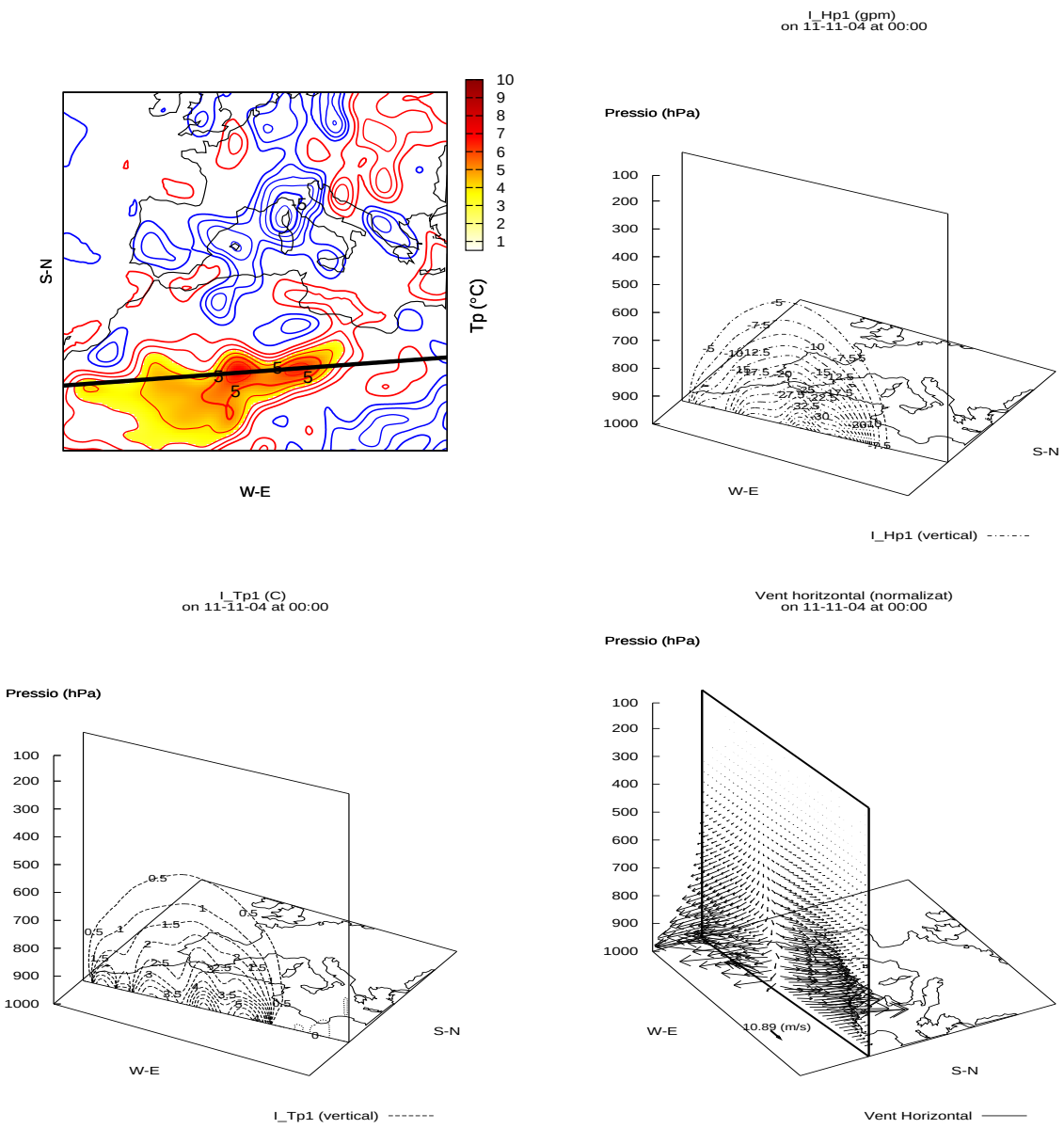

Figure 4.1.15: Top left panel: Thermal anomaly (solid line every 1°C; blue: negative anomaly, red: positive anomaly) and selected surface thermal anomaly (shaded area), dashed line indicates vertical cross sections. Top right panel: Cross section of the geopotential anomaly (every 2.5 gpm) due to the surface thermal anomaly. Bottom left panel: Vertical cross section of the thermal anomaly (every 0.5 °C). Bottom right panel: Vertical cross section of the wind anomaly (rescaled, see bottom vector). It is shown how a positive surface thermal anomaly induces a pressure and a cyclonic rotation of the above air.

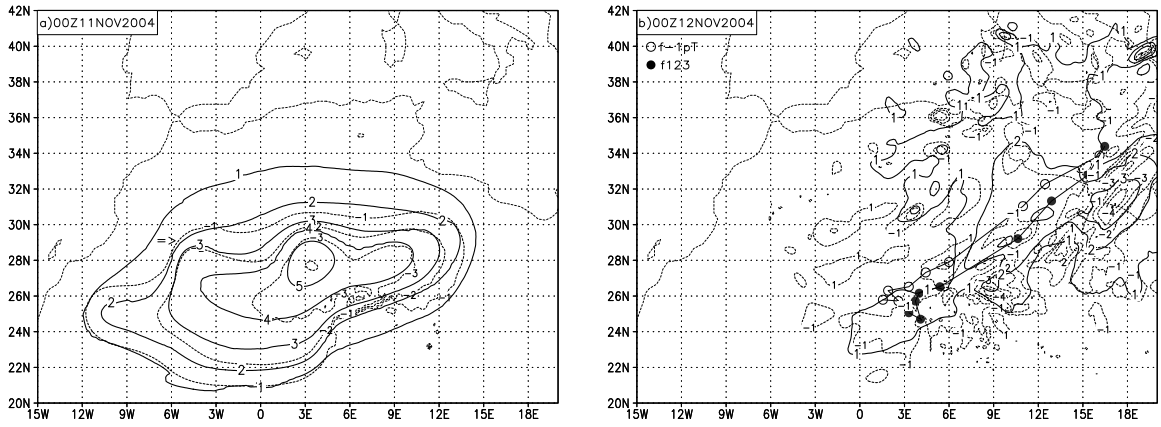

Figure 4.1.16: Definition of the thermal anomaly subtracted from the initial conditions at 11 Nov 2004 00 UTC (a). Fields denote a difference between the modified initial fields for the thermal anomaly sensitivity experiment and the original initial fields of the control run. The initially positive mean sea level pressure modifications (hPa) is plotted in continuous line and the initially negative temperature modification at 925 hPa in dashed. The arrow denotes the lee of the High Atlas mountains and removal of the "secondary" thermal anomaly. The structure of the thermal anomaly perturbation after 24 hours of simulation at 12 Nov 2004 00 UTC (b), defined as a difference described above. The cyclone trajectories in the experiment with thermal anomaly removed (f-1pT) and in the control run (f123) were superimposed on the figure, starting from 12 Nov 00 UTC, plotted every 6 hours

At 12 Nov 00 UTC, the approximate time of cyclogenesis in the lee of the Atlas, the initially removed thermal anomaly was strongly stretched out and already partly advected over the Mediterranean Sea with little effect in the Atlas lee (figure 4.1.16b). This suggests that the atmospheric conditions in the lee of the High Atlas at cyclone initiation time were only slightly changed by the removal of the thermal anomaly perturbation. It can be verified from the figure that the relative differences in the area of interest reached up to 1 K and 1 hPa. The dipole structure of the thermal anomaly perturbation in the lee of the High Atlas denoted weakening of the baroclinic zone and frontally induced low-level PV before the cyclone commencement. Further inspection of the low-level atmospheric conditions at 12 Nov 00 UTC (figure 4.1.17ab) showed that the surface baroclinic zone was somewhat weaker compared to the control run, in accordance with figure 4.1.16b, while the barotropic zone near the cyclone initiation point was more uniform. In this barotropic zone, a slightly weaker cyclone centre was located more inside the secondary thermal anomaly, closer to the mountain and orographic PV banner then in the control run. However, already at 12 Nov 12 UTC, there was no notable difference in the cyclone centre intensity or surface baroclinicity in the area of interest (figure 4.1.17c-d). Nevertheless, the cyclone centre was positioned closer to the mountain and continued to take that path in its further development (figure 4.1.16b).

The simulation showed that a thermal anomaly in the lee of the Atlas built up rather quickly, practically during the 24-hour interval preceding the cyclogenesis. Thus, little reliance could be made on the separation of low-level PV and thermal anomaly influences on the intensity of cyclone initiation in our simulation experiments. However, it seems that the location of the cyclone initiation showed sensitivity to thermal anomaly positioning in the mountain lee (see topographic configuration of the domain in figure 4.1.18).

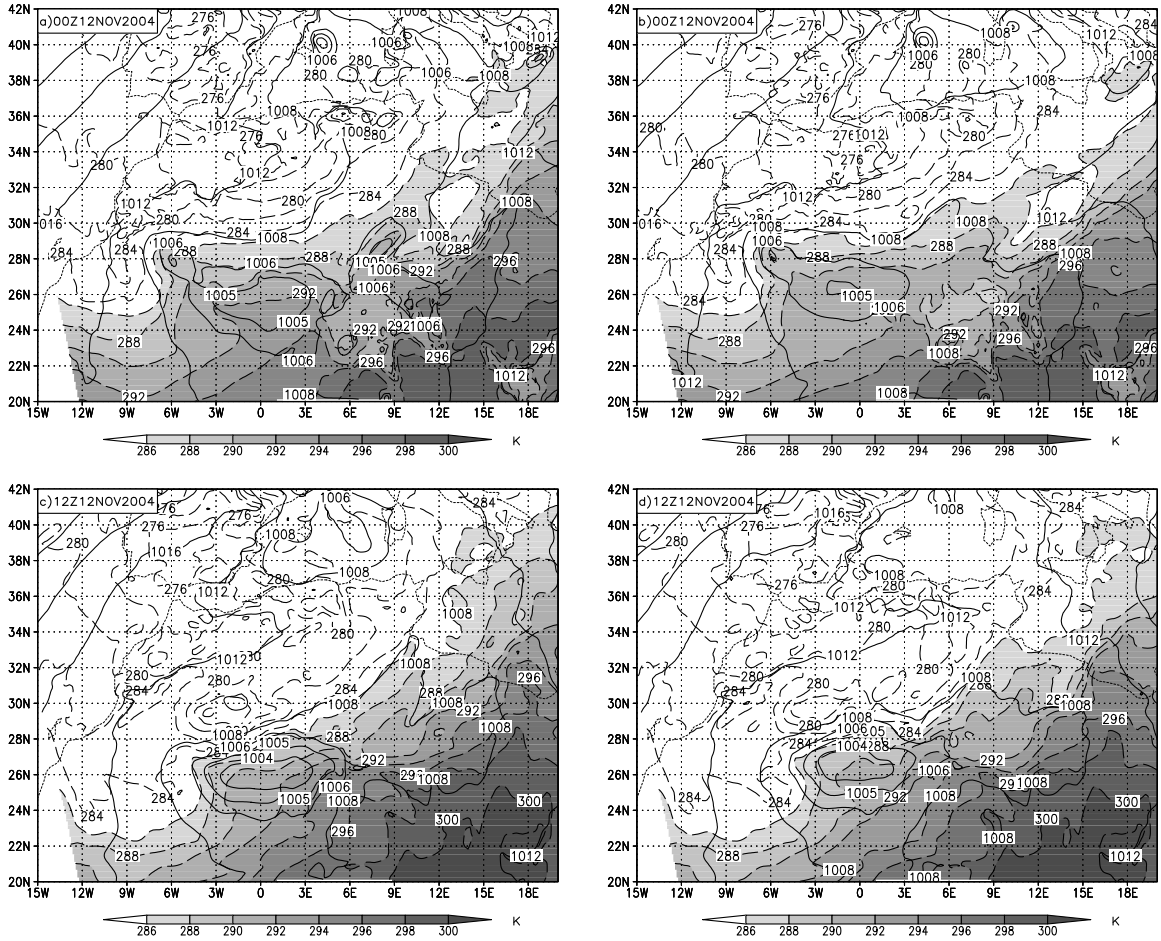

Figure 4.1.17: Model forecasts (shown on a zoomed domain) of the control run (a) and the thermal anomaly sensitivity run (b) at 12 Nov 2004 00 UTC and the control run (c) and the thermal anomaly sensitivity run (d) at 12 Nov 2004 12 UTC. Mean sea level pressure (hPa) is shown in continuous line (above 1008 hPa every 4 hPa, under 1006 hPa every 1 hPa). Temperature is plotted in dashed line (every 2 hPa) with shaded values over 286 K

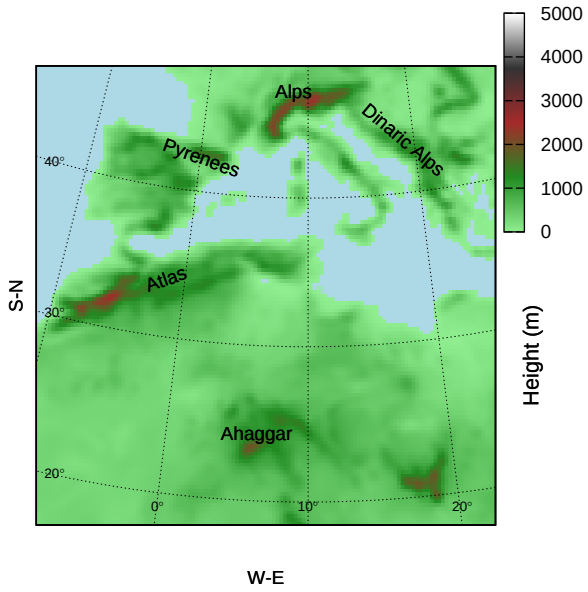

Figure 4.1.18: Topography of the domain of interest

4.2 Topographic lee influences

In the November 11th-14th 2004 case, an Atlas lee cyclogenesis (see figure 4.2.1). In contrast to the Alps-lee cases, Atlas cases present the singularity that their development is above extreme hot and dry area.

4.2.1 Extreme Bura case on November 11-14th 2004

During this case, a large upper-level trough was present above the Iberian peninsula on Nov. 11th (figure 4.2.2). This upper level trough was clearly depicted by the water vapour satellite image (EUMETSAT source) as a dry water vapour content (black zone in figures 4.2.7 and 4.2.8). At the same time, old signs of instability were present in the Adriatic Sea zone (between November 7th and 8th where recorded about 180 mm of precipitation in Albania).

Synoptic pattern is dominated by a high pressure zone that determined the flow in the North African region. At low levels a permanent northwestern flow affected the Atlas

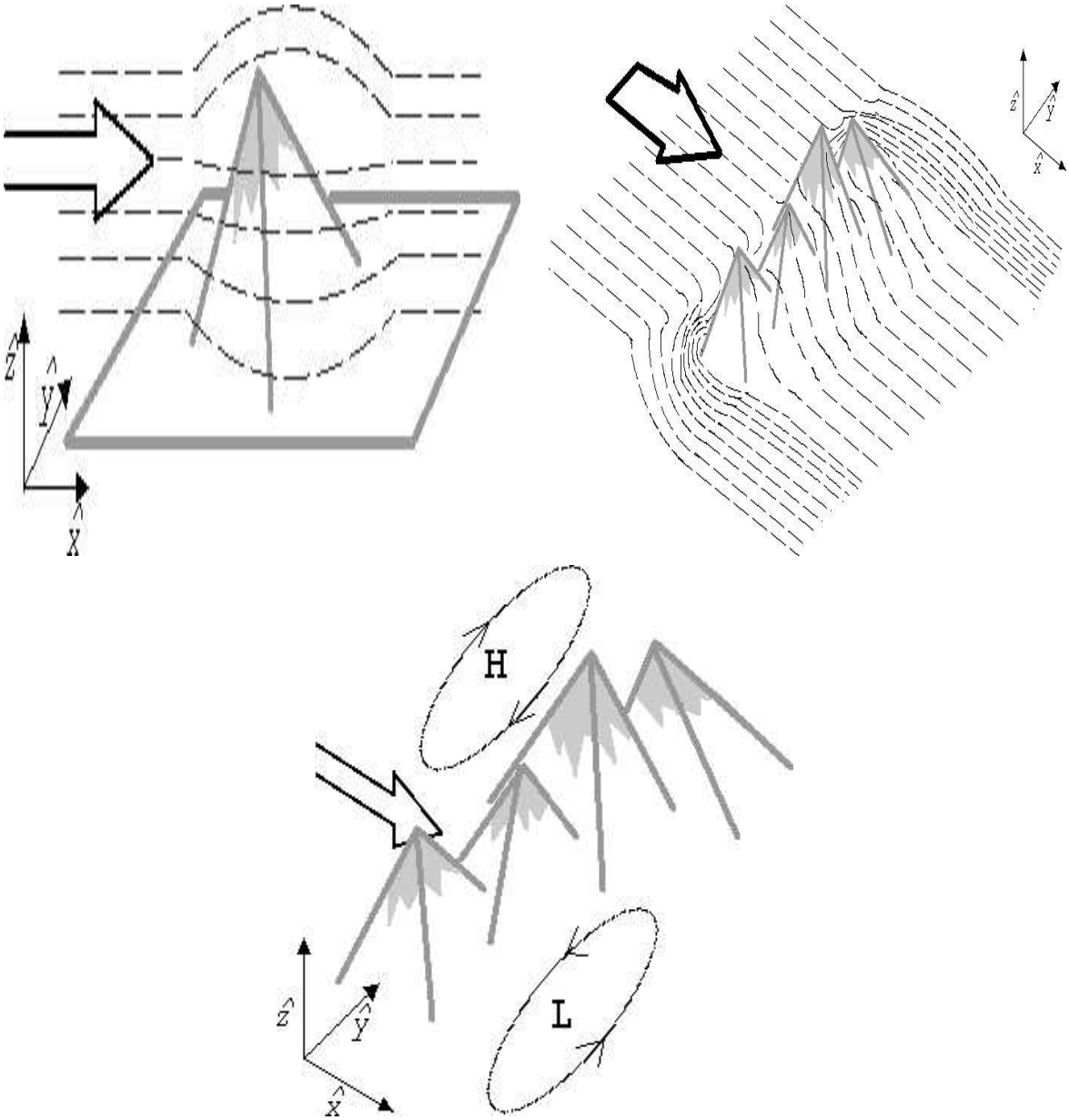

Figure 4.2.1: **Lee cyclogenesis:** Mountains block the flow of a persistent synoptic wind (top left and right panels). In the windward side if the flow could not overpass the mountains, air becomes compressed and the pressure increased and a High pressure disturbance is created. In the leeward the diminishing of the air decreases the pressure and a low pressure disturbance is generated. By this way, a dipole system is established (bottom panel)

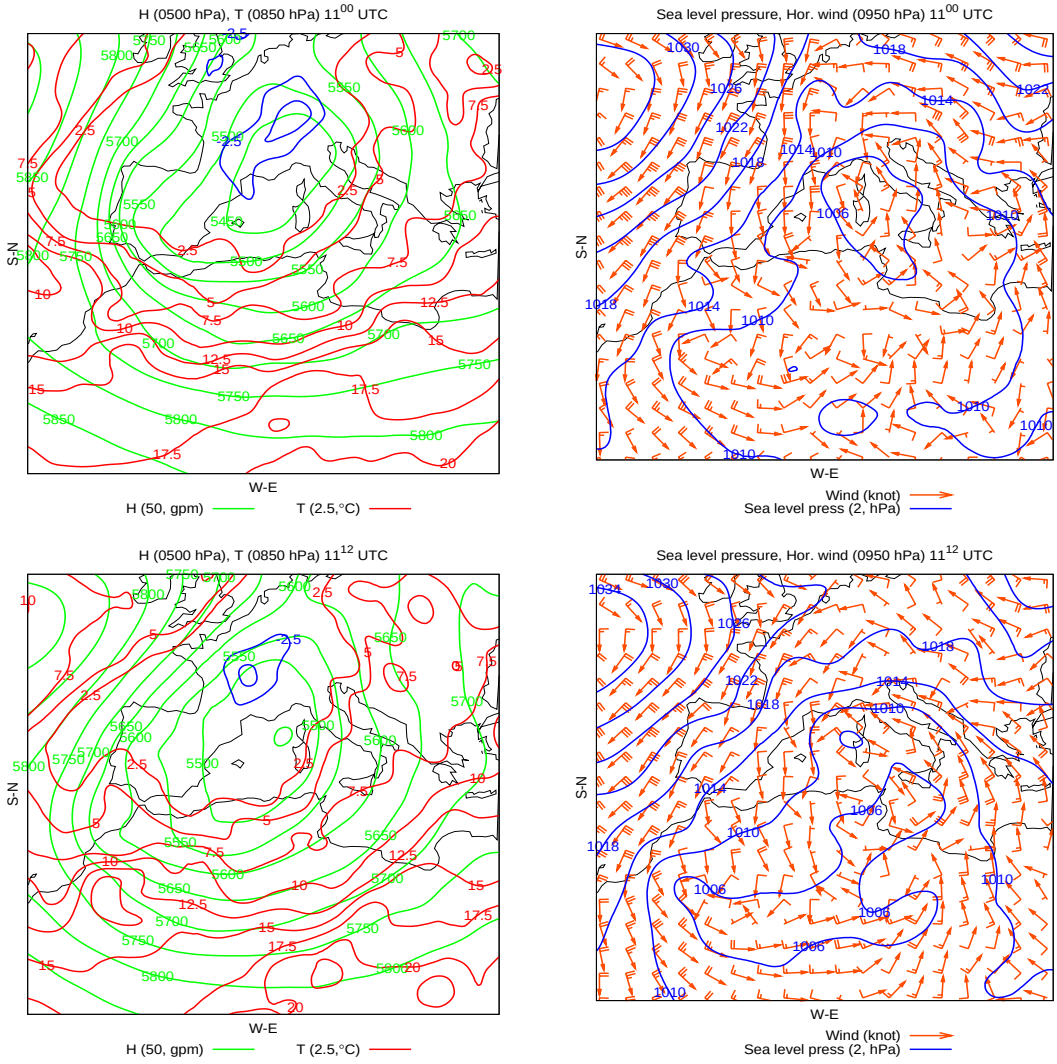

Figure 4.2.2: NCEP analyses evolution of the case. Left panel: Geopotential height (H) at 500 hPa (every 40 gpm, green line) and Temperature at 850 hPa (every 2.5 °C; red line, positive values; blue line, negative values). Right panel: Sea surface pressure (every 4 hPa, blue line) and horizontal wind at 950 hPa (orange barbs notes; large: 10 kt, short: 5 kt). On Nov. 11 at 00^{00} UTC (top), and at 12^{00} UTC (bottom)

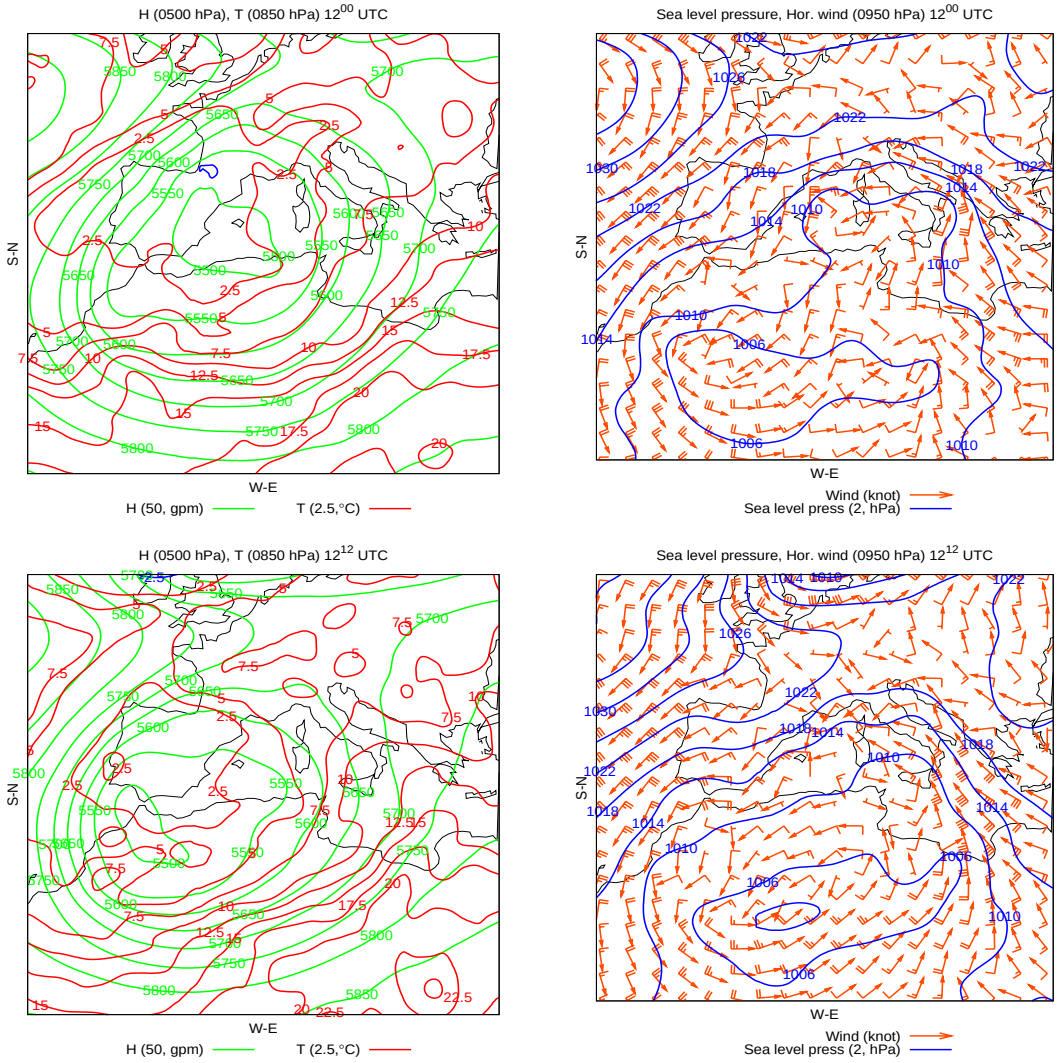

Figure 4.2.3: As in figure 4.2.2, but on Nov. 12th at 00^{00} UTC (top) and 12^{00} UTC (bottom)

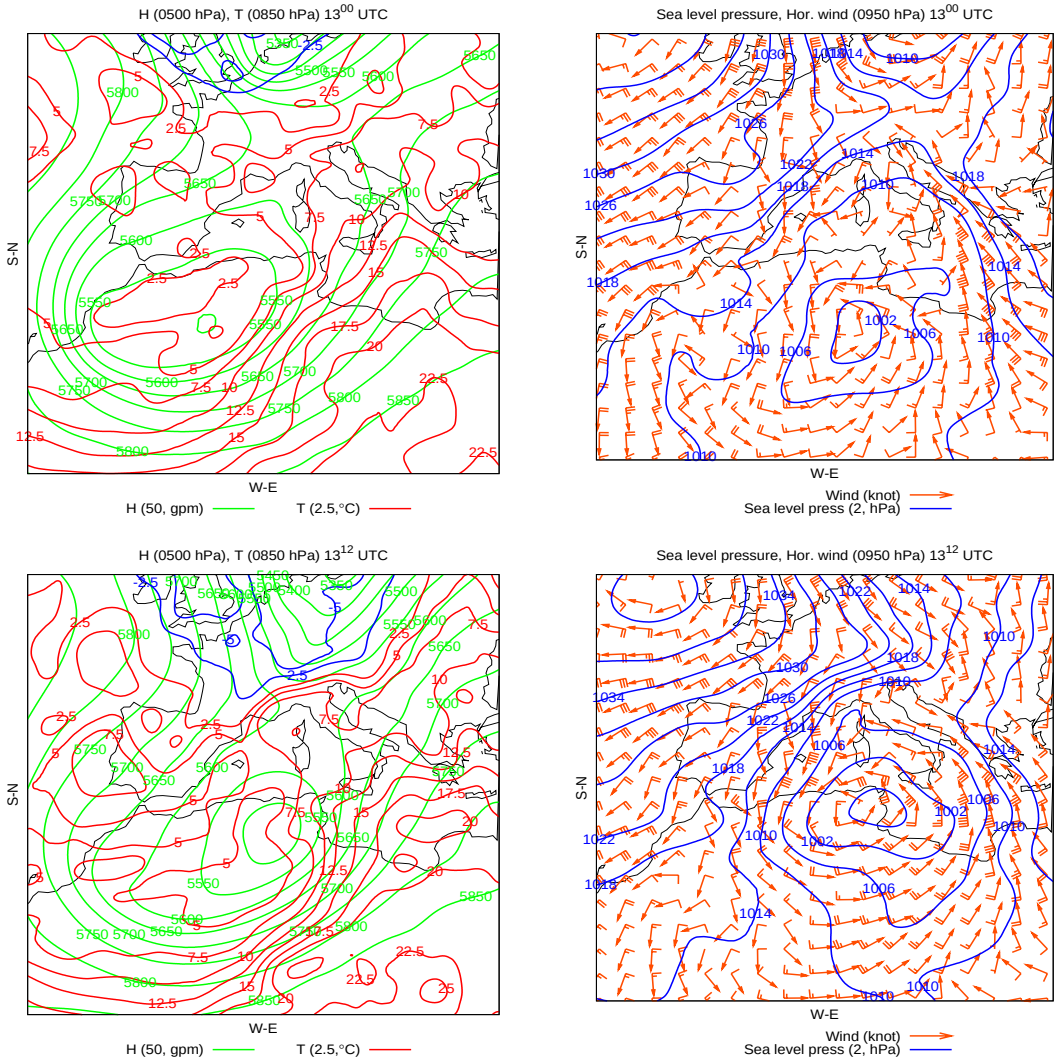

Figure 4.2.4: As in figure 4.2.2, but on Nov. 13th at 00^{00} UTC (top) and 12^{00} UTC (bottom)

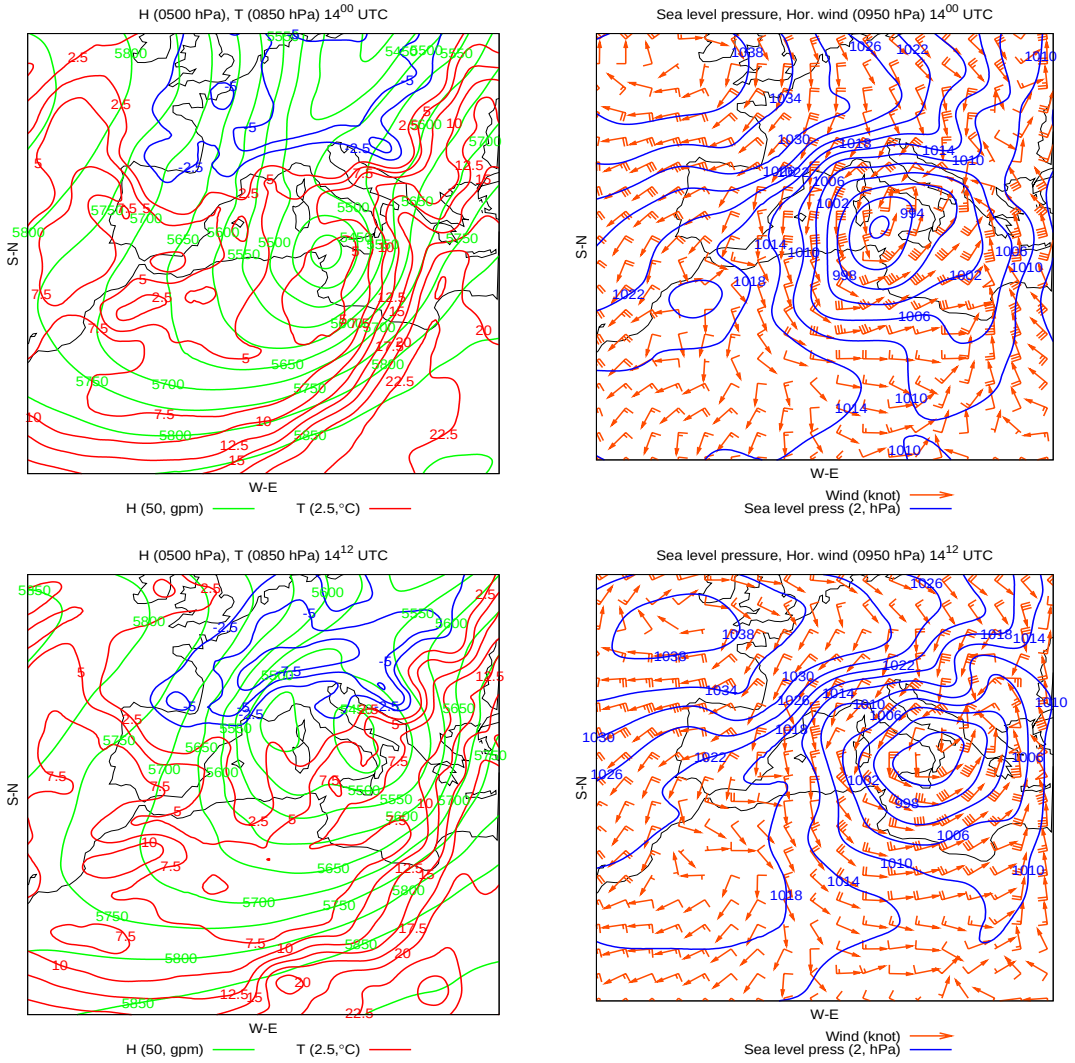

Figure 4.2.5: As in figure 4.2.2, but on Nov. 14th at 00^{00} UTC (top) and 12^{00} UTC (bottom)

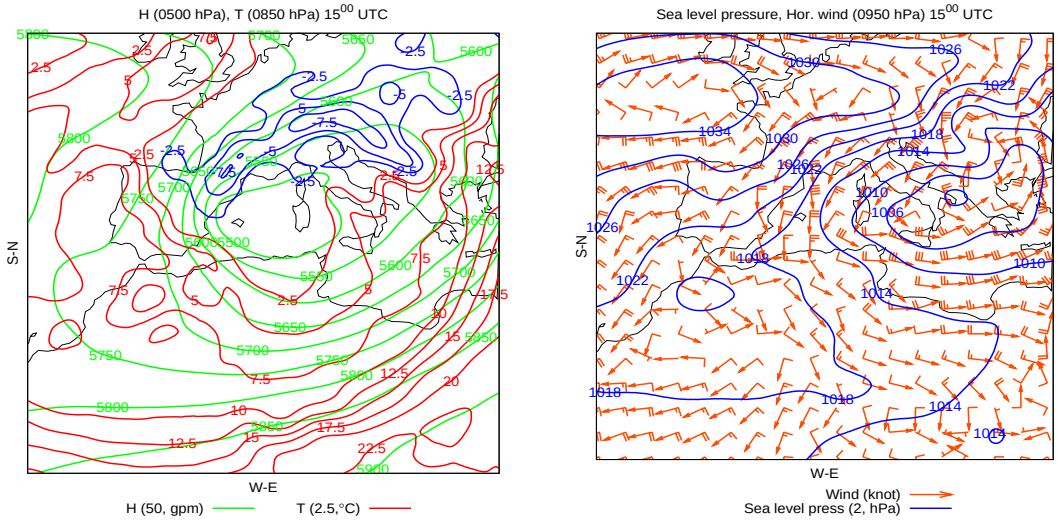

Figure 4.2.6: As in figure 4.2.2, but on Nov. 15th at 00^{00} UTC

range and in the southern part of the Atlas range there was an important longitudinal thermic gradient (figure 4.2.2 on Nov. 11 at 00^{00} UTC). Initially the flow kept blocked by the Atlas, but after a low detraiment the flow could overpass the range and the initial disturbance started to growth (Nov. 11th at 12^{00}). At the same time, intense radiative fluxes are simulated in the African plateau (about 400 Wm^{-2}, not shown). Upper level trough moved southward and the surface disturbance moved eastward following longitudinal thermal gradient at the south lee of the Atlas range (figure 4.2.3, Nov. 12th 12^{00}). From this moment, eastward movement of the cyclone and the upper level trough became very similar (might be a signature of the acouplement between upper and low level disturbances). The coupling between disturbances and the surface thermal gradient established the needed circumstances that allow the development of the baroclinic mechanism (Hoskins et al., 1985).

Cyclone kept growing during the Atlas lee and the coupled phase between upper level and low level disturbances. When the cyclone reached the coastal line of Tunisia (Nov. 13th 12^{00}, figures 4.2.4 and 4.2.8) it experimented a strong and fast deepening, from which it reached its mature state. At the same moment, it can also be seen above the Mediterranean Sea a secondary thermal gradient with a SW-NE direction. Meanwhile the cyclone started to decay it was moving towards the NE (14-15 Nov., figures 4.2.5 4.2.6). At this step of the cyclone evolution, strong convective activity is depicted by the satellite images at the South of Italy (figure 4.2.8, Nov. 14th 12^{00}). In concordance with a high pressure zone in the Atlantic Sea, a strong pressure gradient was established allover the Alps and Dynaric Alps. According to this distribution of pressures, strong winds can be developed

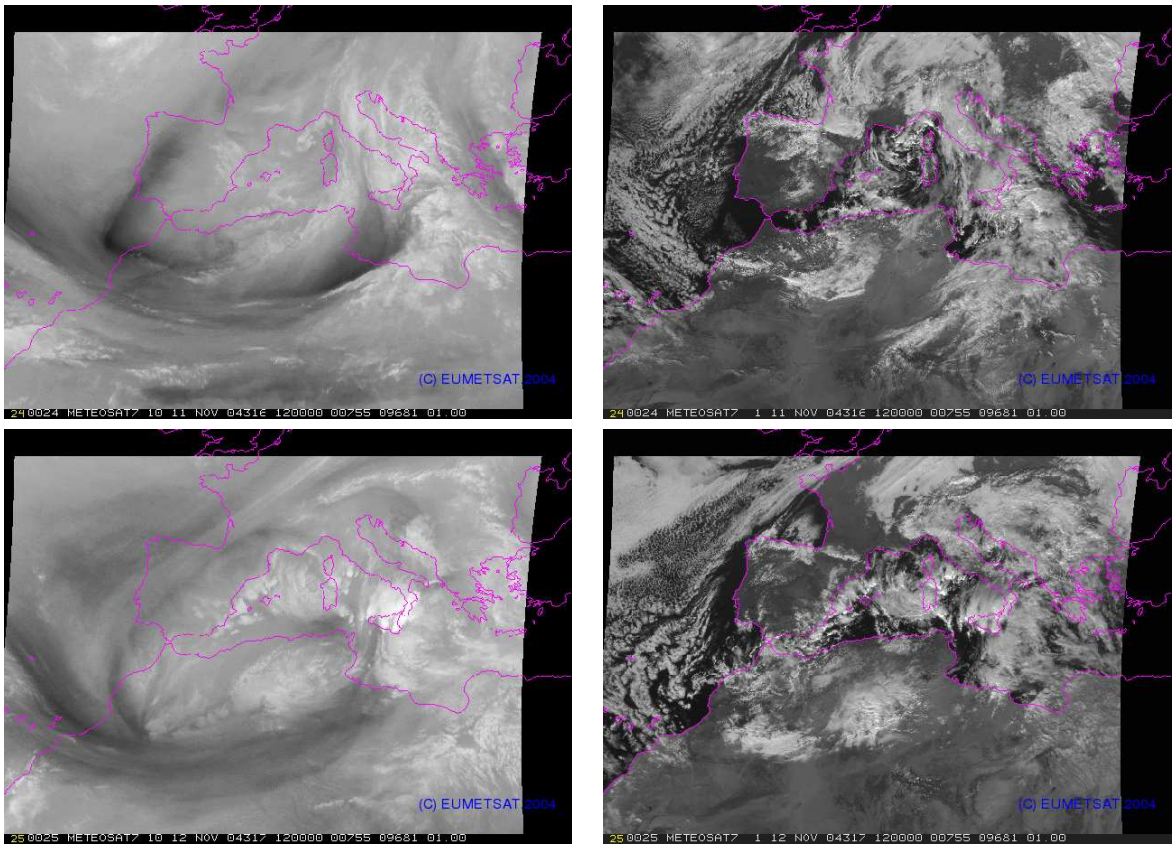

Figure 4.2.7: METEOSAT7 images for the vapour water channel (left) and the visible channel (right). On Nov. 11th at 12^{00} (top) and Nov. 12th at 12^{00} (bottom). Upper level trough is identified as the dark free cloud area due to the upper level downdrafts of dry air from higher levels. Cloudy zone seen in the visible channel image at the south of the Atlas mountains corresponds with the cyclone. Images with the collaboration of Ángel Luque)

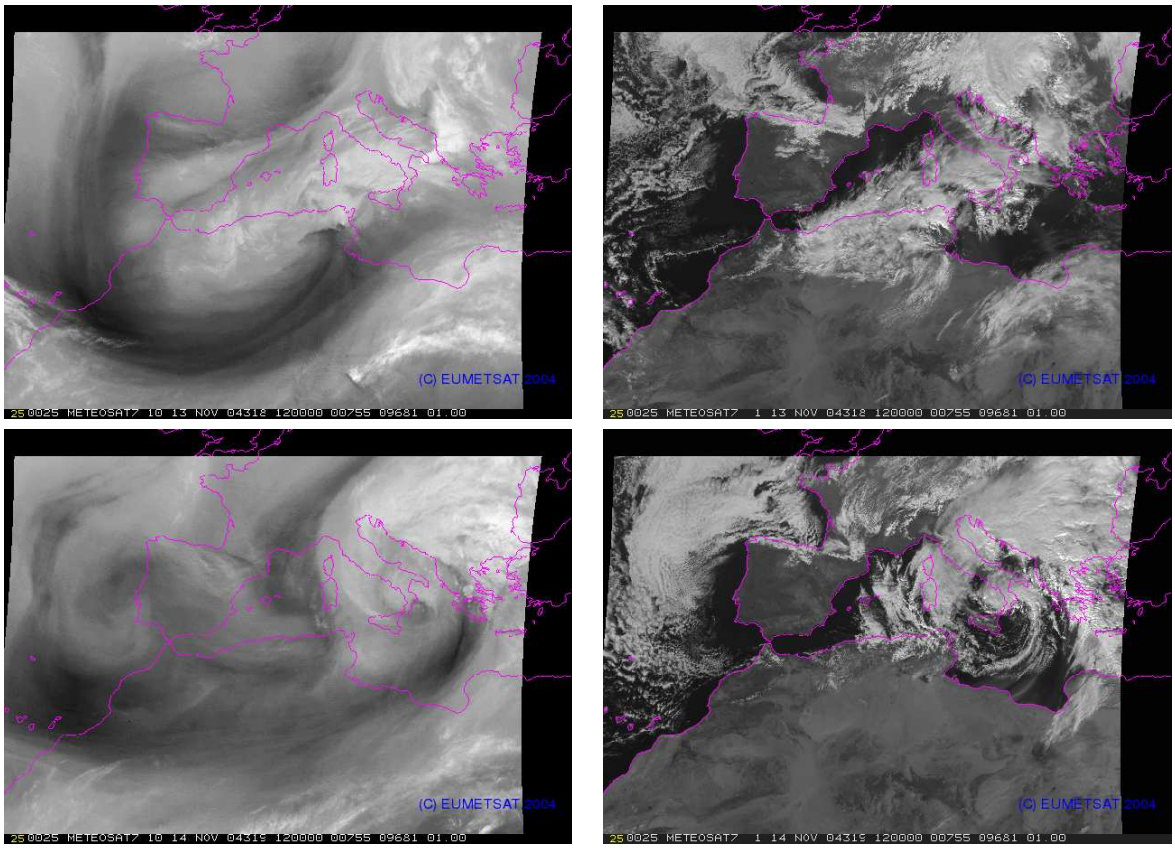

Figure 4.2.8: As in figure 4.2.7, but on Nov. 13th at 12^{00} (top) and Nov. 14th at 12^{00} (bottom). The movements of the cyclone observed in the visible channel image (right panels) corresponded with the movements of the upper level trough (dark zones in the water vapour channel images, left panels)

in the Rhône river basin and in the North base of the Adriatic Sea known as Bura winds. During this period of time, heavy precipitation were recorded in the south of Italy (about 200 mm/24h) and extreme Bura winds in the Croatia region (sustained winds about 35 ms^{-1} and gust winds about 60 ms^{-1}). 60 ms^{-1} gust winds have been established as the strongest gust wind record in Croatia.

Mediterranean phase of the cyclone is out of interest in the study of Atlas lee cyclogenesis. However, such kind of strong and quick deepening of the cyclones, have also been observed in other Mediterranean cases (Romero, 2001; Homar et al., 2002a) and in the North Atlantic bombs Sanders and Gyakum (1980); Sanders (1986) or similar cases Gyakum (1983a,b); Uccelini et al. (1985); Whitaker et al. (1988); Kuo et al. (1991a); Huo et al. (1995). The deepening process is associated to the strong amount of water evaporation from the sea and the strong formation of clouds. Large amounts of water vapour and heating at middle levels contribute significantly to deep the cyclone in a short time (Hoskins et al., 1985; Davis and Emanuel, 1991).

Validation of control simulation

The synoptic evolution of the lee cyclone in the control simulation (figure 4.2.9) shows that mean sea level pressure fields, system movement and deepening were moderately well simulated, experiencing some time delay in the process evolution. The upper-evel potential vorticity core at 300 hPa level reached 14 PVU at the time it was advected over the Atlas region (figure 4.2.9c). This cut-off upper tropospheric low induced a closed upper-air circulation as indicated by geopotential height distribution. Towards the end of the analysed period (figure 4.2.9d), which is approximately the time when the cyclone left the lee and entered the Mediterranean (14 Nov 00 UTC), the upper-level potential vorticity anomaly weakened, probably at the expense of interaction with the low-level vortex. The axis of the lee cyclone had a slightly negative tilt that tended to get more neutral with time. All of the aforementioned facts agree with the (Pettersen and Smebye, 1971) cyclone type B, and are in close resemblance with the lee cyclogenesis synoptic features.

In a mesoscale analysis of the model run, we investigated the lower tropospheric conditions. As mentioned in evolution of the system, strong northerly winds together with high surface sensible heat flux created an Atlas-sized thermal anomaly already on 10 Nov, far prior to the cyclogenesis. However, soon upon its creation, cold air crossed the lower NE part of the Atlas range and reduced the thermal anomaly to the lee of the High Atlas Mountains (figure 4.2.10a). A strong shear line is visible on 12 Nov 0 UTC as primary orographic PV banner of a considerable horizontal distance starting over the SW Atlas edge and overcoming 2.5 PVU in intensity (figure 4.2.10b). At the same time, two frontal low-level PV sources are visible: the first one corresponding to the front that

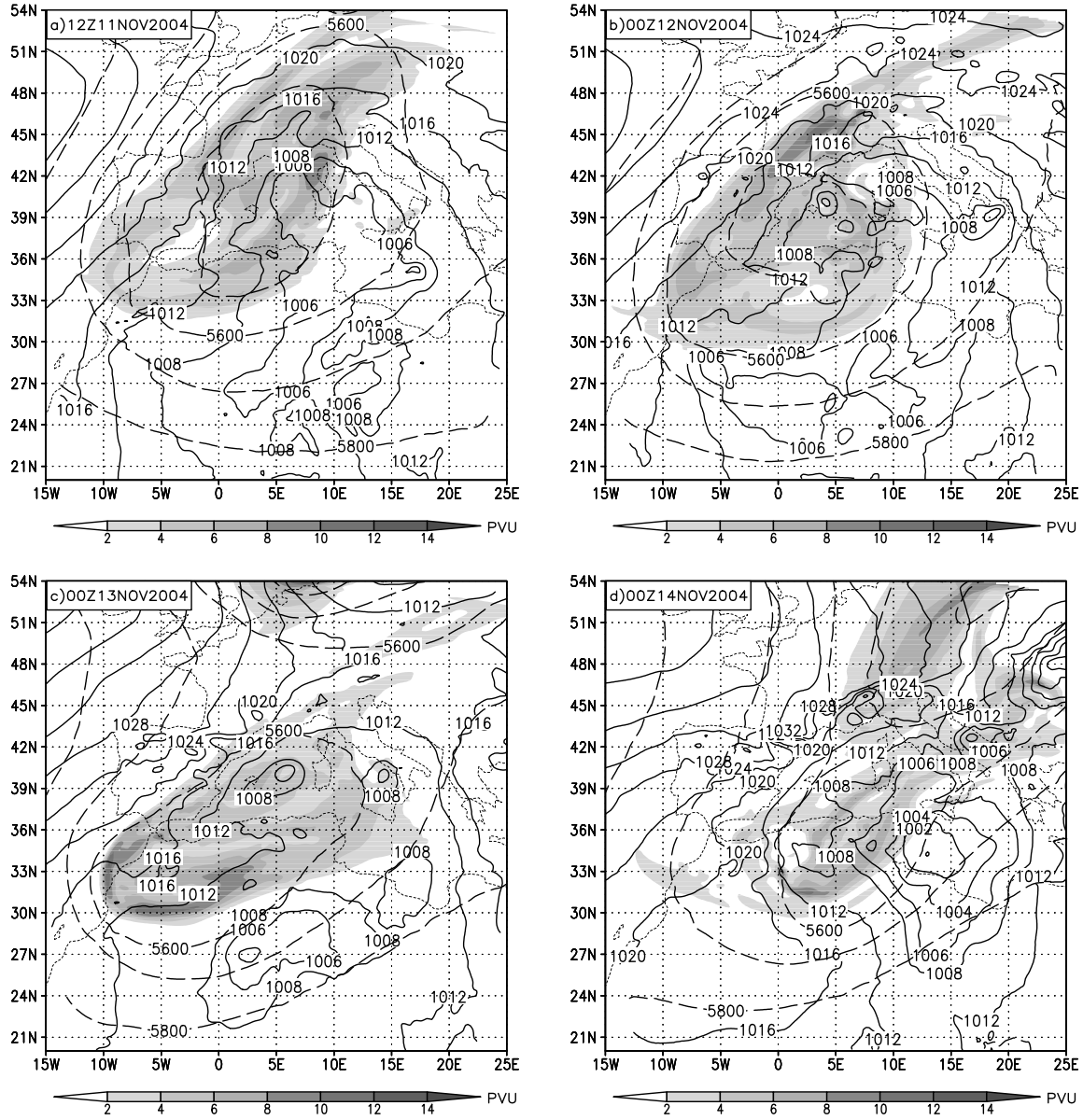

Figure 4.2.9: Model forecast of synoptic scale evolution at 11 Nov 2004 12 UTC (a), 12 Nov 2004 00 UTC (b), 13 Nov 2004 00 UTC (c) and 14 Nov 2004 00 UTC (d). Mean sea level pressure contours are plotted in continuous line with 4 hPa above 1008 hPa and 2 hPa below 1008 hPa values. Upper-level potential vorticity values at 300 hPa are shaded (white under 2 PVU black over 14 PVU), while geopotential at 500 hPa is plotted in dashed (every 100 gpm)

crossed the central and the northern part of Atlas and the second one more away to the east. They belonged to the same initial baroclinic zone and were separated due to the temporary orographic blocking of the first and quick outbreak from the Mediterranean of the second. In this period and subsequent hours, the very cyclone centre was located in a small quasi-barotropic zone and an area of enhanced low-level PV. During the 12t h of November, the cyclone moved northward towards the Mediterranean area. Low-level PV banners weakened, as a mere consequence of the reduced daytime stability. At 13 Nov 00 UTC (figure 4.2.10c), the orographic primary PV banner merged with the frontal one, forming a continuous source of low-level PV far away from the mountain. At the time, the cyclone centre started to be attached to the frontal baroclinic zone and stayed that way until the end of the analysed period. Orographically induced PV banner seemed to feed the low-level cyclone, resembling some of the documented cases of Alpine lee cyclogenesis (Aebishcer and Schär, 1998). On 14 Nov 00 UTC (figure 4.2.10d), which is the last time-sequence of our analysis, roughly corresponding to the time the cyclone left the lee and entered the maritime area, the cyclone centre reached 1000 hPa depth and was characterised with a well defined frontal structure.

Despite of the fact that differences between model simulations and ECMWF analysis (not shown) reveal that the model simulation of the investigated process was of limited quality, it is believed that its features were captured reasonably well enough to make the case appropriate for the sensitivity study and deduction of factor contributions in this lee cyclogenesis event.

4.2.2 Sensitivity tests

Control run of the case exhibits a good correspondence with the satellite-based observations (see figure 4.2.8). However, the maritime phase of the simulated cyclone does not match very well with the NCEP analyses and the observations. That could be a reflection of the lack of accuracy of the MM5 mesoscale model for simulations that least for a long period.

In previous sections upper-level potential vorticity (PV), orography and surface sensible heat flux (SSHF) were identified as main factors affecting this cyclogenesis event. A series of simulations will be addressed out in order to qualitatively analyse the contributions of these factors and their mutual synergies to the mean sea level value and cyclone centre position. This study will done with the aim of the factor separation technique (Stein and Albert, 1993). As mentioned previously, for that purpose 8 simulations had to be done. Thus, to address the orographic contributions to the process, the Atlas Mountains were removed from the terrain field. Secondly, surface sensible heat flux was withheld in a series of simulations, allowing for a determination of the influence of the associated surface forcing. Finally, an upper-level potential vorticity anomaly was removed from the

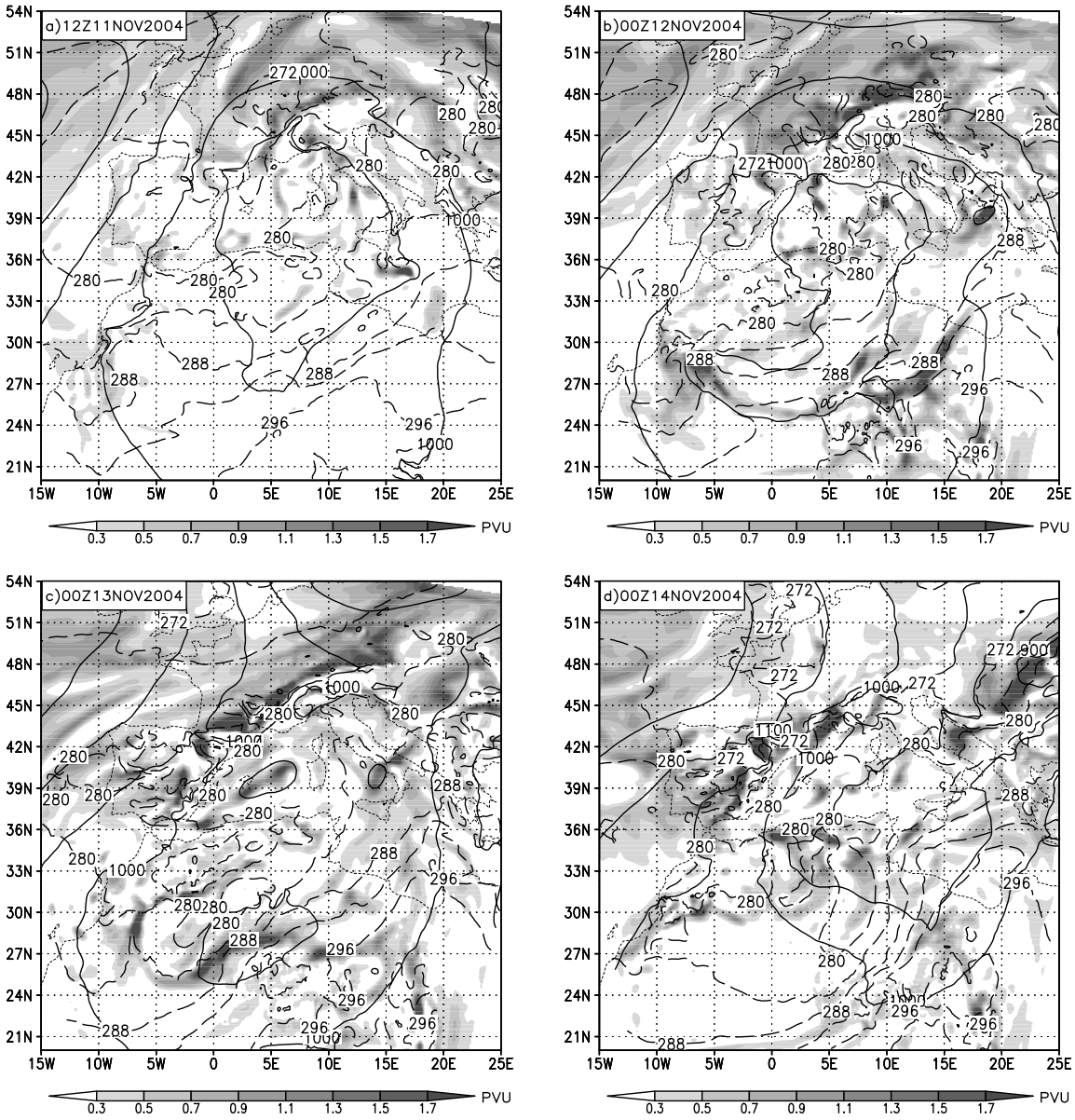

Figure 4.2.10: Model forecast of low-level conditions at 925 hPa at 11 Nov 2004 12 UTC (a), 12 Nov 2004 00 UTC (b), 13 Nov 2004 00 UTC (c) and 14 Nov 2004 00 UTC (d). Low-level potential vorticity is shaded (white under 0.3 PVU and black over 1.7 PVU). Geopotential is continuous line (every 50 gpm), while temperature is in dashed (every 4 K)

initial conditions to address the role of upper-level dynamical processes in the cyclogenesis.

The *Surface Latent Heat Flux* (here and after, LHF) and the *Sensible Surface Heat Flux* (here and after, SSHF) are related to the exchanges between earth surface and atmosphere. Due to the extremely dry conditions of the North African plateau, LHF will be not considered in the study. Preliminary results with this factor do not show a clear role of the flux.

Throughout the sensible surface heat flux (SSHF) the heat exchange between earth surface and the atmosphere is carried out (see figure 4.2.11). Surface is heated by the solar radiation (shortwave). Incoming radiation is used in different processes such as: diffusion to the ground, absorption into water surfaces (Sea, lakes or rivers), radiation in longwave form and/or atmospheric heating. This atmospheric surface originated induced heating is the first factor that heats/cools the first layers of the atmosphere Stull (1988). It could be considered as the source of energy that will produce the turbulence in the Boundary layer. Due to the extremely hot conditions of the north African plateau, it is assume that SSHF might have an important role in the development of the cyclone (Kuo et al., 1991b).

The removal of the upper-level potential vorticity anomaly from initial conditions was performed by applying the piecewise PV inversion scheme (Davis and Emanuel, 1991) described in section 2.2. The inversion was performed at the simulation starting time (11 Nov 00 UTC) using the NCEP/NCAR the 10-day averaged fields were centred at 12 Nov 00 UTC. However, in simulations with a total upper-level PV anomaly removed, the cyclone was excessively changed, both in intensity and in path. Thus, in order to keep the similarity with the real case, a PV perturbation used for our sensitivity study addressed only half of the total PV anomaly (figure 4.2.12). This later resulted in an upper-level PV anomaly that e.g. on 12 Nov 06 UTC reached 8 PVU at 300 hPa level, compared to the almost 14 PVU associated with the original upper-level PV anomaly. This should be kept in mind when considering the quantitative contributions of the upper-level potential vorticity and its interactions.

The influence of the Atlas mountainous range is realised removing all the topography of the mountain range from the simulation (height is fixed to 1 m allover the domain of the range, see figure 4.2.13). SSHF is studied throughout modifications in the boundary layer scheme used in the simulations. PBL used scheme is a high resolution modified version (Zhang and Anthes, 1982; Zhang and Fritsch, 1986) of Blackadar scheme (Blackadar, 1979). The SSHF is switched off in the scheme computations. By this way, PBL will be generated without the heating of the surface. Radiative heating from the sun will be heating the soil without any exchange with the atmosphere. Upper level PV anomaly will be studied via the piecewise PV Inversion.

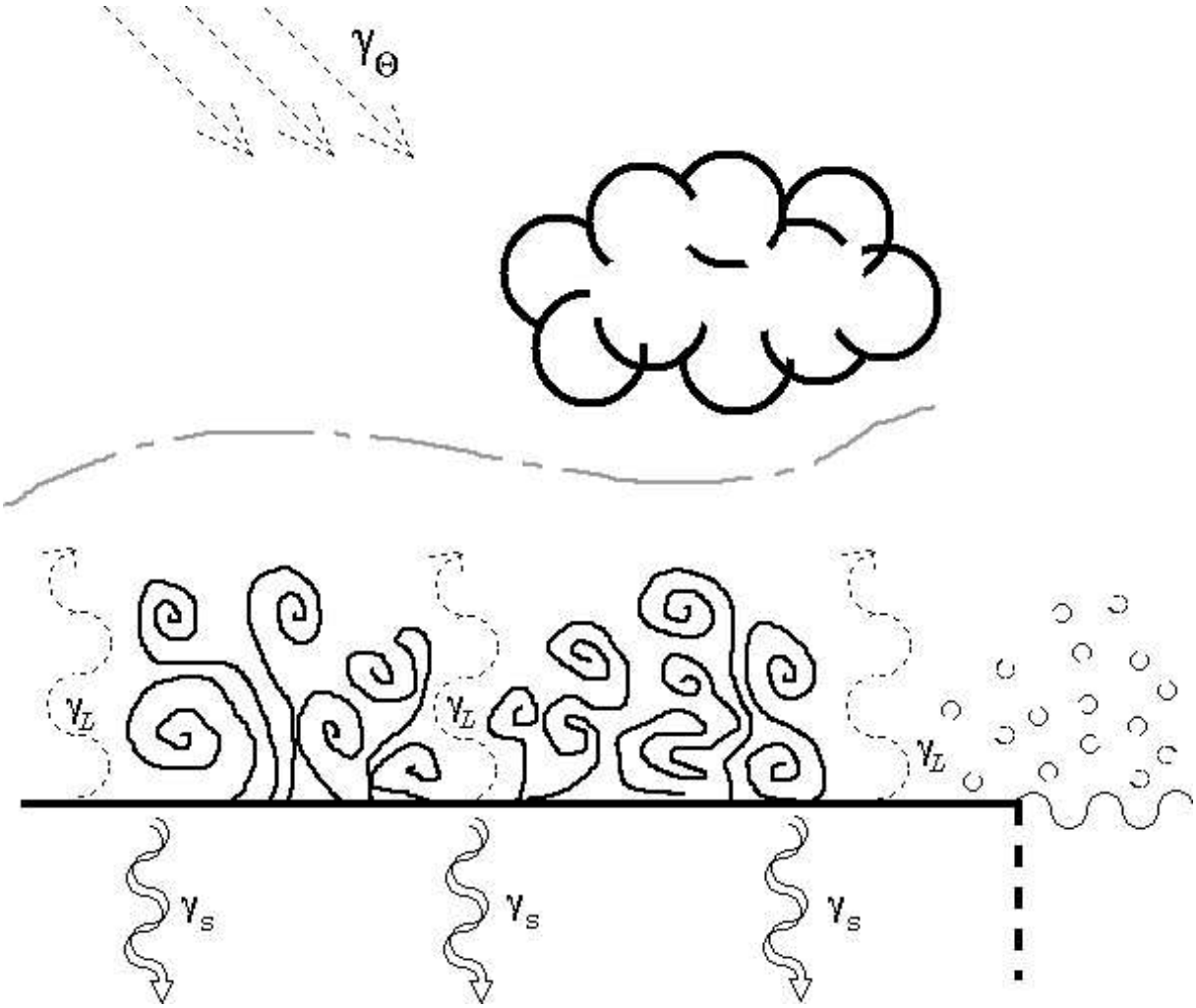

Figure 4.2.11: **Radiative balance:** Solar radiation (parallel and downdraft arrows, shortwave radiation γ_Θ) heats the surface. A fraction of the heat is emitted as longwave radiation (curved arrows, γ_L), which is partially absorbed by the water vapour of the clear-air, liquid water content of the clouds, CO_2. Another fraction (SSHF) heats the lowest layers of the troposphere from which the turbulence (spirals) is generated within the boundary layer (gray slash-dot line). Another fraction of the solar radiation is diffused in to the ground (γ_s, double curved arrows). Finally, another fraction evaporates the humidity of the soil surface, or the water of rivers, lakes or seas (opened circles)

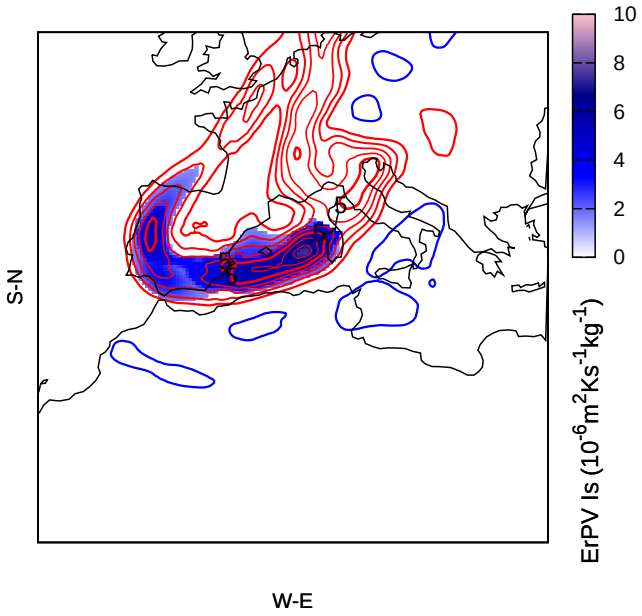

Figure 4.2.12: *Ertel Potential Vorticity* anomaly on Nov. 14th at 00^{00} UTC (solid line every 1 $PVU = 10^{-6}m^2Ks^{-1}kg^{-1}$). PV anomaly selected feature f_3 (shaded region, PV units)

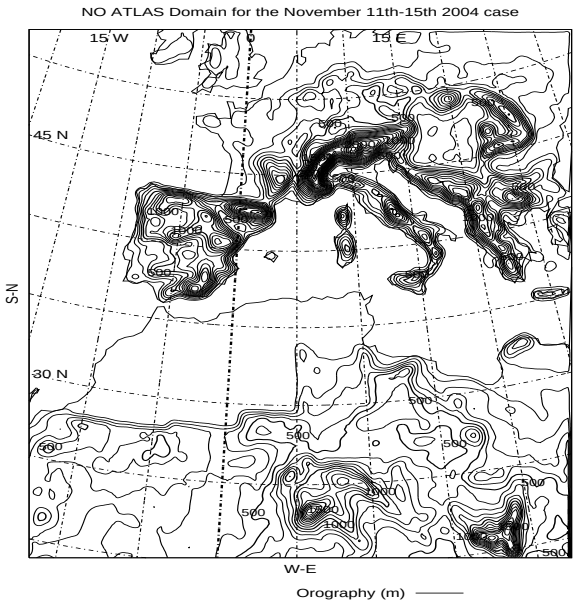

Figure 4.2.13: Orography after the removing of the mountain ranges of the Atlas f_1

Resultant selected sensitives are labelled as follows:

- e_0: Other effects
- e_1: Atlas range effect
- e_2: SSHF effect
- e_3: Upper level PV anomaly fraction effect at the initial conditions
- e_{12}: Synergy between Atlas and SSHF
- e_{13}: Synergy between Atlas and Upper level PV anomaly
- e_{23}: Synergy between SSHF and Upper level PV anomaly
- e_{123}: Triple synergy

A time evolution of the factor contributions to the mean sea level pressure value illustrates the dominance of different processes at different stages of the cyclone development (figure 4.2.14). The analysis focused on the period starting from 12 Nov 00 UTC (24 hours after the simulation initiation) that is the approximate time of cyclogenesis commencement in the simulation. The apparent cyclogenetic influence of upper-level PV in

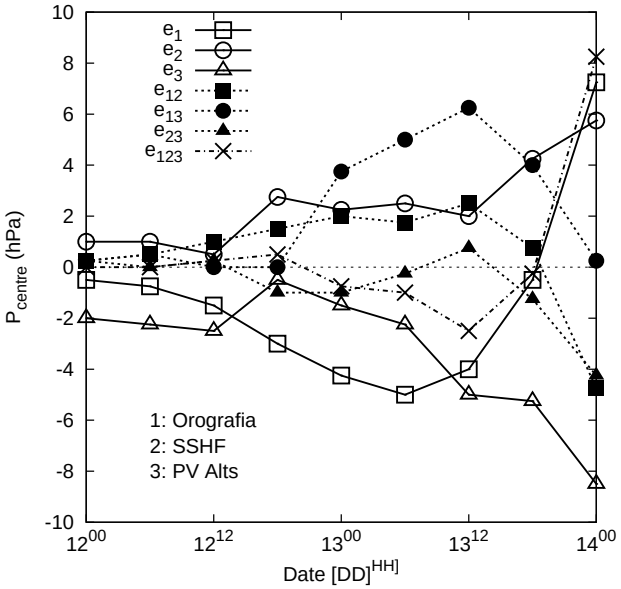

Figure 4.2.14: Temporal evolution of the effects of each factor on the control simulated central pressure of the cyclone (hPa)

the start of the analysed period (12 Nov 00 UTC, e_3 effect, line with empty triangles in figure 4.2.14) probably merely reflects the change in initial conditions. Namely, a removal of upper-level PV perturbation caused a warming of the low-level cold air impinging on the Atlas, thus reducing the intensity of the thermal anomaly and the associated pressure low. That is the reason why, before the cyclogenesis commenced, a mean sea level pressure was somewhat higher in the background simulation (with all factors excluded, f_0 simulation) than in the simulation with the upper-level PV perturbation included (f_3).

The first pronounced cyclogenetic influence was an orographic one (effect, e_1, line with empty squares in figure 4.2.14), starting around 12 Nov 00 UTC, cumulatively exerting 5 hPa deepening on the cyclone. This influence was associated with a frontal retardation and creation of the thermal and low-level PV anomalies in the lee of the High Atlas that were not present in simulations without orography. At that time and in subsequent hours, the cyclone centre was mostly attached to the quasi-barotropic lee area, marking the first phase of the lee cyclogenesis. At 13 Nov 06 UTC, an orographic influence first diminished (e_1), and then became strongly cyclolytic (destruction of a cyclone). This type of duality of orographic influence was already noticed in a study of the Alpine cyclogenesis by Alpert et al. (1995) and was probably due to cyclone movement out of the favourable lee area.

Similar results were achieved in Tsidulko and Alpert (2001), although the cyclogenetic influence of orography in their analysis does not seem to be so intensive as in this study.

The upper-level potential vorticity perturbation (effect e_3, line with empty triangles in figure 4.2.14) started to contribute to cyclogenesis at the time its strongest core got advected over the Atlas lee at 12 Nov 18 UTC. Its influence was in the subsequent period associated with reduced stability of the troposphere and a creation of a slightly stronger thermal anomaly at the surface (inclusion of the upper-level PV perturbation cooled the air impinging on the Atlas). Furthermore, stronger positive vorticity advection at upper levels induced greater low-level vertical velocities (e.g. in accordance with the omega equation, 2.2.21) and stronger low-level convergence, resulting in a more intense low-level vortex development. Stronger winds at lower levels resulted in the more intense cyclonic circulation and the stronger shear line in the lee. In other words, a cyclonic circulation of the upper-level potential vorticity anomaly propagated vertically (downward) to the middle and lower atmosphere, in accordance with conclusions derived from similar experiments for the Alpine lee cyclogenesis (Tsidulko and Alpert, 2001) and in idealised numerical experiments on the Sharav cyclone (Egger et al., 1995) However, as later analysis is going to show, the difference between the speeds of advection in simulations that define the upper-level PV perturbation influence (referred as e_3) indicates that part of its strong cyclogenetic influence in the end of the analysed period could be partially related to moist processes over the Mediterranean Sea.

The most pronounced contribution of sensible surface heat flux (effect e_2, line with empty circles in figure 4.2.14) seems to be the afternoon cyclolysis. It is evident that surface heat flux enables heat exchange between the atmospheric planetary boundary layer (PBL) and the surface. Thus, in the simulation without surface sensible heat flux, absorbed energy during the daytime (when SSHF is directed upwards) caused higher ground temperatures, but lower surface air temperatures near the ground and a less intensive planetary boundary layer. In this environment, a weaker PBL and less vertical mixing contributed to a stronger baroclinic zone and more intensive cyclone deepening. A similar cyclolytic influence in the early stage of the cyclone development has been noticed in work done by Kuo et al. (1991a), although their case took place over the sea. Furthermore, a horizontal air temperature gradient in the surface baroclinic zone was stronger then the horizontal ground temperature gradient at the same location. Thus, when enabled, the heat exchange tended to increase the horizontal temperature gradient in the ground, and decrease it in the low-level atmosphere, weakening the baroclinic zone and cyclone deepening. Finally, it is proposed that exclusion of SSHF affected the radiation balance at different levels in the atmosphere. In absence of SSHF, during the daytime, ground temperature was higher than in the presence of SSHF. This situation enhanced the longwave earth radiation, which became the main heat exchange factor between the ground and the atmosphere, since latent heat flux over the arid Atlas lee was rather small.

In contrast to SSHF that transferred the heat more locally to the surface boundary layer (and indirectly to the whole PBL through turbulent mixing), longwave terrestrial radiation was absorbed the most where the humidity was the highest. Throughout this process, cloudy areas in the free troposphere gained more, while the surface layer gained less heat energy compared to the control run. Thus, the PBL was less intensive contributing to a stronger surface baroclinicity and cyclogenesis as described above. On the other hand, the moist free troposphere was less stable due to increased heating. The heating of the moist free troposphere is known for its strong contributing to a cyclone deepening. For example, in Alpert et al. (1995), latent heat release was identified as one of the main contributors to cyclone deepening. Although the underlying mechanism was clearly not the same, the final effect in terms of a heat supply to the free troposphere seems to be qualitatively similar.

The afternoon cyclogenetic effect of SSHF noticed in the study seems to oppose the findings of Alpert and Ziv (1989), who investigated the generation mechanism of the Sharav cyclones with modified two-level linear baroclinic model suggested by Phillips (1954). Thus, their study mostly considered global to regional scale analysis that can be captured by quasi-geostrophic balanced dynamics. This result seems to indicate the scale dependence of the SSHF influence, and the importance of mesoscale frontal dynamics and boundary layer processes representation in the model, in order to fully determine the role of surface sensible heat fluxes in lee cyclogenesis events.

It is interesting to note the contribution of the synergy between orography and upper-level potential vorticity (e_{13}, line with filled circles in figure 4.2.14) on the mean sea level pressure values. The influence was clearly cyclolytic during the 18-hour period, starting from 12 Nov 18 UTC. It will be shown later in the analysis of cyclone paths, that it seems to be connected to the cyclone destruction at the orographic obstacle on the way to the Tunisia area. After that, on 13 Nov 12 UTC and subsequent hours, the synergy contributed to the cyclone recovery. At that time lower and upper-level vortices were tilted to the favourable western direction with height. Rough estimates of geopotential at 300 hPa and mean sea level fields on 13 Nov 12 UTC gave a horizontal dimension of the upper-level trough wave of L=60, and a separation of the centres of around 0.15L. If these numbers were applied to the idealised conceptual models of low-level-upper-level vortex interaction or linear instability theory (Bretherton, 1966; Hoskins et al., 1985), the waves would tend to hold themselves against the zonal flow (i.e. against differential advection), growing and reinforcing each other. This qualitative consideration seems to be roughly applicable at the end of the analysed period, when low-level and upper-level centres tended to be almost locked in phase.

It has been observed that an inclusion of SSHF in the simulations strengthens the upper-level PV. This is in qualitative agreement with the cyclogenetic synergy of SSHF

and upper-level PV (e_{23}, lines with full triangles in figure 4.2.14) seemed to show in the afternoons. Other synergies (e_{12}, e_{12}, e_{123}) did not seem to exert a significant impact on the cyclone centre deepening/filling, except in the very end of the analysed period. The corresponding results at that time should be interpreted with care, because of the cyclone centre spread at the end of the simulations. Namely, in some simulations the cyclone centres entered the Mediterranean, while in others still stayed on the continent. In this way, possible moisture processes could have influenced the results. However, the role of moist processes is out of the scope of this study and will not be analysed here.

Cyclone centre paths in factor separation simulations are shown in figure 4.2.15. A cyclone centre path for the simulation with the total upper-level PV anomaly removed from the initial conditions (F_PV) is added to the picture. Considering the latter first, we can see that without upper-level PV anomaly in the initial conditions the cyclone initiation point and movement were excessively changed. The shallow cyclone was indeed formed in the lee of the Ahaggar Mountain (refer to figure 4.1.18), dominated by a weak advection of the upper-level PV from the boundary conditions over that area. Thus, the analysis suggests that strong upper-level PV advection is crucial for the cyclogenesis in the lee of the Atlas to occur.

The influence of orography on cyclone paths was clearly resolved the four closest cyclone paths to the Atlas range corresponded to the four simulations with orography included (F1, F12, F13, F123 trajectories in figure 4.2.15). Therefore, in the first place orography tended to move the location of cyclone initiation to the favourable lee area where orographically induced low-level PV and thermal anomalies were the strongest. In addition, it continued to keep the cyclone path deeper inside the lee area. In contrast, inclusion of the upper-level PV perturbation (factor 3) moved the position of the cyclone formation away from the mountain. It seems that the stability of the lower atmosphere on the windward side of the Atlas played an important role in localising the formation place. Namely, in simulations with the upper-level PV perturbation included, the lower atmosphere was less stable underneath. A closer look reveals that in those simulations (F3, F23), cold air parcels on the windward side were able to cross the mountain more efficiently and moved the thermal anomaly more to the south-east. Adversely, in simulations without the upper-level PV perturbation, the low-level stability was stronger and the air was forced to go around the obstacle, creating a thermal anomaly deeper inside the mountain lee. Diffluence of the cyclone paths in simulations with a variable intensity of the upper-level PV anomaly indicates that upper level dynamical factors have a potential to account for the variability of the cyclone paths towards the Mediterranean Sea. Inspection of the cyclone path in the simulation with orography and upper-level PV perturbation (F13) included showed that the cyclone ran into the orographic obstacle on the way to the Mediterranean Sea. The associated land-rise (hill) the cyclone crossed was almost 500 meters, and was not experienced in other simulations of interest (f0, f1 and

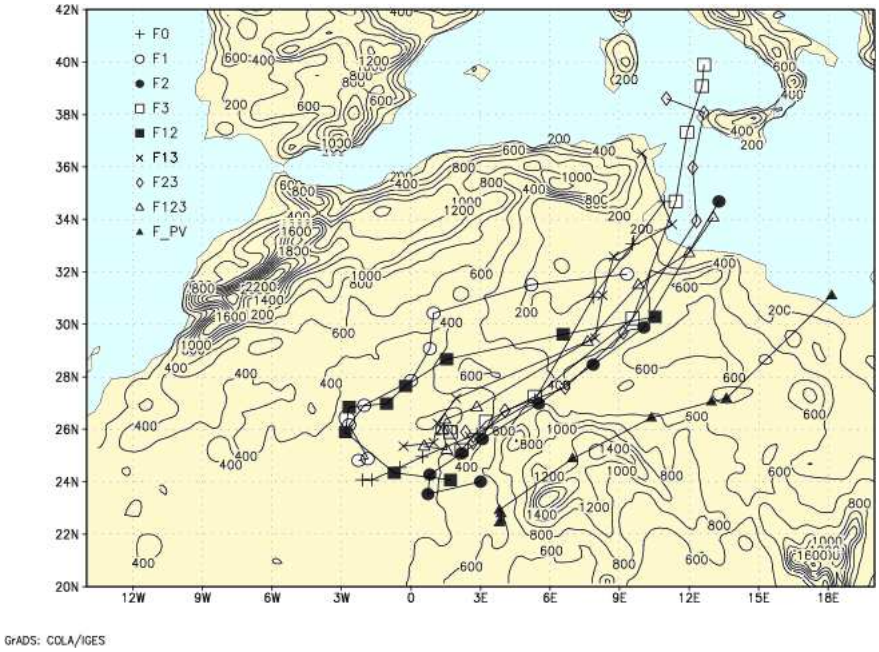

Figure 4.2.15: Simulated trajectories of the different simulated cyclones. On F0 (equivalent to f_0 in equation 2.3.4), F1 (f_1): simulation only with the topography, F2 (f_2): only SSHF, F3 (f_3): only PVp, F12 (f_{12}): without PVp, F13 (f_{13}): without SSHF, F23 (f_{23}): without top orography, F123 (f_{123}, control simulation): with the three factors, F_ PV: simulation without the entire upper-level PV anomaly PVp. Symbols denote position of the cyclone every 6 hours

f3, refer to equation 2.3.4) to such an extent. Thus, this unique cyclone path, and the destruction over the hill could have been the reasons for the strong cyclolytic influence the analysed synergy tended to produce. This idea qualitatively resembles the studies on tropical cyclones passing over the island terrain (g.e. Bender et al., 1987) that reported a strong cyclone filling as the cyclone passes the land disturbance. However, this cyclolytic influence lasted for 18 hours and it is not clear whether this type of orographically induced cyclone filling can be held responsible for the cyclolysis in the whole period.

There were significant differences noted in the times the cyclone reached the Mediterranean Sea. The two slowest cyclones were attached to orographically (f1, f12), while the two fastest ones to upper-level potential vorticity dominated simulations (f3, f23). As expected, sensible heat flux did not have a significant impact on the cyclone track variability. The aforementioned strong dependency indicates that the orographic influence was to keep the cyclone in the mountain lee, while upper-level potential vorticity induced a faster advection of the low-level pressure system to the Mediterranean Sea.

Chapter 5

Medicanes: Tropical-like Mediterranean storms

Articles on which this chapter is based:

L. Fita, R. Romero, a. Luque, K. Emanuel and C. Ramis, 2007: *Analysis of the environments of seven Mediterranean tropical-like storms using an axisymmetric, nonhydrostatic, cloud resolving model*, Nat. Hazard. Earth Sys., **7**, 41-56

L. Fita, R. Romero and C. Ramis, 2008: *Sensitivity study of Mediterranean tropical-like storms. part I: Sensitivity of air-sea mechanism in three storms*,Ann. Geophys., **submitted**

L. Fita, R. Romero and C. Ramis, 2008: *Sensitivity study of tropical-like storms. part II: Verification, dynamics and structure of January 1995 medicane*,Ann. Geophys., **submitted**

Different studies have revealed the existence of tropical-like storms evolving in the Mediterranean basin (in the following, the 'medicane' [Medi-*terranean*+*Hurri*-cane] term is adopted to refer to these systems). A rounded cloud structure surrounding a cloud free area in the centre associated with strong winds, heavy precipitation and high vorticity is a common aspects of medicanes. These are rare cases, however since, about 40 cases during the last 25 years allover the Mediterranean basin have been detected from satellite images and bibliography done by the *Grup de Meteorologia* of *Deparatament de física* of the *Universitat de les Illes Balears* (a web page[1] has been prepared with animations of satellite pictures of the detected cases). Some of the cases have been previously analysed and studied from different perspectives and using different techniques (Rasmussen and Zick, 1987; Businger and Reed, 1989; Lagouvardos et al., 1999; Pytharoulis et al., 2000; Reed et al., 2001; Homar et al., 2003b). Conclusions obtained from these studies reflected the singularity of the characteristics of the phenomena in the Mediterranean basin. Despite its low occurrence, this type of strong cyclogenesis over open sea areas has an important interest due to its potential destructiveness and the high populated Mediterranean coastal line.

Since the initial description of a tropical storm occurred South of the Sicilian Island done by Ernst and Matson (1983), different studies have been devoted to medicanes. Rasmussen and Zick (1987) provided a satellite-based description of a medicane occurred at the end of September 1983. Moreover, through the analysis of soundings they verified the warm core structure of the system and made the hypothesis about the important role of the sea surface temperature (SST) and the strong convective activity associated to these phenomena. Businger and Reed (1989) classification of the small and strong vortex generation associated to a cold air mass gave a first main frame of these kind of phenomena. The term 'polar low' was applied to those extratropical small and deep cyclones originated in sea areas related to a cold upper level air mass or synoptic disturbance. Medicanes were classified as a subclass of "polar low" developed in the Mediterranean basin. They associated this phenomena to an upper level low with a strong convective activity induced by a warm sea from which strong heat and moist surface fluxes were generated. Basically, on a pre-existing high convective and cyclonic environment, convection is enhanced by the existence of an upper level cold low. Self organisation of the convection around a small vortex contributes to the formation of a deep and small cyclone enhancing convection mechanism. Instead of the baroclinic aspects of the Mediterranean basin, the initial studies of medicanes related the evolution of these systems to convective processes, more typical from tropical environments. By this way, the evolution and maintenance of these systems was supposed to be a combination of different mechanisms such as baroclinicity, conditional instability of second kind (CISK), air-sea interaction and barotropy.

The application of atmospheric limited area numerical models gave the opportunity

[1] `http://www.uib.es/depart/dfs/meteorologia/METEOROLOGIA/MEDICANES/`

to confirm such theories. These models are able to simulate medicane systems with a pretty good correspondence with the observations, helping to describe the evolution of the storms over the data-avoided oceanic areas. As examples, ETA and RAMS models were used by Lagouvardos et al. (1999), UK Met. Office Unified Model for the same case by Pytharoulis et al. (2000), and MM5 simulations were done for two cases: January 1982 (Reed et al., 2001) and September 1996 (Homar et al., 2003b). Warm core evidences of the systems are obtained from these simulations as well as characteristic radial wind profiles. Exploiting the flexibility of the numerical models, sensitivity studies can be carried out in order to verify observational hypotheses and to obtain a better understanding of the phenomena. Sensitivity tests of the storms (Lagouvardos et al., 1999; Reed et al., 2001; Homar et al., 2003b) confirm the important role of the different mechanisms theoretically emphasised for the medicane formation and evolution. A large set of parameters have been tested: diabatic processes such as latent heat release from convection and latent heat flux from the sea (hereafter, LHF) are key mechanisms in the medicane; sensible surface heat flux (hereafter, SSHF) and SST played also an important role in the medicane evolution; Homar et al. (2003b) showed an evolution of the September 1996 medicane initially dominated by upper level induced mechanisms and a second phase dominated by LHF and diabatic processes. Reed et al. (2001) revealed a high sensitivity of the simulation of the January 1982 case to the initial conditions (as an initial surface vortex). These same studies have revealed that these Mediterranean systems can have the strength of a tropical storm (more than 33 ms^{-1}).

Previous described observational sparse model-based studies revealed that principal reinforce mechanisms of medicanes are related to sea surface temperature and the presence of an upper level anomaly (Rasmussen and Zick, 1987). The use of present nonhydrostatic models operated at higher resolution than older ones should be able to confirm and reveal new fine and deep structures of these systems. Such studies like (Lagouvardos et al., 1999; Pytharoulis et al., 2000; Reed et al., 2001; Homar et al., 2003b) also presented a strong small vortex related to heavy precipitation and a warm core. These studies also confirm main mechanisms of reinforce and maintenance such as: strong diabatic processes related to vigorous and deep convection, latent heat release from cloud formation at middle altitudes, vigorous latent heat fluxes from the sea and the initial driven role of the baroclinicity due to a prior upper level cold low. Sensitivity test shown that without latent heating due to the strong convection developed by deep cumulus, these systems can not be developed (Homar et al., 2003b). A lower influence is attributed to surface fluxes and upper level trough, latent heat flux from the sea surface and in lower degree, sensible surface heat flux. Another important role is attributed to the SST value as it is shown by Homar et al. (2003b). Although, uncertinities due to the lack of observations related to maritime characteristics of the systems decrease the success of the simulations of the models (Reed et al., 2001).

Air-sea interaction mechanism (Emanuel, 1986) has also been proposed as responsible for the medicane evolution. However, Mediterranean environment is very different than the tropical one (Reiter, 1975). Maritime Tropical environments exhibit homogeneous atmospheric characteristics over most of the low latitudes region. They are characterised by warm temperatures and high humidities (e.g. mean annual values of temperature and humidity at 1000 hPa for the West Indies are respectively 24.3 $^{\circ}C$ and 79%; Jordan (1958)). Tropical environments show also a low seasonal trend (annual spread of the temperature at all levels is lower than 10 $^{\circ}C$ Jordan (1958)).

Main characteristics of the Mediterranean basin like elevated surrounding orography, small sea and warm and dry air advections from the North African plateau might influence the Mediterranean tropical-like systems. Thus, Mediterranean cases evolve within a more complex environment than the homogeneous tropical one and in order to capture the entire influences due to the complexity of the environment (see figure 1.1.2), their study should be done with full physics primitive equations numerical models like MM5 if an adequate simulation will be obtained (Fita et al., 2007a).

The existence of an upper level cold low above warm and moistened low level air is assumed as the triggering environment from which medicanes are formed (Emanuel, 2005). By this way, medicanes can be developed above sea within a surface temperature (see SST distribution during the January 1995 case in figure 5.0.1) colder than the 26 °C, threshold below which a hurricane can not be formed (Emanuel, 1986).

5.1 Description of studied cases

Seven cases have been studied with different techniques, purposes and methodologies. Each one affected different areas and occurred at different periods of time (see all their trajectories in figure 5.1.1). A general description of the cases has been obtained from the satellite images. The trajectory of the storms is derived through human-base eye localisation. All cases exhibited similar characteristics from the satellite perspective. A highly stormy environment was present during the initial phase of the systems (in some cases, convection with cloud top temperatures as cold as 200 K was observed, not shown). Cloud systems started to gain cyclonic rotational movement meanwhile cloud formation was enhancing. Rotational movement of the clouds increased rapidly and a well shaped circular cloud system was formed. In the centre of the cloud structure, a free cloud area (an eye-like structure) was visible. The hurricane-like aspect of the storm was visible at different periods of the storm evolution, and lasted for different amounts of times (see table 5.1.a, for more details). Then, the storm diminished in intensity and finally disappeared (generally 1 day later), mainly when the storm reached the coast.

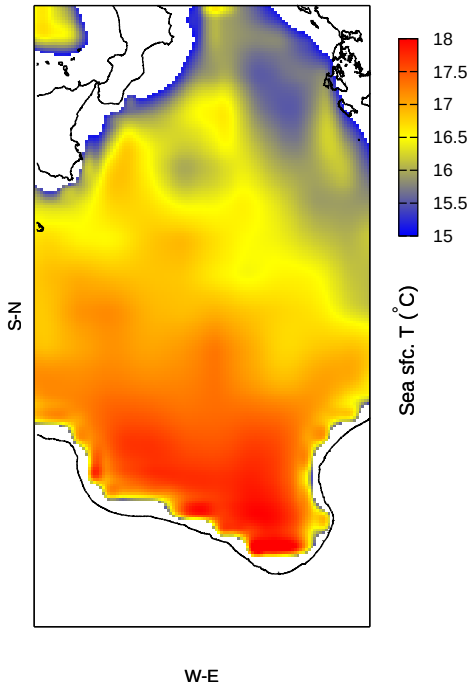

Figure 5.0.1: Sea surface temperature in the zone of evolution of the medicane. It is unchanged during all the period of simulation

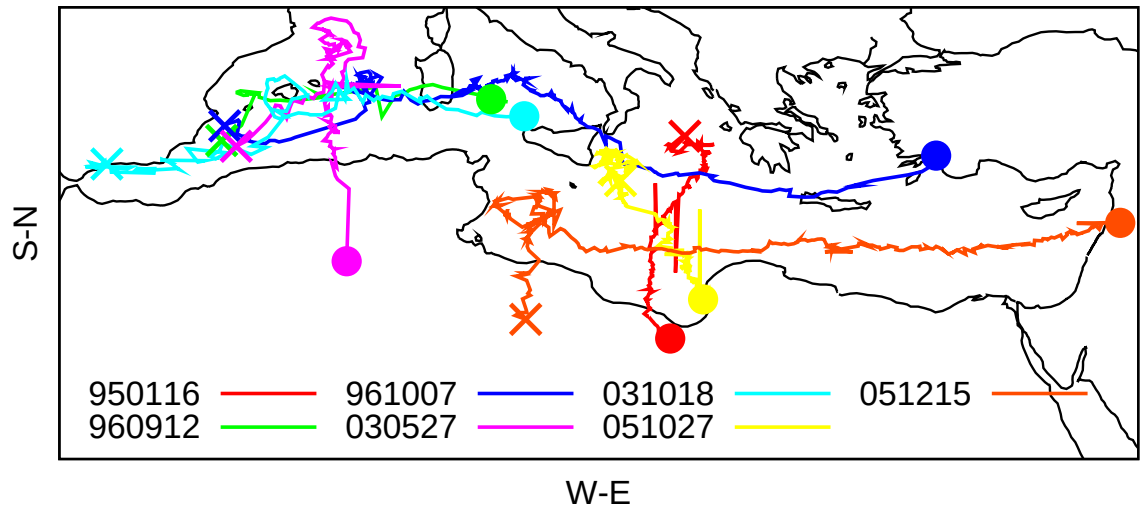

Figure 5.1.1: Storm trajectories derived from satellite imagery. See legend for case-description. Cross beginning of the storm. Full circle end of the storm

All cases presented similar synoptic characteristics (see figures from 5.1.2 to 5.1.9). An upper level trough was present during all the evolution of the cases. At low levels convergence of cold and warm air masses was present in the zone where the medicanes evolved at the initial phase of the cyclones. However, no particularly high relative humidities or deep column positive vorticity values, presumed in the tropical systems, were detected. Synoptic atmospheric environments obtained from ECMWF analyses did not show any particular difference from previous climatological Mediterranean studies of cyclonegensis and cyclone evolution (Reiter, 1975; Campins et al., 2000). 24 hours before the eye formation the environment (see table 5.3.b) was not supportive of strong thunderstorms according to calculated instability indices (Tudurí and Ramis, 1997). The presence in the area of a strong surface horizontal thermal gradient (bottom panels in figures 5.1.3 to 5.1.9) is an indication of the baroclinicity typical of the Mediterranean basin. As has been said, the presence of an upper level trough is assumed to be a necessary aspect to make possible the development of this kind of tropical-like storms (Emanuel, 2005): thermodynamic vertical disequilibrium in which the medicane is rooted is established between relatively high Sea Surface Temperature (SST) and the cold air associated with the upper level cold low. Thus a medicane might reflect the combination of two different storm genesis mechanisms: strong convection due to the vertical thermodynamic disequilibrium characteristics of tropical systems, and the baroclinic mechanism typical of the Mediterranean latitudes (Fita et al., 2007a). Meanwhile the coldest SST from which a hurricane can be formed is 26°C (Emanuel, 1986), SST in January 1995 case in figure

Table 5.1.a: Selected environments related to a tropical-like Mediterranean storm. First col. indicates label storm. 2^{nd} col.: Storm initial date (on [DD]/[MM] $[HH]^{[MI]}$ format), 3^{rd} col.: Storm ending date, 4^{th} col.: Eye beginning, 5^{th} col.: Eye ending

case	**Storm Beg.**	**Storm End**	**Eye Beg.**	**Eye End**
950116	$14/01\ 12^{00}$	$18/01\ 20^{00}$	$15/01\ 07^{00}$	$18/01\ 06^{30}$
960912	$11/09\ 21^{00}$	$13/09\ 02^{30}$	$12/09\ 07^{30}$	$12/09\ 12^{00}$
961007	$06/10\ 03^{30}$	$11/10\ 03^{00}$	$07/10\ 05^{30}$ $08/10\ 06^{00}$	$07/10\ 06^{30}$ $10/10\ 12^{00}$
030527	$25/03\ 12^{00}$	$28/05\ 04^{30}$	$27/05\ 08^{30}$	$27/05\ 15^{30}$
031018	$17/10\ 00^{00}$	$19/10\ 04^{00}$	$18/10\ 12^{30}$	$18/10\ 13^{30}$
051027	$26/10\ 20^{30}$	$29/10\ 14^{30}$	$28/10\ 10^{00}$	$28/10\ 12^{00}$
051215	$13/12\ 05^{00}$	$16/12\ 12^{15}$	$14/12\ 08^{00}$ $15/12\ 06^{00}$	$14/12\ 15^{15}$ $15/12\ 14^{15}$

5.0.1, for example was only 15.7°C, high enough to activate the air-sea thermodynamic disequilibrium due to the presence of very cold air advected southward by the baroclinic disturbance (see table 5.3.b). Environments related to tropical-like storms are detected in all seasons; however, a great preponderance occurs during Autumn. Studied storms of these environments reached different durations (larger than two days). Some storms travelled large distances (across almost all Mediterranean basin, see figure 5.1.1). All of them showed a high cyclonic rotation and less than 500 km in radius.

January 1995
This case occurred during January 1995 in the south of the Ionic Sea (see figure 5.1.2). In this case the medicane is formed within the area of influence of deep convection that reached the South of Italy and the Albanian coast. In the January 1995 case the eye-wall cloud structure was visible for about 1 day while the system moved southward about 500 km (see table 5.1.a).

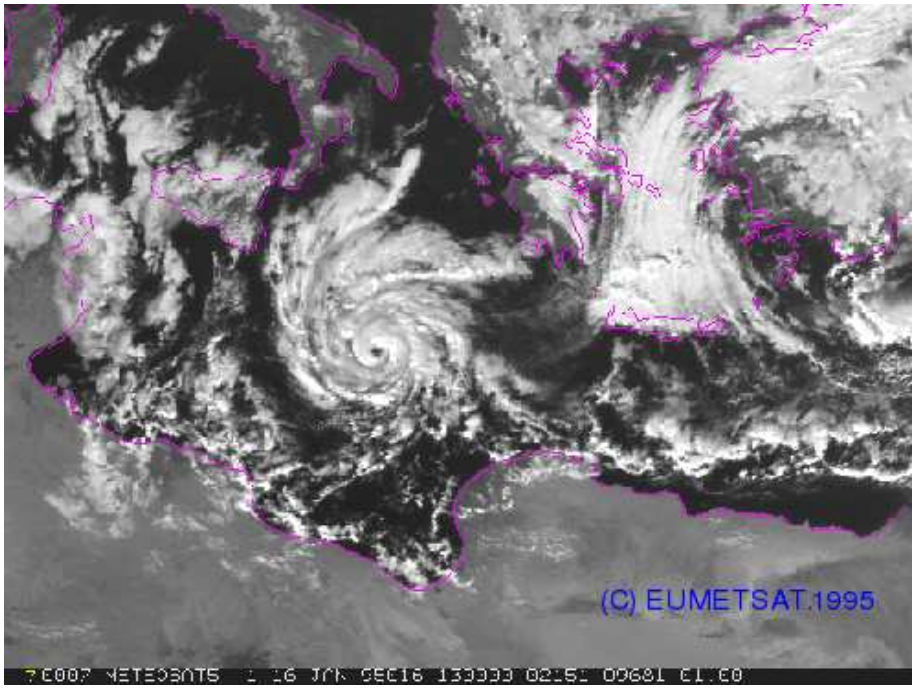

Figure 5.1.2: Main characteristics of the January 1995 medicane case. Normalised satellite visible image channel at maximum intensity moment corresponding to '950116' case on January 16th 1995 at 13^{00} UTC (source METEOSAT-5, top).

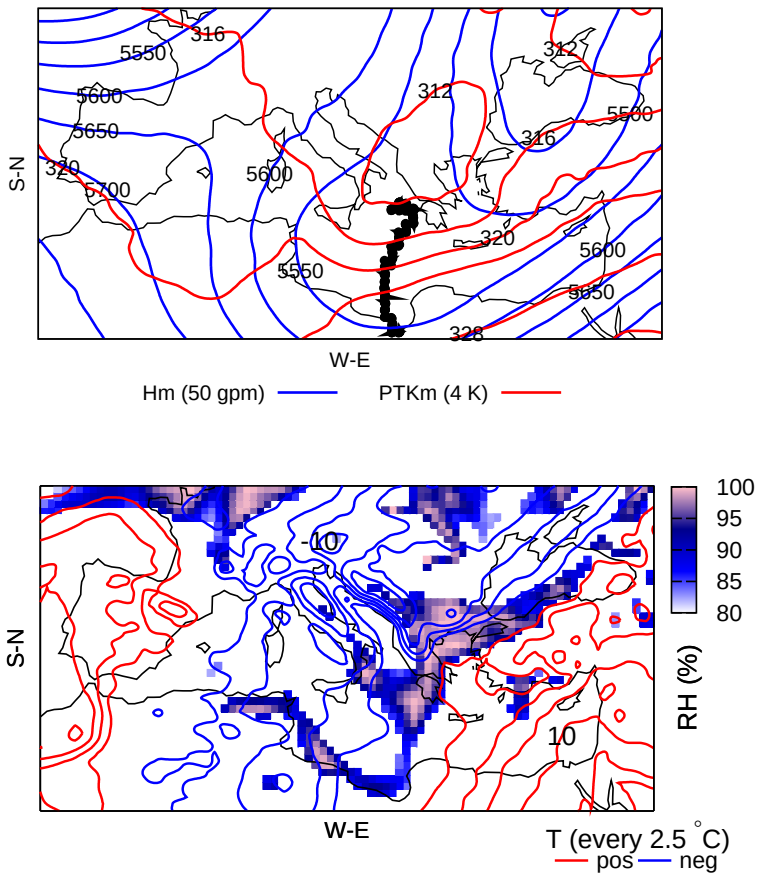

Figure 5.1.3: Main characteristics of the January 1995 medicane case. Top panel: Time averaged ECMWF analysis (during all the storm period see table 5.1.a) geopotential height (500 hPa, blue solid line, every 50 gpm) and time averaged potential temperature (300 hPa, red solid line, every 4 K). Thick solid lines with points showed storm trajectory obtained from satellite images. Bottom panel: Relative humidity at 925 hPa (above 80 %, shaded) and temperature at 850 (red line: positive values, blue line: negative values, every 2.5 $^{\circ}C$) at the beginning of the storm on Jan. 14th at 12^{00} UTC.

September 1996

This case affected the Balearic Islands (see middle panel in figure 5.1.4). Deep convection occurred in the Balearic Sea, between Valencia coast and Balearic Islands, meanwhile a weak cyclonic system was offshore the coasts of Argel. A weak vorticity centre evolved from the south following the Iberian coastal line. When this system reached the convective zone the medicane started to develop. September 1996 case, vanished in one day after it overpassed Sardegna Island.

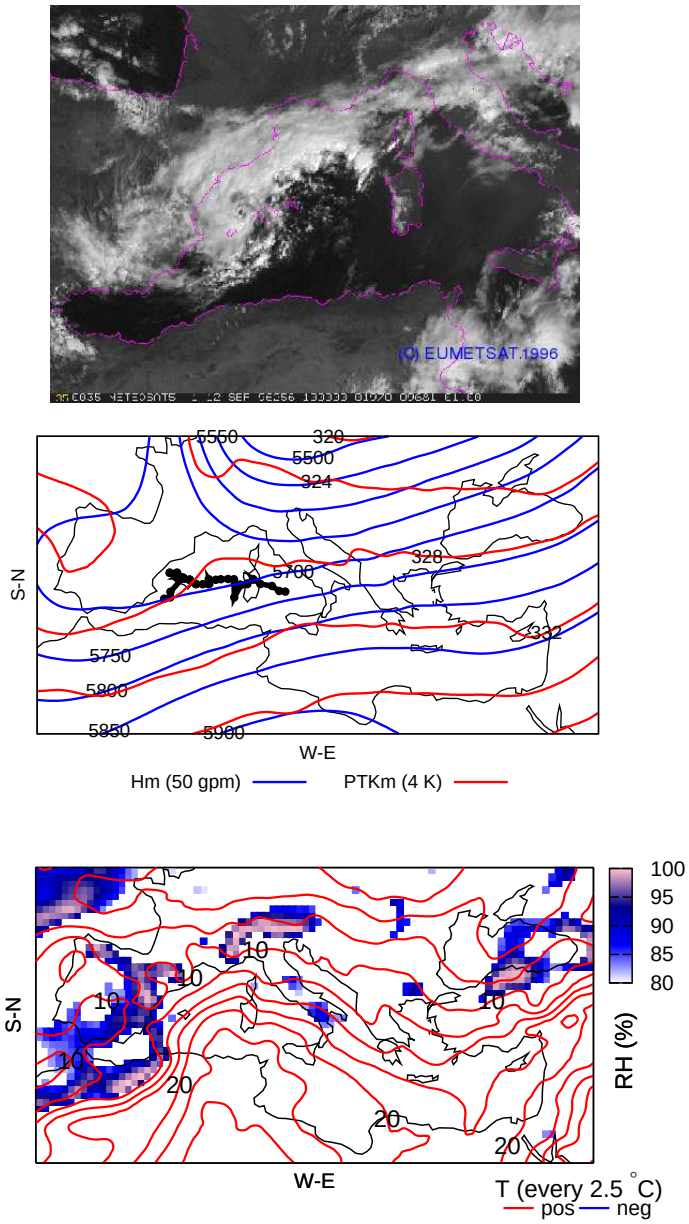

Figure 5.1.4: As in figures 5.1.2 and 5.1.3, but for the September 1996 medicane case. Satellite maximum on September 12th 1996 at 10^{00} UTC (METEOSAT-5, top). Beginning of the storm is on Sept. 12th at 00^{00} UTC.

October 1996

This case started as a storm system Southwest of the Balearic islands. It gained vorticity as it moved westward. Before it reached Sardegna island it shown a clear eye in the centre of spiral clouds. When it was overpassing Sardegna it lost it hurricane-like morphology, that it recovered again when it reached again the Sea between the island and Italy (see table 5.1.a with the two eye-detected period). The system moved south-eastward, overpassed close to the Strait of Messina and died as storm residual system South of the Peloponnese peninsula.

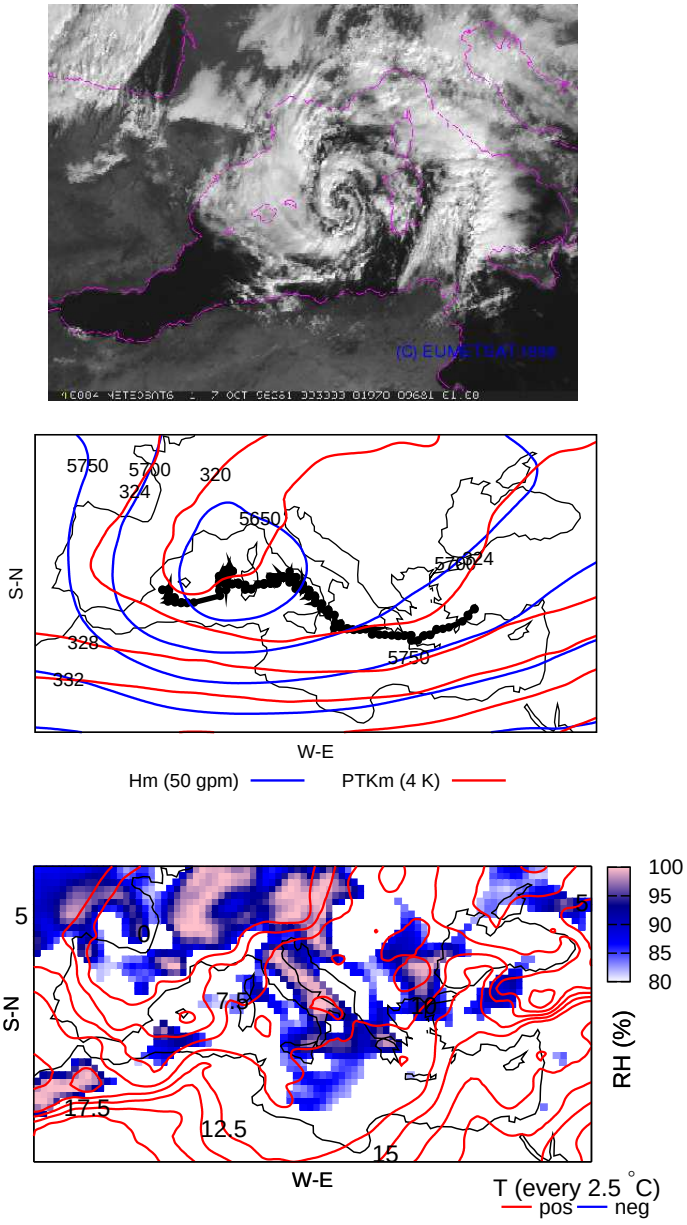

Figure 5.1.5: As in figures 5.1.2 and 5.1.3, but for the October 1996 medicane case. Satellite maximum on October 7th 1996 at 09^{30} UTC (METEOSAT-6, top). Beginning of the storm is on Oct. 6th at 06^{00} UTC.

May 2003

This episode occurred during May of 2003 in the Western Mediterranean basin. A cyclonic system was initially present between North of Balearics and Sardegna Islands. The vortex system evolved from a coma shape cloud structure to a medicane, while moving. Southwards and overpassing Balearic Islands. Strong vorticity of the cloud systems was observed but a cloud free area was not clearly identified.

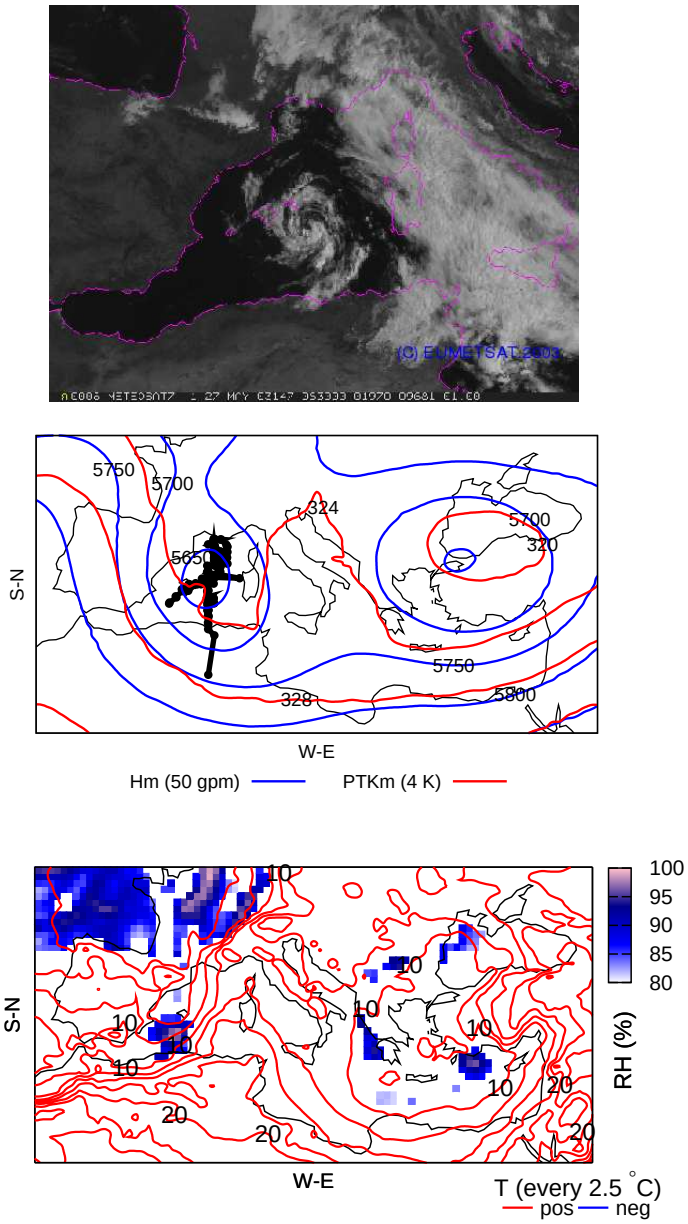

Figure 5.1.6: As in figures 5.1.2 and 5.1.3, but for the May 2003 medicane case. Satellite maximum on May 27th 2003 at 08^{30} UTC (METEOSAT-7, top). Beginning of the storm is on on May 25th at 12^{00} UTC

October 2003

This case developed in the Western Mediterranean basin. A weak vortex initiated to the south of the Iberian peninsula, evolved along the eastern coast of Spain until it reached an area with thunderstorm activity located between Iberian peninsula and Balearic Islands. Later, convective cloud cluster acquired a cyclonic rotation and formed the medicane. It moved westward until it disappeared when it overpassed the Sardegna island.

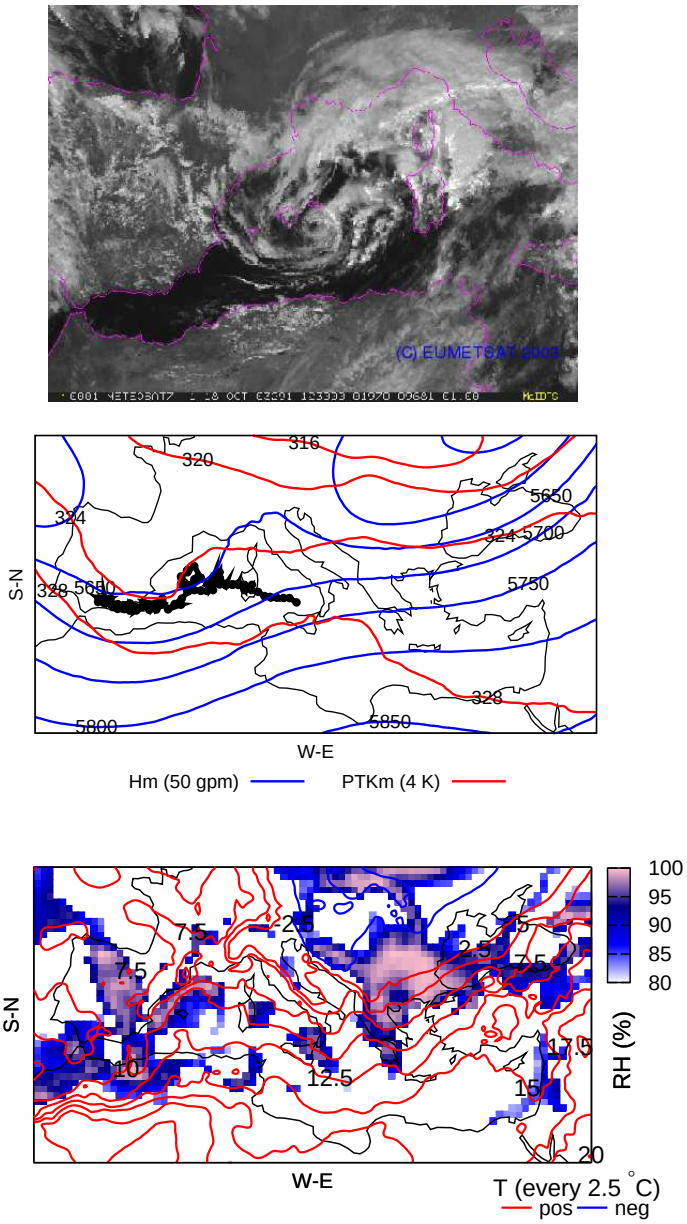

Figure 5.1.7: As in figures 5.1.2 and 5.1.3, but for the October 2003 medicane case. Satellite maximum on October 18th 2003 at 12^{30} UTC (METEOSAT-7, top). Beginning of the storm is on Oct. 17th at 00^{00} UTC.

November 2005

This case started as a strong storm system in the eastern coast of Tunis. It moved north-eastward until the South of the Strait of Messina. It stopped at this point and gained vorticity. Once it started cyclonicity to rotate it moved southward and disappeared in front of the North African coast at the Gulf of Sidra.

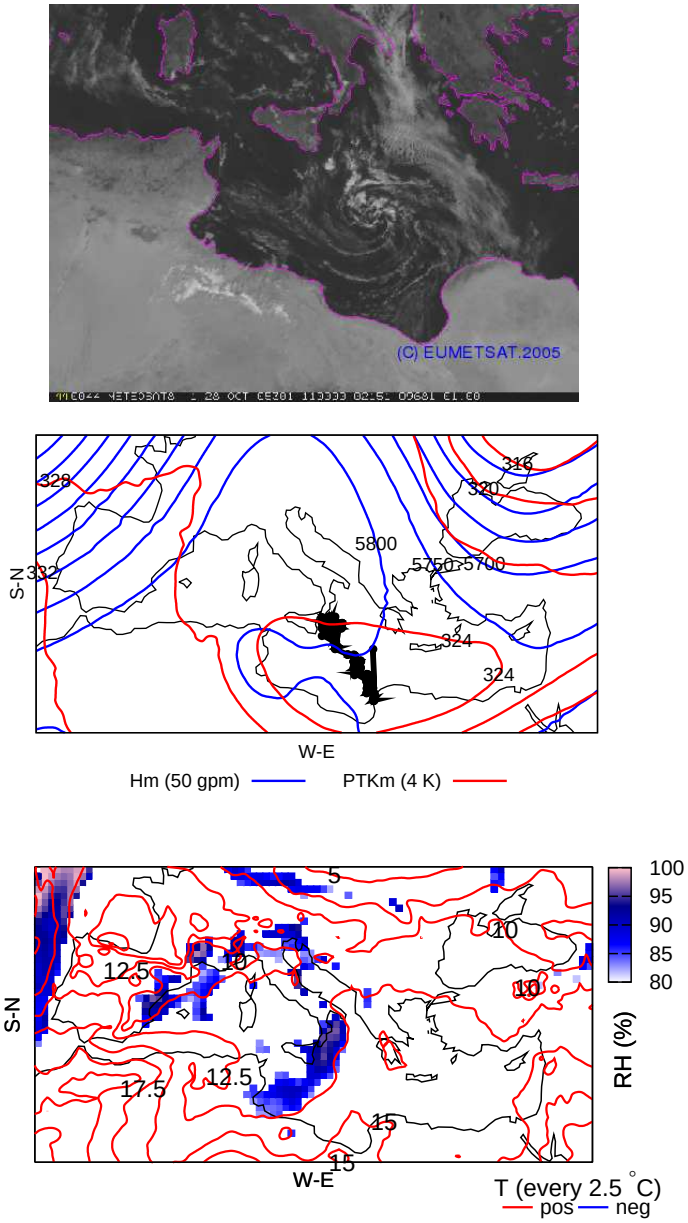

Figure 5.1.8: As in figures 5.1.2 and 5.1.3, but for the October 2005 medicane case. Satellite maximum on October 28th 2005 at 11^{00} UTC (METEOSAT-8, top). Beginning of the storm is on Oct. 26th at 18^{00} UTC.

December 2005

A weak vortex from the inland of North Africa reached a strong storm system located in the eastern coast of Tunis. Storm system acquired cyclonic rotation and moved eastward. Close to the Golf of Sidra round cloud structure with a cloud free centre as an eye was observed. It acquired again the eye-like centre structure when it was moving South of the Crete island (see two eye-formed periods in table 5.1.a). It vanished as storm system when it reached the eastern extreme of the Mediterranean basin.

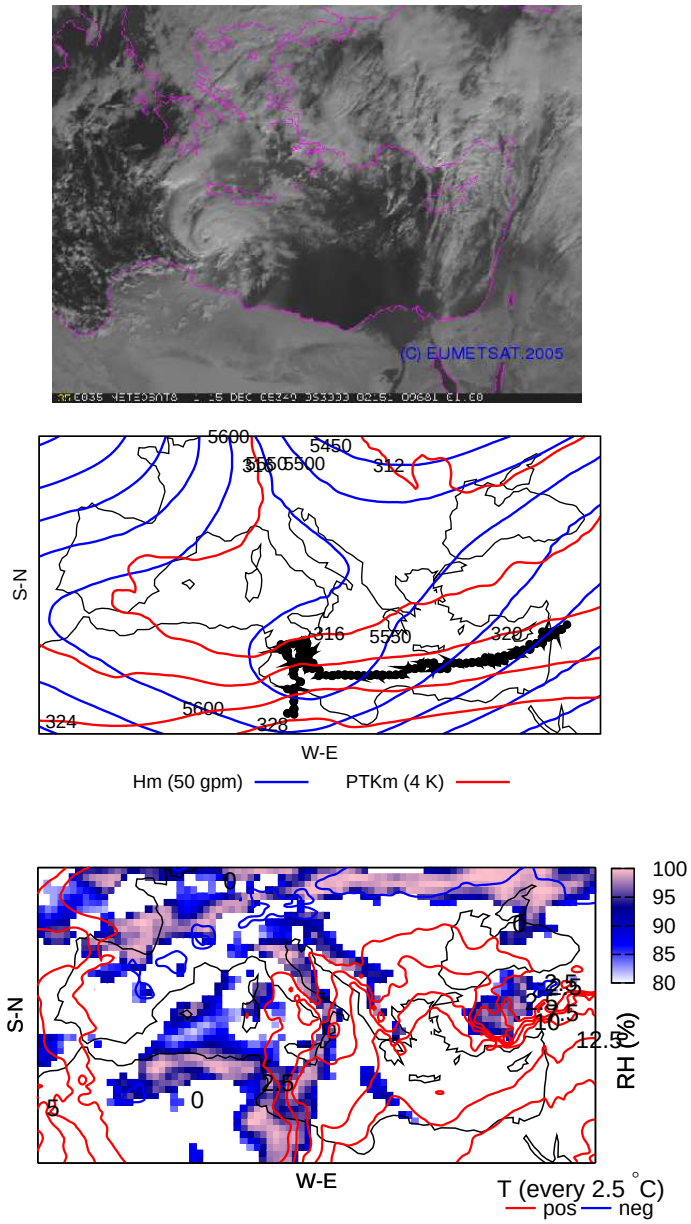

Figure 5.1.9: As in figures 5.1.2 and 5.1.3, but for the December 2005 medicane case. Satellite maximum on 15/12/05 at 08^{30} UTC (METEOSAT-8, top). Beginning of the storm is on Dec. 13th at 06^{00} UTC.

5.2 Air-sea mechanism

Air-sea mechanism (Emanuel, 1986) starts from the assumption that tropical cyclones are developed and maintained by the self-induced strong fluxes of moist and enthalpy originated above sea surfaces. Previous description of formation of tropical cyclones assume that convection was maintained by the moist convergence in the boundary layer of a quasi-balanced vortex (Charney and Eliassen, 1964; Ooyama, 1964). Air-sea mechanism does not assume an environmental CAPE value as the triggering mechanism as in previous descriptions, but it needs a genesis driven by a finite amplitude disturbance as a weak vortex. A feedback is established between radial temperature gradients and radial gradients of sea-air heat transfer associated with gradients of surface wind speed. Transfer of the moist and heat acquired from the Sea surface is driven by cumulus convection. By this way, environment keeps locally neutral to slantwise moist convection. This assumption provides a thermal and kinematic structure of the tropical storm in which combination of buoyant/centrifugal potential of boundary layer air is null. From which is derived a neutral buoyancy of the air in the boundary layer when it lifts along surfaces of constant angular momentum (Emanuel, 1983). It has assumed a well-mixed boundary layer that is inviscid and thermodynamic reversible and the gradient wind approximation can be applied.

Air-sea mechanism describes a tropical mature storm as an axisymmetric structure, with upward constant angular momentum air-parcels trajectories in the free atmosphere and a boundary layer with three distinct regions (eye, wall and outer zone; see schematic representation in figure 5.2.1). Outer zone is characterised by an inward increasing of the azimuthal wind speed with constant surface relative humidity and strong turbulent exchange at the top of the boundary layer. Eye wall zone is depicted as satured air with maximum azimuthal wind speed and strong updrafts (becoming the most responsabile flows for the moist transport instead of the turbulent transport $\overline{(\omega'\theta_E)}_h = 0$ as it is shown in figure 5.2.1). Eye zone is characterised by unsaturated air and subsidence.

The development and maintains of a tropical storm following air-sea mechanism can be described by the trajectory that follows an air particle within a tropical storm. It is assumed that the gain of energy is only obtained from the sea surface. Throughout a constant thermal inward movement to the centre of the storm air particle acquires energy (A-B section of figure 5.2.1). Strong amount of heat and moist is acquired at constant temperature. When the air particle reaches the wall zone it is adiabatically upward decompress transported following constant angular momentum surfaces (B-O section of figure 5.2.1). By radiative Newtonian cooling, air particle loses its heat at the outer part of the storm (O-O' section of figure 5.2.1). Air-mass circulation it would be enclosed by adiabatic compression by turbulent mixing with surrounding air (O'-A section of figure 5.2.1). This description of the energy budget within a tropical storm allows an ideal

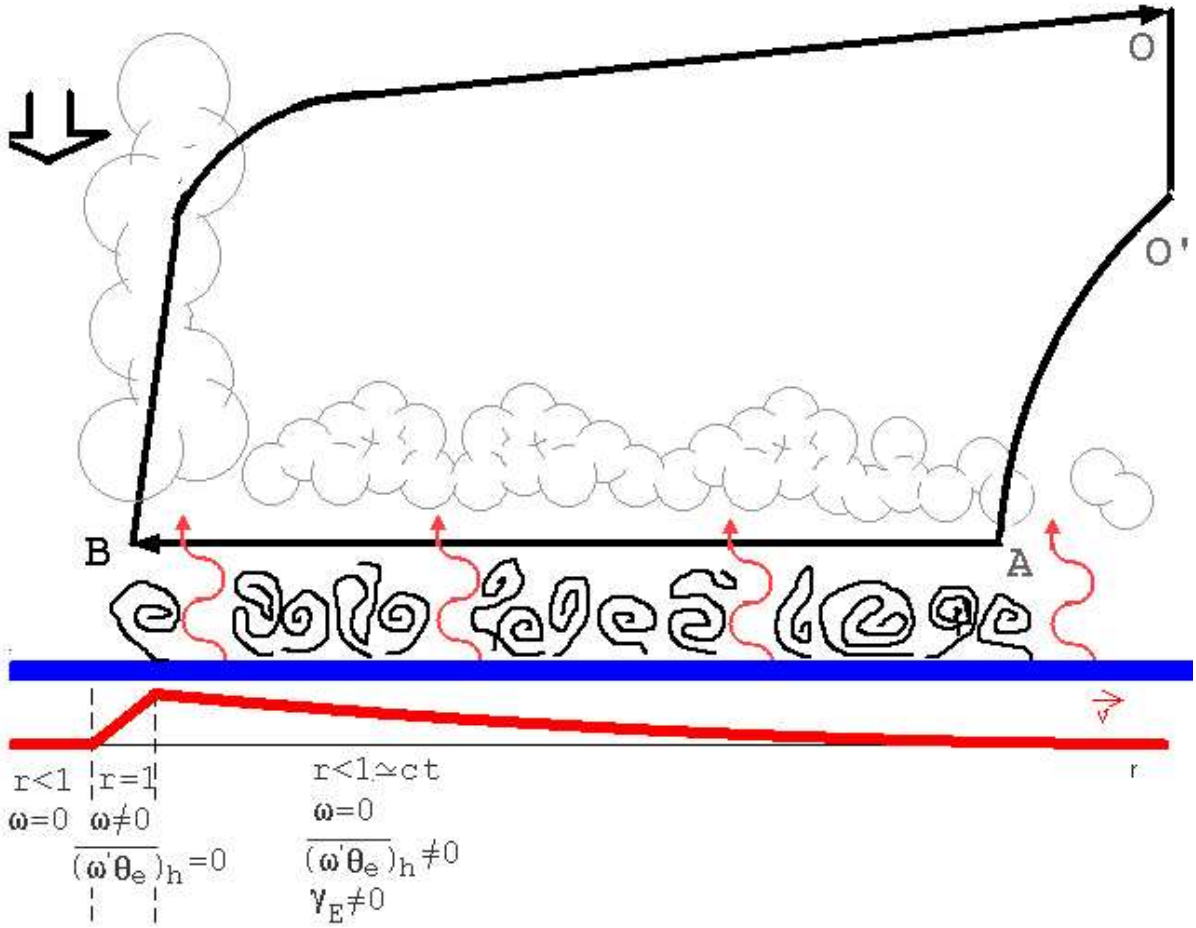

Figure 5.2.1: Radial structure of a tropical steady storm. $\vec{v}$, azimuthal wind (thick red line below); PBL regions (dashed lines, from left to right: eye, wall, outer zone); r, relative humidity; ω, vertical velocity; $\overline{(\omega'\theta_E)}_h$, turbulent vertical transport of moist entropy; γ_E, Ekman pumping

treatment of the storm as a Carnot heat engine (Emanuel, 1986, 1995).

Air-sea mechanism provides a relation between the dimension of the tropical storm, the radius with the maximum azimuthal wind speeds, the pressure fall at the centre of the storm and the thermal relation between the sea surface temperature and the upper level temperature at the outer region of the storm in which the radiative cooling occurred. At the same time provides a 26°C minimum sea surface temperature threshold below which a tropical storm would not be formed.

Main characteristics of the tropical storm according to air-sea mechanism are:

- Radial distribution of moist entropy θ_e

$$\ln \theta_e = \ln \theta_{es} - \frac{C_D}{C_\theta} \frac{1}{C_p(T_B - T0)} \left(V^2 + \frac{1}{2} f r V \right)$$

  where θ_{es}, surface moist entropy; T_B, absolute temperature at the top of the boundary layer; T_0, outflow temperature; f, Fourier.

- Radius length of the storm r_0

$$r_0^{2+2\beta} \approx r_{max}^{2\beta} 2\epsilon \frac{C_\theta}{C_D} \frac{T_B}{T_S} \frac{L q_a^*}{f^2} (1 - RH_{as})(1 + \beta) \tag{5.2.1}$$

  where r_{max}, radius of maximum wind; T_s, surface temperature.

- Wind $|\vec{V}\|$ radial distribution

$$V(r) \begin{cases} V \approx r^{\chi/2} & r < r_{max} \\ V \approx r^{-\beta} & r > r_{max} \end{cases} \tag{5.2.2}$$

$$\chi \equiv \frac{2\left[1 - \epsilon\left(1 + \frac{L q_a^*}{R T_s}\right)\right]}{2\frac{C_D}{C_\theta} - 1} \tag{5.2.3}$$

$$\beta \equiv 1 - \epsilon \left(1 + \frac{L q_a^* RH_{as}}{R T_s}\right) \tag{5.2.4}$$

$$\epsilon \equiv \frac{T_B - T_0}{T_B} \tag{5.2.5}$$

  where C_D/C_θ, Ratio exchange coefficients; q_a^*, saturated mixing ratio of the ambient; RH_{as}, relative humidity of the ambient at the surface;

- Eye-pressure

$$\ln \pi_{cs} \simeq \frac{-\left(\frac{T_B - \overline{T}_{out}}{T_B}\right) \frac{L q_a^*}{C_p T_S} (RH_c - RH_a)_s + \frac{1}{4} \frac{f^2 r_0^2}{C_p T_B}}{1 - \left(\frac{T_B - \overline{T}_{out}}{T_B}\right) \left(1 + \frac{L q_a^* RH_{CS}}{R T_S}\right)} \tag{5.2.6}$$

where $\overline{T}_{out}$, weighted averaged outflow temperature; RH_c, relative humidity at the centre, RH_{cs}, surface relative humidity.

- V max

$$V_{max}^2 = \frac{C_\theta}{C_D}\epsilon L q_a^*(1-RH_{as})\frac{1-\frac{1}{4}\frac{f^2r_0^2}{\beta RT_B}}{1-\frac{1}{2}\frac{C_\theta}{C_D}\epsilon\frac{Lq_a^*(1-RH_{as})}{\beta RT_S}} \tag{5.2.7}$$

- pressure distribution

$$\ln\pi = \frac{-\frac{1}{2}\epsilon\frac{C_\theta}{C_D}\frac{Lq_a^*}{C_pT_B}(1-RH_{as})+\frac{1}{4}\frac{f^2r_0^2}{C_pT_B}}{\beta-\frac{1}{2}\frac{C_\theta}{C_D}\epsilon\frac{Lq_a^*}{RT_s}(1-RH_{as})} \tag{5.2.8}$$

5.3 Sensitivities of Medicane environments with cloud model

Medicanes have a structure similar to that of tropical systems. Thus a numerical model for tropical systems (Rotunno and Emanuel, 1987) is used to study a collection of 7 Mediterranean atmospheric environments related to tropical-like cases (see description in figures 5.1.2 to 5.1.9). Cloud model simulations will be used as a tool to study the Mediterranean environments in which seven medicanes were formed and to examine the limitations arising from the model assumptions. It is not attempted to simulate the real cyclones, but rather to assess the potentialities of the environments to support this kind of extreme windstorms. The model is an axisymmetric cloud resolving model employed to simulate under idealised, homogeneous conditions, tropical systems such as hurricanes and tropical storms. The results of the numerical simulations allow one to determine similarities and differences between the storms in the Tropical and Mediterranean environments. The air-sea interaction theory of tropical cyclones shows that the steady-state of these storms can be idealised by a Carnot engine, with good agreement between the theoretical maximum wind speed (or potential intensity) and observed values in the Tropics. However, the Mediterranean basin (Reiter, 1975) presents characteristics significantly different from those of tropical regions (Jordan, 1958; Emanuel, 2003) and different results might be obtained in the real Mediterranean environment.

The effect in the simulated medicane of the sea surface temperature, dimension and strength of the initial perturbation from which the medicane will grow, and the stability of the air (Emanuel, 2003, 1986) will be analysed with the cloud model (see section 2.1.2).

Moreover, a recent study (Romero and Emanuel, 2006), applied an empirical index of tropical cyclone genesis to the medicane cases. The results showed systematically high values of the index for all the events and therefore its value as a forecasting parameter. The index is based, among other environmental factors, on the potential intensity (or maximum attainable wind speed) of tropical cyclones derived from the air-sea interaction theory (Emanuel, 2003). The theoretical potential intensity (Bister and Emanuel, 1998) can be compared with the -simulated and observed- intensity of the selected medicane events.

The seven environments for this study have been selected from satellite imagery and previously published papers on tropical-like storms. That is, these events have been selected because they exhibited in the satellite visible channel a rounded and clear-eye cloud structure (see figures 5.1.2 to 5.1.9). As it has been mentioned, more than seven cases (Lagouvardos et al., 1999) have been detected. However, only the cases for which satellite images were accessible at the time of the study could be analysed. Once a storm was selected (see table 5.1.a), the storm was tracked using visible, infrared and water vapour

satellite channels. The storm trajectory was chosen from the centre of the storm, or from the position of the eye (when it was visible). The formation, maintenance and dissipation of tropical-like storms are all of interest to this study. For this reason, the chosen trajectory comprises the entire lifetime of the storm and not only when a clear eye and rounded cloud structure are clearly observed.

Soundings derived from ECMWF analyses have been used to initialise the cloud model. These soundings do not show special environmental aspects (see table 5.3.b). Sea surface temperature (SST) was not warmer than climatological values (Reiter, 1975). Generally, the synthetic soundings exhibit significant instability (values of index CAPE higher than 700 Jkg^{-1}) and high amount of precipitable water in the air column (higher than 22 mm). However, these values are not rare in comparison with characteristic Mediterranean storm situations (Tudurí and Ramis, 1997). Thus, the atmosphere did not show any specific characteristic from which any particular precursor signature of medicane formation could be obtained.

Two types of observation have been also used to complete the general description of medicanes. Synoptic observations and observations derived from satellite measurements have been used. Synoptic observations have been taken from BUFR files from ECMWF (pilot and surface observations). Records within a 1000 km radius from the cloud-eye position have been selected from this database. Due to the maritime characteristics of the medicanes, the information obtained has been very sparse. However, maximum and minimum values showed characteristics of tropical systems (see table 5.3.a). Wind speeds measurements confirmed the tropical storm strength of the medicanes. The lack of synoptic observations over the sea has been alleviated by the use of SSMI or QSCAT satellite-sensors information (SSMI source). Wind derived from satellite images above the sea is obtained. These sensors on board polar-orbiting satellites can measure wind speed remotely from the analysis of the sea roughness in the microwave radiative spectrum area. These data and more information about the sensors and techniques are freely available via the web page `www.ssmi.com` from the Remote Sensing System enterprise. Remote wind speed measures have 25 km spatial resolution over open sea and covers a range of wind speeds from 0 to 33 ms^{-1} for ssmi (50 ms^{-1} on QuikSCAT). See satellite-derived wind for 051215 event on figure 5.3.1.

The control simulation for all the cases covers a 10-day period and the outer radius of the model is set at 1000 km. The initial vortex had an overall radial dimension of 100 km width, and a maximum wind speed of 5 ms^{-1} at 25 km radial distance from the centre. This vortex specification is assumed to be close to the initially weak vortexes observed in the satellite images. Initial atmospheric conditions are taken from ECMWF analyses. A synthetic atmospheric sounding is interpolated from ECMWF analysis 24 hours before the eye formation at the central storm position (see figure 5.3.2). General atmospheric

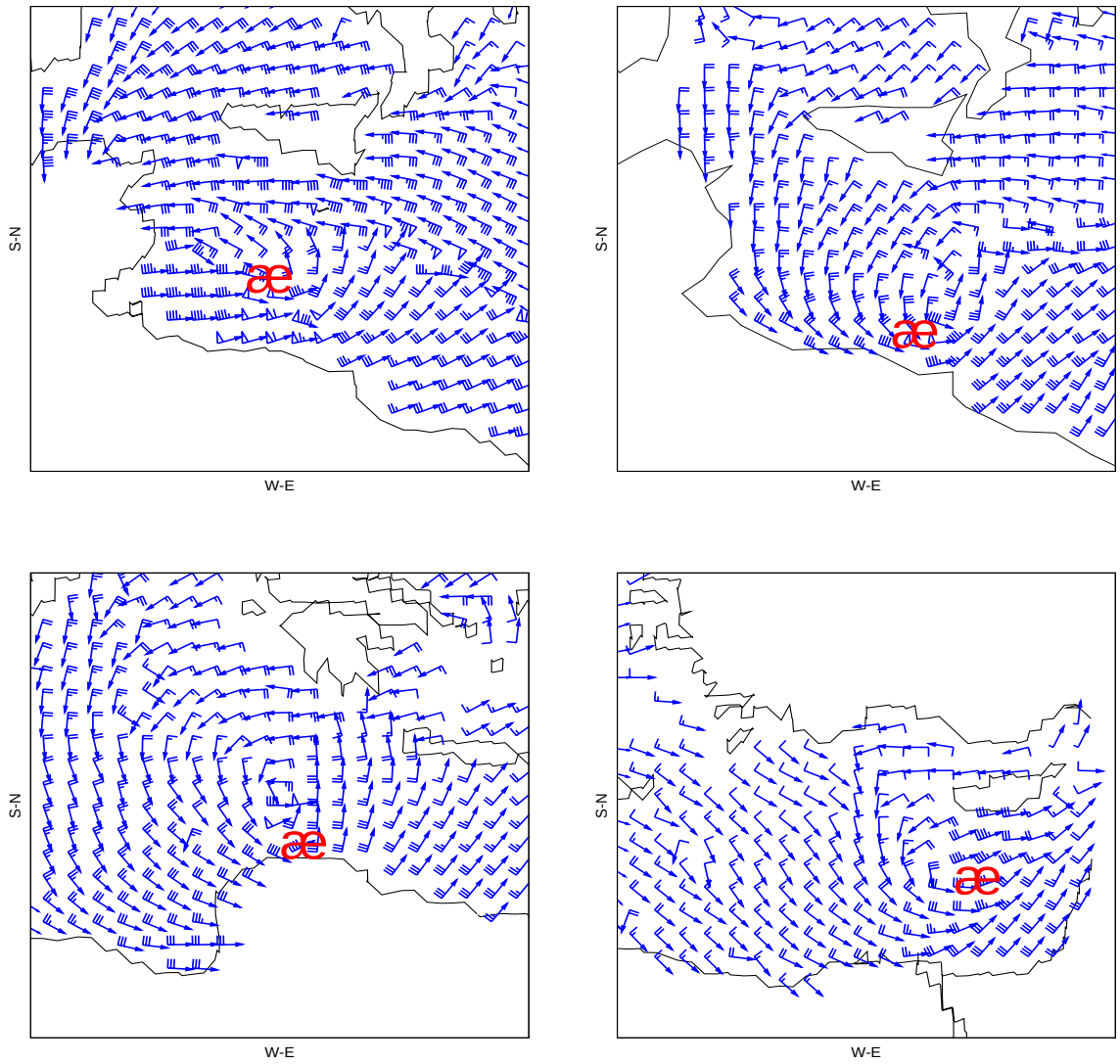

Figure 5.3.1: QuikSCAT satellite wind derived field (every 2 grid points) on 13/12/05 at 17^{30} UTC (top left), 15/12/05 at 14^{18} UTC (top right), 15/12/05 at 17^{06} UTC (bottom left) and 16/12/05 at 03^{54} UTC. Red big æshows centre position of the 051215 medicane on corresponding time observed from Meteosat satellite images. Missed wind derived values correspond with heavy precipitation zones or areas out of the satellite range. æ symbol is proposed as medicane indication (keeping § for hurricane)

Table 5.3.a: Storm observed characteristics (BUFR files-pilot, synop sources- from ECMWF). The selected values corresponded to the maximum values of observations closer than 1000 km to the storm trajectory (when exhibited eye-rounded cloud structure) and date and position of the observation ($[DD]^{[HH]}$; latitude, longitude). Col 1: Case label, col 2: minimal pressure (hPa), col 3: maximum surface wind speed (ms^{-1}) and col 4: maximum surface temperature (K). Maximum wind (53.0 ms^{-1}) of 961007 storm is perhaps not correct

case	Pmin (hPa)	max sfc. wind (ms^{-1})	max temp. (K)
950116	1009.0 (16^{06}; 35.60,18.40)	26.0 (16^{12}; 35.30,18.70)	13.3 (16^{06}; 35.60,18.40)
960912	998.4 (12^{12}; 39.55,2.73)	24.0 (12^{09}; 40.80,2.20)	24.9 (12^{15}; 38.28,-0.55)
961007	1004.8 (07^{06};39,87,4.23)	19.0 (07^{12};37.30,5.6)	17.4 (07^{12}; 37.30,5.6)
	997.0 (09^{00}; 40.30,12.40)	53.0 (09^{06}; 38.20,15.55)	24.1 (09^{09}; 39.10,9.52)
030527	1012.5 (27^{09}; 39.87,4.23)	13.0 (27^{18};37.2,3.50)	21.7 (27^{12}; 39.55,2.73)
031018	1024.0 (18^{12}; 39.87,4.23)	13.0 (18^{12};37.10,4.3)	22.1 (10^{18}; 37.10,4.30)
051027	1021.2 (28^{18}; 35.0,16.0)	5.0 (28^{18};35.0,16.0)	23.1 (28^{18}; 35.0,16.0)
051215	991.0 (14^{06};35.5,12.6)	25.0 (14^{12}; 33.5,13.3)	19.7 (14^{13}; 35.5,12.6)
	993.5 (15^{12}; 33.6,24.9)	18.0 (15^{12}; 33.6,24.9)	17.6 (15^{12}; 34.1,25.7)

conditions are presented in table 5.3.b. Sea surface temperature is also obtained from the ECMWF analyses. ECMWF SST is based on daily NCEP SST analyses generated from ship, buoy and satellite observations (see more information on ECMWF web page `http://www.ecmwf.int`)

General results from the cloud resolving model emphize the potentiality of the environments to support medicanes, but the simulation features are in low agreement with observations. Generally, the model simulations overestimate storms characteristics (see figures 5.3.3 and 5.3.4, as example for all the cases). Simulated storms become much stronger than the observed ones, having deeper cores, stronger winds and wider eye structures. Moreover, simulated storms form and evolve more slowly than the observed ones and do not show any signs of dissipation over the ten-day period.

A numerical evaluation is carried out comparing the winds derived from satellite measurements (SSMI or QUICKSCAT) to the simulated ones. The radial distribution of the winds is divided in radial sections about 12.5 km. For each section an average wind speed is calculated. Numerical simulations overestimate storm strength. In order to obtain a more adequate intercomparison, wind values are not taken when the simulated storm is steady state. Simulated wind values are taken at different time-steps according

Table 5.3.b: Sounding main characteristics for each case [DD]/[MM] $[HH]^{[MI]}$, at ([latitude], [longitude] position), and **SST**: Sea surface temperate (K), **C**: Cape (J/kg), **Sh**: Showalter index (C), **PW**: Precipitable water (mm), **C15**: Convective Instability between 1000 and 500 hPa layers (deg.), **SRH**: Storm relative helicity (m^2s^{-2}), **T15**: Thickness between 1000 and 500 hPa layers (m).§, soundings not corresponding to time storm position, because at this time storm was over land. † null Cape is undetermined because of humidity numerical overestimation at some verticals levels of the sounding

case	**S. date (lat., long.)**	**SST**	**C**	**Sh**	**PW**	**C15**	**SRH**	**T15**
950116	14/01 12^{00} (37.9, 18.9)	15.7	27.8	4.28	15.8	1.8	-16.3	5348
960912	12/09 $00^{00,\S}$ (38.3, 1.2)	24.3	1840	0.38	41.0	-13.5	79.3	5647
961007	06/10 06^{00} (38.4, 1.2)	22.0	1284	0.92	20.6	-10.8	-141.3	5439
	07/10 12^{00} (40.4, 6.3)	20.9	932	0.57	24.9	-9.4	-46.2	5503
030527	26/05 06^{00} (42.4, 4.3)	17.1	$0.0^{\dagger}$	2.36	25.4	2.3	1077	5493
031018	17/10 $12^{00,\S}$ (37.2, -0.7)	22.3	946.9	-1.56	33.9	-8.4	-63.6	5544
051027	27/10 12^{00} (30.8, 12.6)	25.6	1043	-2.08	30.5	-12.6	8.9	5621
051215	13/12 12^{00} (33.8, 12.6)	20.1	376.5	-0.71	22.0	-5.5	43.2	5439
	14/12 06^{00} (35.6, 13.8)	18.2	0.1	3.27	18.4	-0.4	43.7	5462

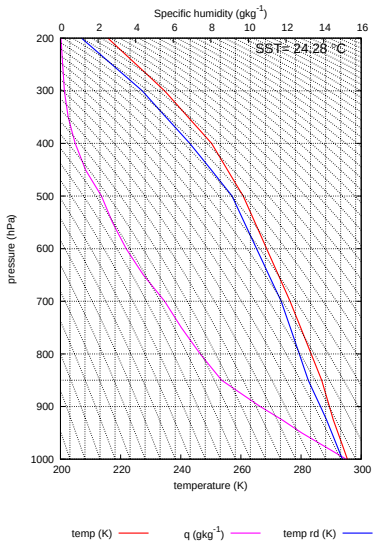

Figure 5.3.2: Synthetic sounding from ECMWF analysis used to simulate the environment labelled '960912'. bottom x-axis temperature (K), y-axis pressure (hPa), top x-axis water content (gkg^{-1}). Dry temperature (red line), dew point temperature (blue line), water content (pink line). SST (Sea Surface Temperature, $°C$)

to the time when maximum wind speeds are reached and are maintained above different thresholds. It has been taken the simulated values at the 4^{th} day of simulation (reached maximum winds about 20 ms^{-1}), the 5^{th} day (reached maximum winds about 25 ms^{-1}) and the 6^{th} day (reached maximum winds about 30 ms^{-1}). Winds derived from satellite measurements are taken when the eye of the storm is observed. A radial distribution of the derived winds is assumed and the distribution is positioned at the centre of the eye. The combined results do not show a good agreement between satellite measurements and model results (see figure 5.3.5). Intensity and decay of the wind profile are underestimated by the model. This disagreement may come from the low satellite grid resolution, sparse satellite data, irregular temporal resolution due to the polar orbit tracks, the failure of the model to simulate the systems adequately and/or subjectivity of the arbitrary choice of the time at which the intercomparison is made.

In order to understand modelled medicane behaviour, sensitivity tests are performed. A value of 26 $°C$ is often indicated as the coldest SST at which a hurricane can develop in tropical regions (Emanuel, 1986). As has been shown in the Mediterranean cases (see table 5.3.b), the SST does not show a critical value (e.g.: on 950115 case, the SST obtained from ECMWF was 15 $°C$; see SST distribution in 5.0.1). Obviously, at the 'high' latitudes of the Mediterranean region under preceding cold intrusions at mid-upper levels,

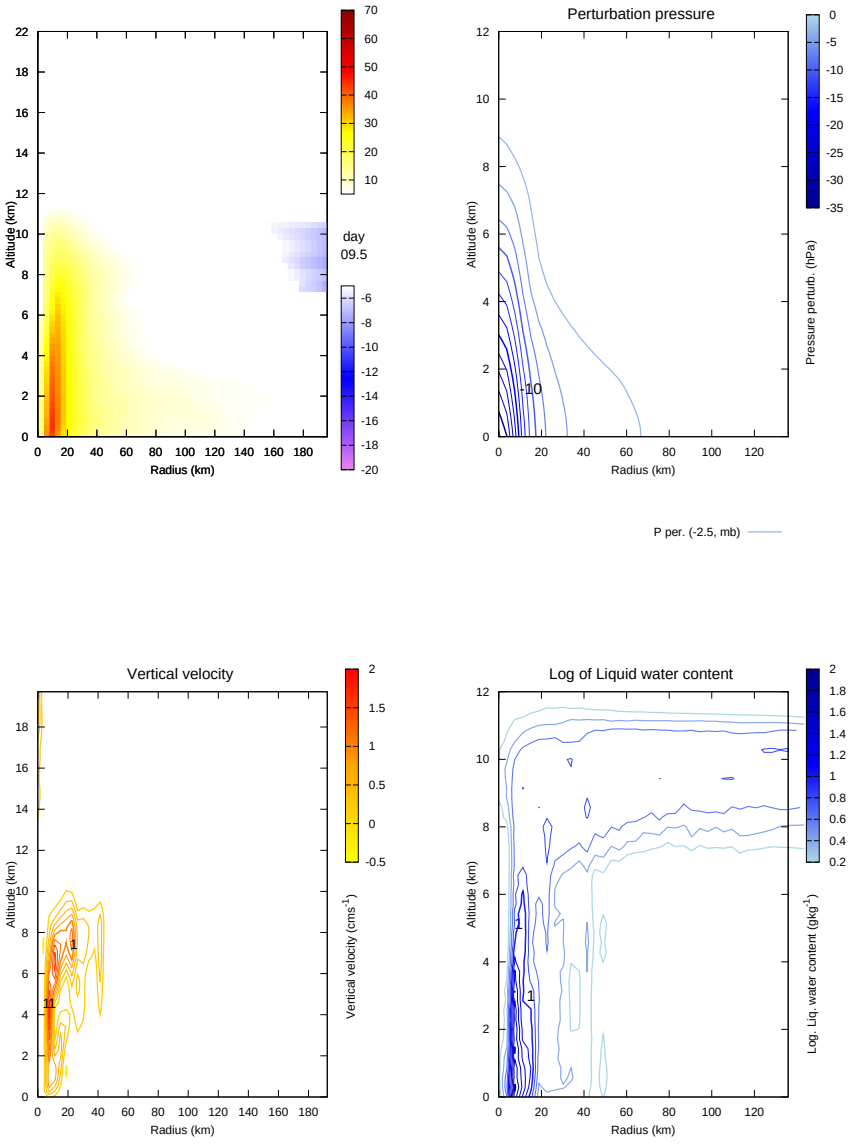

Figure 5.3.3: Simulation results of '960912' storm. x-axis radial distance (km) from storm centre at the left, y-axis height (km). Top left panel: Azimuthal velocity (every 5 ms^{-1}, shaded). Top right panel: Pressure anomaly (every, -2.5 hPa). Bottom left panel: Vertical velocity (every 0.2 cms^{-1}). Bottom right panel: Logarithmic liquid water content (every 0.2 gkg^{-1})

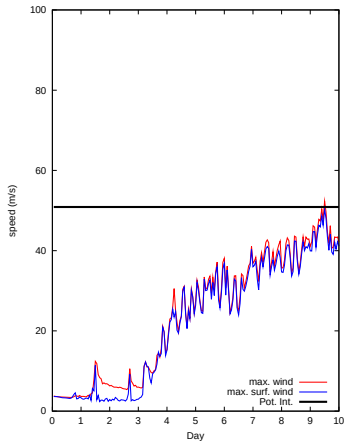

Figure 5.3.4: Evolution of the theoretical potential intensity of the storm (thick black line). maximum wind speed (blue line), and maximum surface wind speed (red line) evolution of the 960912 storm obtained from the model. Day of simulation (x-axis), speed (ms^{-1}, y-axis). Simulation obtained from the 'control' configuration of the initial vortex;$r_{max} = 25\ km,\ v_{max} = 5\ ms^{-1},\ r_0 = 100\ km$ using sounding plotted on figure 5.3.2

the thermodynamic disequilibrium between sea and air can be established with significantly cooler SST values, compared to tropical cases.

To study the sensitivity to the SST, a pair of simulations in which SST has been increased and decreased 5 $°C$ is carried out. It is assumed that the cloud model is able to produce adequate surface fluxes (in concordance to the new SST) after a 'spin-up' time. The study of the sensitivity to the degree of convective instability and moisture content is done by increasing and decreasing 30 % of the humidity value at each point of the sounding used to initialise the axisymmetric model. Previous simulations of tropical cyclones (Rotunno and Emanuel, 1987) do not show an important dependence on the nature of the initial vortex. However, the Mediterranean cases have smaller dimensions (diameter less than 500 km), for which the size of the initial vortex might play an important role. For this reason, a sensitivity test is also carried out by changing the dimension of the initial vortex. In one simulation the initial vortex has been reduced ($r_{max} = 15\ km,\ v_{max} = 5\ ms^{-1},\ r_0 = 50\ km$). In the other simulation, the vortex has been enlarged ($r_{max} = 25km,\ v_{max} = 5\ ms^{-1},\ r_0 = 500\ km$). Another simulation test has been run by changing the surface temperature distribution of the initial vortex. From potential vorticity theory, it is known that positive thermal anomalies are associated with a cyclonic movement of the air around its area (Hoskins et al., 1985; Thorpe, 1986). Thus, in order

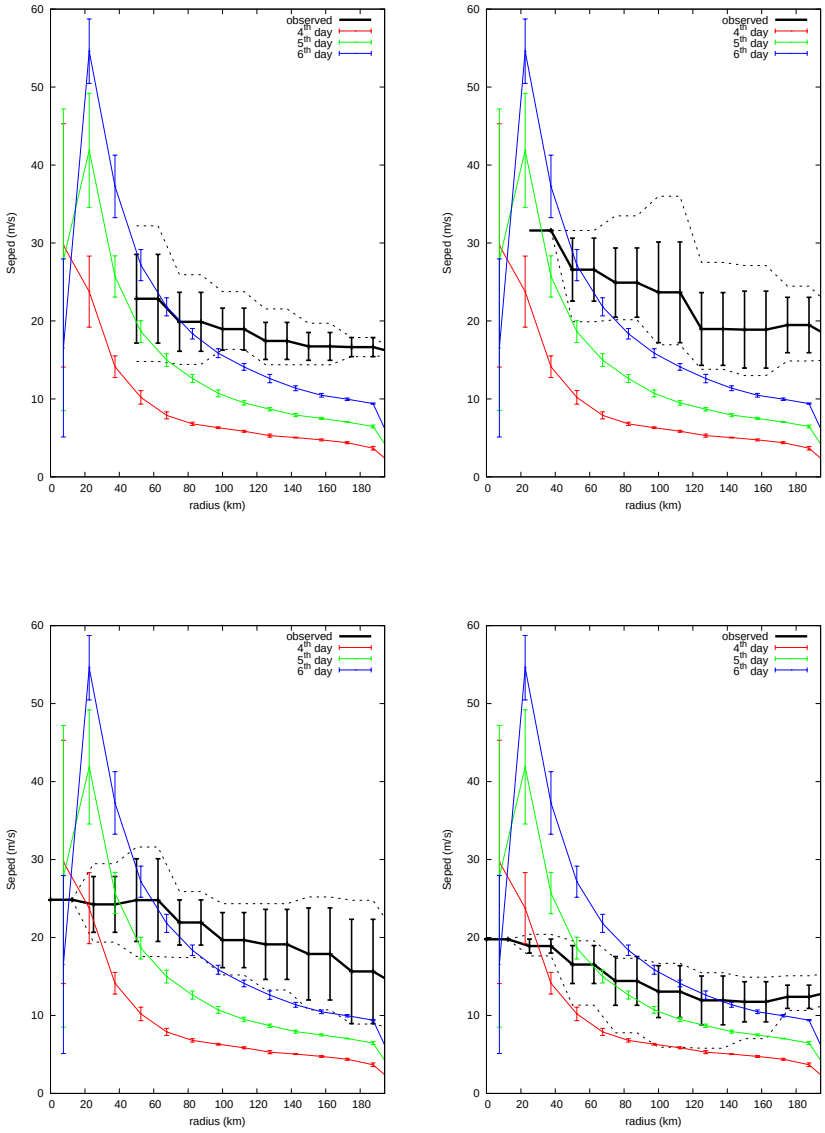

Figure 5.3.5: Comparison between radial cloud model simulated wind profile (colour lines) at different time steps (4th day, red; 5th day, green; 6th day, blue) and wind speed satellite derived measurements for 961007 case at different time steps. Each wind speed value is a radial average every 12.5 km from the centre of medicane (on 0 at x-axis, km). Mean speed values (y-axis, ms^{-1}). Solid colour error lines values correspond to simulated results at the time of initial formation of the system. Solid black error lines are satellite derived measurements. Dashed black lines above(below) corresponded with the maximum(minimal) wind speed value at the corresponding radii. Satellite measurements on 8/10/96 at 21^{00} UTC (top left), 8/10/96 at 18^{06} UTC (top right), 9/10/96 at 06^{24} UTC (bottom left) and 10/10/96 at 12^{00} UTC. In both cases, error bars are calculated as standard deviation from the values used to compute the average

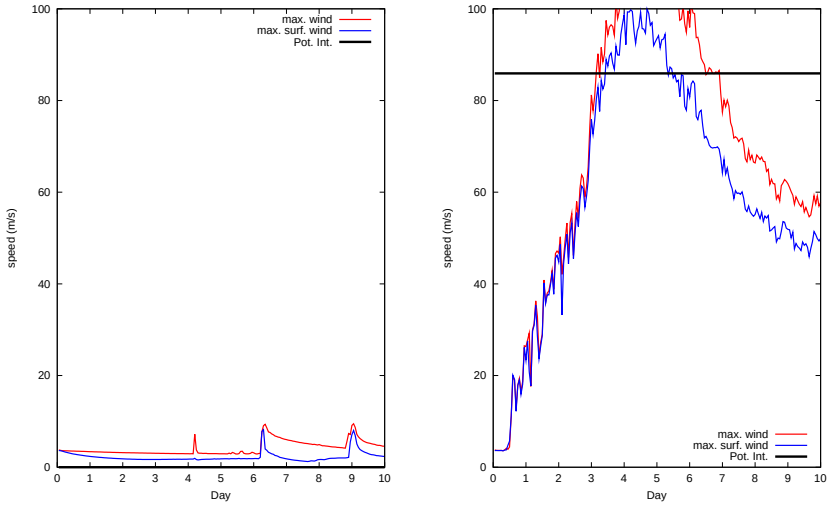

Figure 5.3.6: As in figure 5.3.4, but cooling 5 $°C$ SST (left) and increasing 5 $°C$ Sea surface Temperature (right).

to obtain a warmer initial vortex, the initial maximum azimuthal velocity is increased without changing the vortex dimensions ($r_{max} = 25\ km,\ v_{max} = 15\ ms^{-1},\ r_0 = 100\ km$). Sensitivity tests results will be shown with plots of the evolution of the maximum wind speed at all levels, maximum surface wind speed and potential intensity. Potential intensity is the theoretical maximum wind speed that can attain the steady-state storm according to the air-sea interaction theory (Bister and Emanuel, 1998).

For the sake of brevity, only the sensitivity results of the 960912 environment will be shown. The sensitivities obtained for the 960912 case are quite representative of the sensitivities obtained from the other cases. Sensitivity test simulations results (see figure 5.3.6) show a high impact of changes in the sea surface temperature. In some cases, the system is not formed when the SST has been cooled 5 $°C$ (e.g.: 960912 case). When the SST has been increased 5 $°C$ a much more intense and larger system is obtained, reaching hurricane strength (wind speeds faster than 33 ms^{-1}). On 960912 when SST has been increase 5 $°C$, potential intensity derived from the cloud model simulation is extremely high (maximum wind speeds over 100 ms^{-1}). This value would explain a high potentiality of the environment resulting from a combination of the prescribed vertical sounding and the SST. This result should not been taken as a high simulation of the specific storm, but as a mere potential test of the environment.

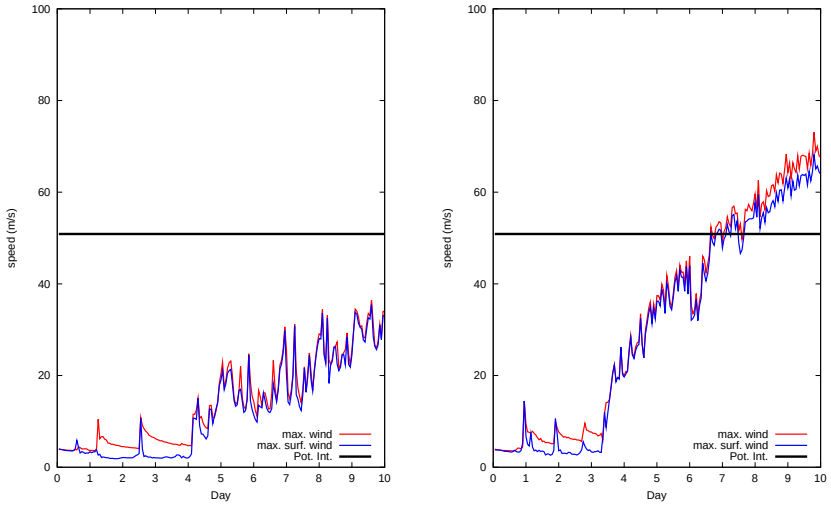

Figure 5.3.7: As in figure 5.3.4, but using a smaller initial vortex ($r_{max} = 15\ km$, $v_{max} = 5\ ms^{-1}$, $r_0 = 50\ km$, left) and with a wider initial one ($r_{max} = 25km$, $v_{max} = 5\ ms^{-1}$, $r_0 = 500\ km$, right)

5.3.1 Sensitivity on dimension of initial vortex

Changes in the dimension of the initial vortex size had a minor effect on the storm simulations (see figure 5.3.7). However, a weaker storm is obtained when the initial vortex is smaller. Besides, the storm takes more time to develop (it is assumed that development is reached when the model simulates maximum wind speeds higher than 20 ms^{-1}). With a larger initial vortex, the storm is formed a bit faster and is quite a bit stronger. On changes on the initial weak vortex, significant changes on the self organisation of the system are introduced (Rotunno and Emanuel, 1987). A weaker initial vortex is less able to organise properly convection than a stronger one.

5.3.2 Sensitivity on initial humidty

The initial relative humidity has a strong effect on the simulations (see results on figure 5.3.8). In a dryer environment, the results are not much different from the control simulation. However, a much more intense system is simulated when the humidity is increased. Moreover, the system is formed much faster than in the control simulation (2 days instead of 4 days). It is shown that high initial moisture in the atmosphere is not a necessary ingredient to generate a medicane in the environment. However, high humidity

emphasises and increases the medicane genesis.

5.3.3 Sensitivity on initial vortex strength

Finally, sensitivity tests on the core temperature of the initial vortex show a clear influence on the speed of formation of the storm (see figure 5.3.9). The simulated storm is formed much faster than in the control case. At the same time, a significantly stronger system is simulated. The environments have not been changed. However, changes on the characteristics of the initial vortex produce changes on the formation and organisation processes of the system.

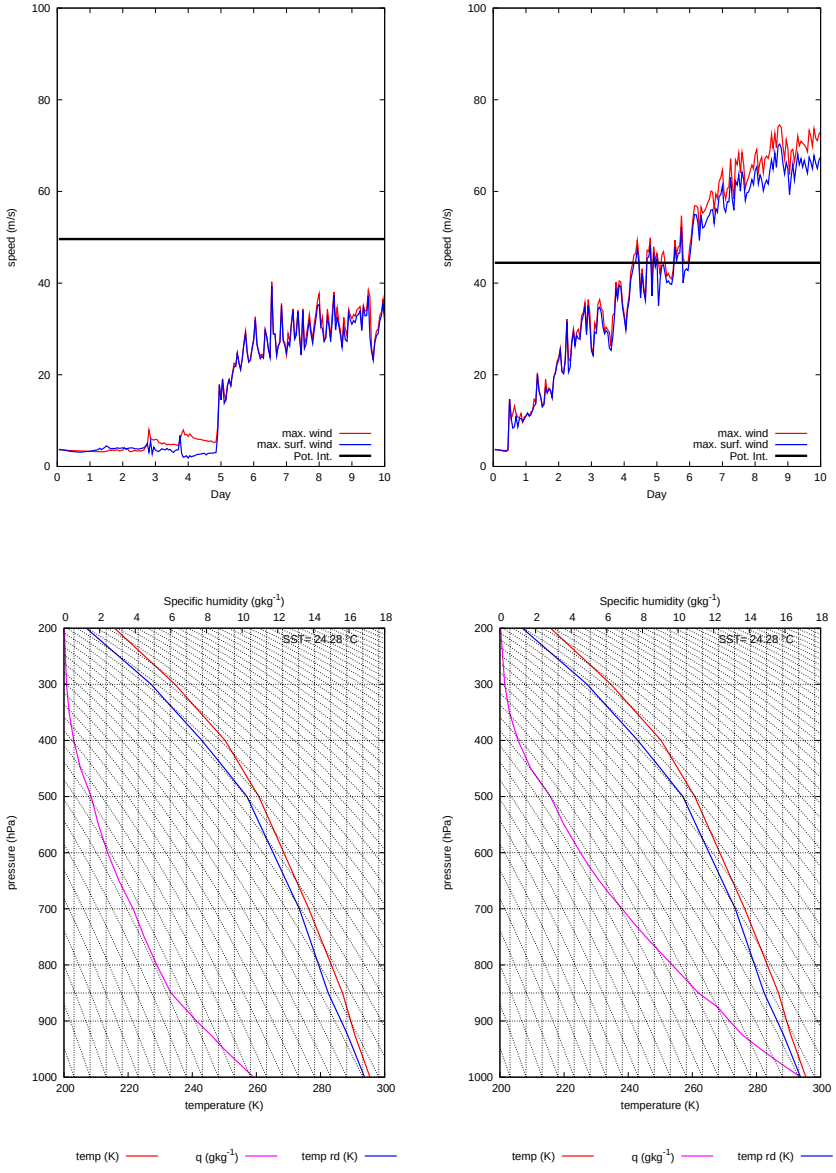

Figure 5.3.8: As in figure 5.3.4, but drying 30% (bottom left) initial vertical relative humidity profile (top left) and increasing 30% (bottom right) initial vertical relative humidity profile (top right)

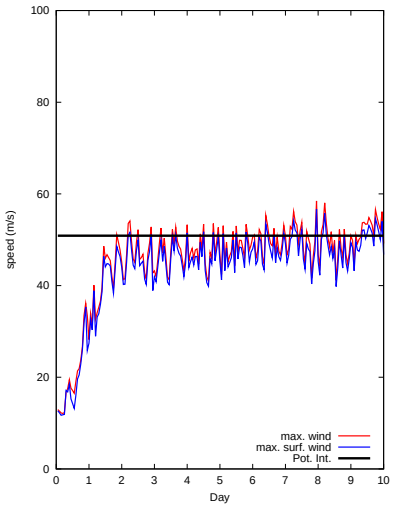

Figure 5.3.9: As in figure 5.3.4, but increasing maximum speed of initial vortex (warmer vortex, $v_{max} = 15\ ms^{-1}$)

5.4 Air-sea mechanism sensitivity study in 3 Medicanes

In order to asses the air-sea interaction in the medicane evolution, a sensitivity test of four factors: sea surface temperature (SST), latent heat flux from the sea (LHF) Upper level PV anomaly and sea surface temperature (SST) is carried out with the MM5 v3.7 numerical model (Grell et al., 1995). This sensitivity test is developed through the factor separation technique (Stein and Albert, 1993). Three different cases are studied (see figures 5.1.2, 5.1.3, 5.1.4 and 5.1.6 respectively for the January 1995, September 1996 and May 2003 cases), attempting to generate a more general scope of the sensitivities. The three selected cases attained different regions, intensities and periods of the year. Due to the large number of simulations needed to deal with the four selected factors (16) short and clear cases are selected: January 1995 south Ionic Sea case (studied previously by Lagouvardos et al., 1999; Pytharoulis et al., 2000), September 1996 Western Mediterranean case (Homar et al., 2003b) and May 2003 Western Mediterranean case.

Storm direct measurements obtained from BUFR data archived in the ECMWF, show a 'tropical storm' strength of the selected medicanes wind speeds less than 33 ms^{-1}). Like the satellite information, BUFR observations reflect the weakness of the 030527 medicane case in comparison with the strong activity of the 950116 and 960912 cases (see table 5.3.a).

5.4.1 Sensitivity methodology and control simulations

Air-sea interaction (Emanuel, 1986) has been assumed as an important mechanism in the medicane evolution. In order to study the role of the mechanism a complete sensitivity study of the medicane events to four aspects involved in it is carried out.

Surface fluxes SSHF and LHF are well correlated with the surface wind and the temperature of the sea surface (Emanuel, 1986; Schulz et al., 1996). Changes on the fluxes or/and in the SST will modify strongly the energy source of the storm. On the other hand, previous studies suggest that the thermodynamic disequilibrium necessary for the development and maintenance of Mediterranean tropical-like storm is activated by an upper level cold low (Emanuel, 2005; Fita et al., 2007a). In order to verify this hypothesis an additional sensitivity analysis to the upper level disturbance will be carried out. With the selection of these four factors, one attempts to capture the most important aspects that influence the energy budget of the air-sea interaction mechanism.

MM5 v3.7 mesoscale model will be used for the numerical determination of the sensitivities. The sensitivity study will be realised by modifying or switching off some aspects

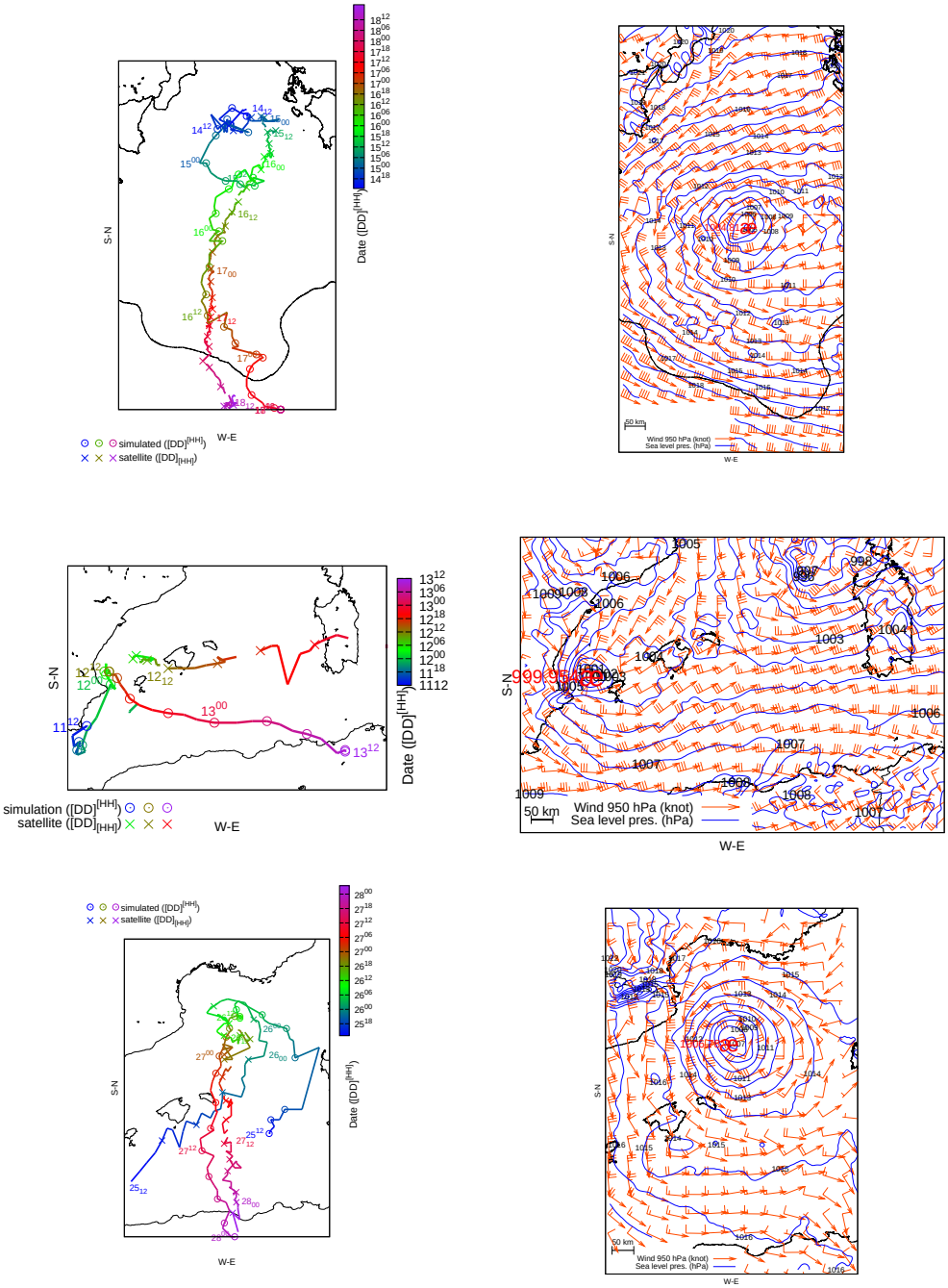

Figure 5.4.1: Left panels: MM5 simulated medicane trajectories (line with empty circles) and satellite derived medicane trajectory (line with crosses) coloured according to date. Case 950116 (top), 960912 (middle) and 030527 (bottom). Right panels: Sea level pressure (blue line, every 1 hPa), and horizontal wind at 950 hPa (barbs notation: triangle: 50 knot; pennant: 10 knot; half pennant: 5 knot) on Jan. 16th 1995 at 00 UTC (top), September 12th at 15 UTC (middle, medicane is the the small vortex in front of the Eastern Iberian Peninsula coast) and May 27th 2003 at 00 UTC (bottom). æ symbol is proposed as medicane indication (keeping § for hurricane)

of the numerical model or the environmental conditions of the simulations. ECMWF analyses and BUFR observation files (WMO, 2007) have been used for the initial and boundary conditions of the simulations. Two-way nested domains of varying dimensions and 15 and 5 km horizontal resolutions with 23 vertical levels are applied on the regions of the three studied medicanes. The cloud microphysical scheme of graupel(Reisner2) (Reisner et al., 1998) has been selected. Kain-Fritsch (Kain and Fritsch, 1993; Kain, 2004) cumulus scheme has been only activated in the first domain. Thus convection will be explicitly simulated by the primitive equations of the MM5 model in the second domain. It is assumed that 5 km horizontal resolution is high enough as to enable this procedure. A simple Blackadar scheme (Blackadar, 1979; Zhang and Anthes, 1982) is used to model the planetary boundary layer (PBL) processes. Cloud Radiation scheme is used (Dudhia, 1989). See MM5 reference for information and characteristics of each selected scheme (Grell et al., 1995). From each cyclone the simulated fields every 3 hours for the 15 km resolution domain (domain 1), and every hour for the 5 km resolution domain (domain 2) will be obtained. January 1995 case from Jan. 14th at 06 UTC to Jan. 18th at 00 UTC will be simulated; September 1996 case from Sep. 11th at 12 UTC to Sept. 13th at 12 UTC and May 2003 case from May 25th at 12 UTC to May 28th at 00 UTC. However, results during the most important phase of the storms and for the periods during which set of simulations present a vortex structure with similarities to the studied cases will only be shown.

Control simulations (i.e. those simulations with the full physics and environmental characteristics) of each case (outputs in figure 5.4.1) reveal the genesis of a small strong vortex assumed to represent a tropical-like storm. However, simulated trajectories show a temporal and spatial shift with respect to the observed ones on the satellite images. Genesis zones are significantly away from the observed areas (except for the January 1995 case) and the simulated vortexes start earlier. Nevertheless, all control simulations are able to simulate a tropical-like storm (denoted by the warm core of strong and small vortex, see figures 5.4.1, 5.4.2 and 5.4.3). There is a strong difference between the trajectory of the September 1996 medicane simulated in this study and in Homar et al. (2003b). In that study NCEP analyses as boundary conditions and MM5 v3.3 version model were used. These simulations will be assumed good enough for the purposes of the subsequent sensitivity study.

Azimuthal and time averaged vertical-cross sections of the simulated mature storms reflect the characteristic structure of a tropical cyclone (figures 5.4.2 and 5.4.3). This averaged state of the storm shows a wall structure in the relative humidity and wind speed fields (at about 20 km from the centre for the 950116 case). Besides, a free cloud eye is reflected according to the simulated vertical motion since subsidence is present in the core of the storm. For September 1996 and May 2003 cases, MM5 does not simulate a structure as clear as in January 1995 case (see figure 5.4.3).

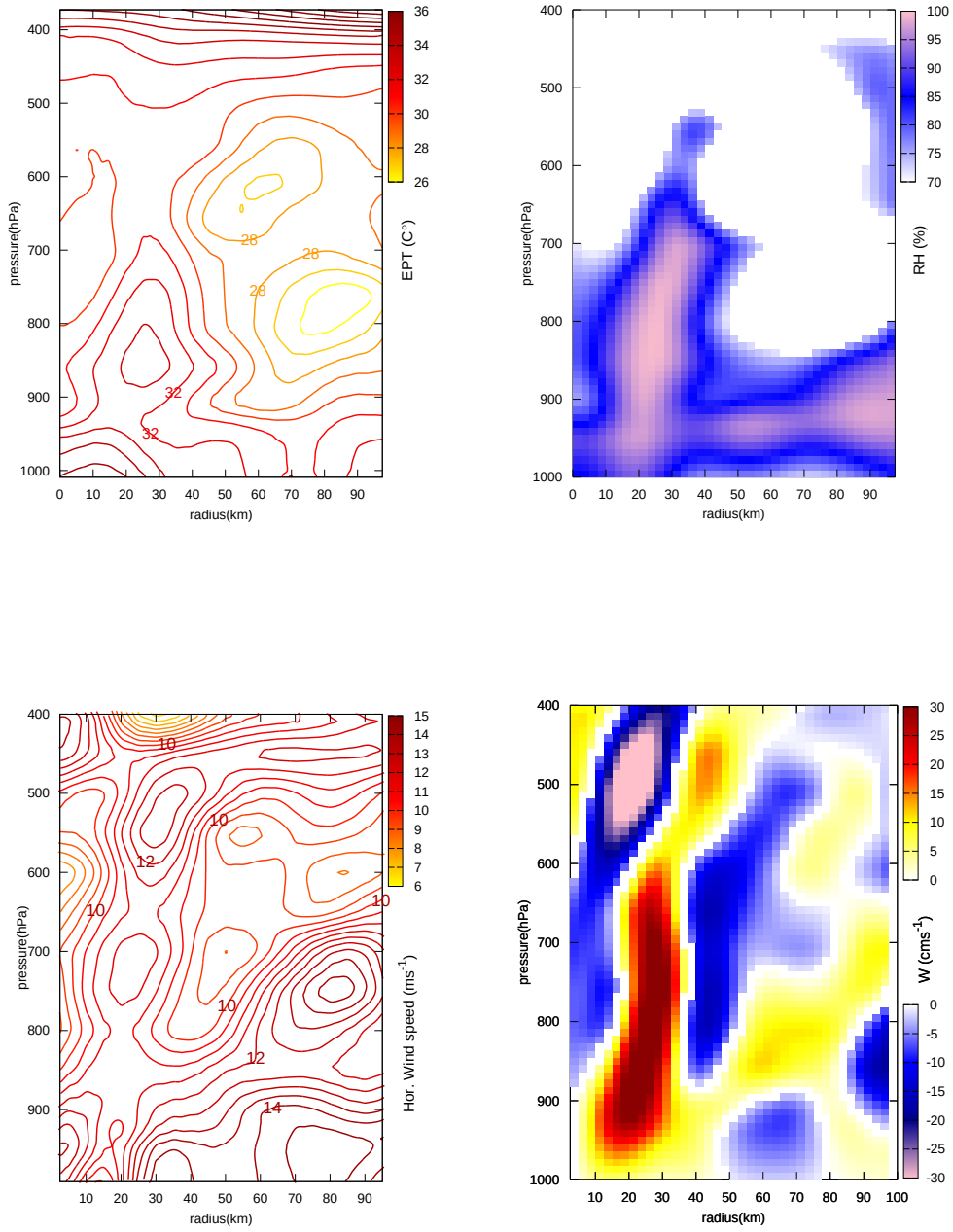

Figure 5.4.2: Vertical cross-section from the centre of the storm, showing the time-azimuthal averaged fields of MM5 simulated 950116 medicane during the period of maximum intensity (from 15th Jan. 95 at 16 UTC to 16th Jan. 95 at 05 UTC). x-axis (radial distance from the centre of the storm, km), y-axis (pressure, hPa). Top left panel: Equivalent Potential Temperature (every 1. $°C$). Top right panel: Relative Humidity from 70 % (shaded). Bottom left panel: Horizontal velocity (lines every 0.5 ms^{-1}). Bottom right panel: Vertical velocity (cms^{-1}, shaded)

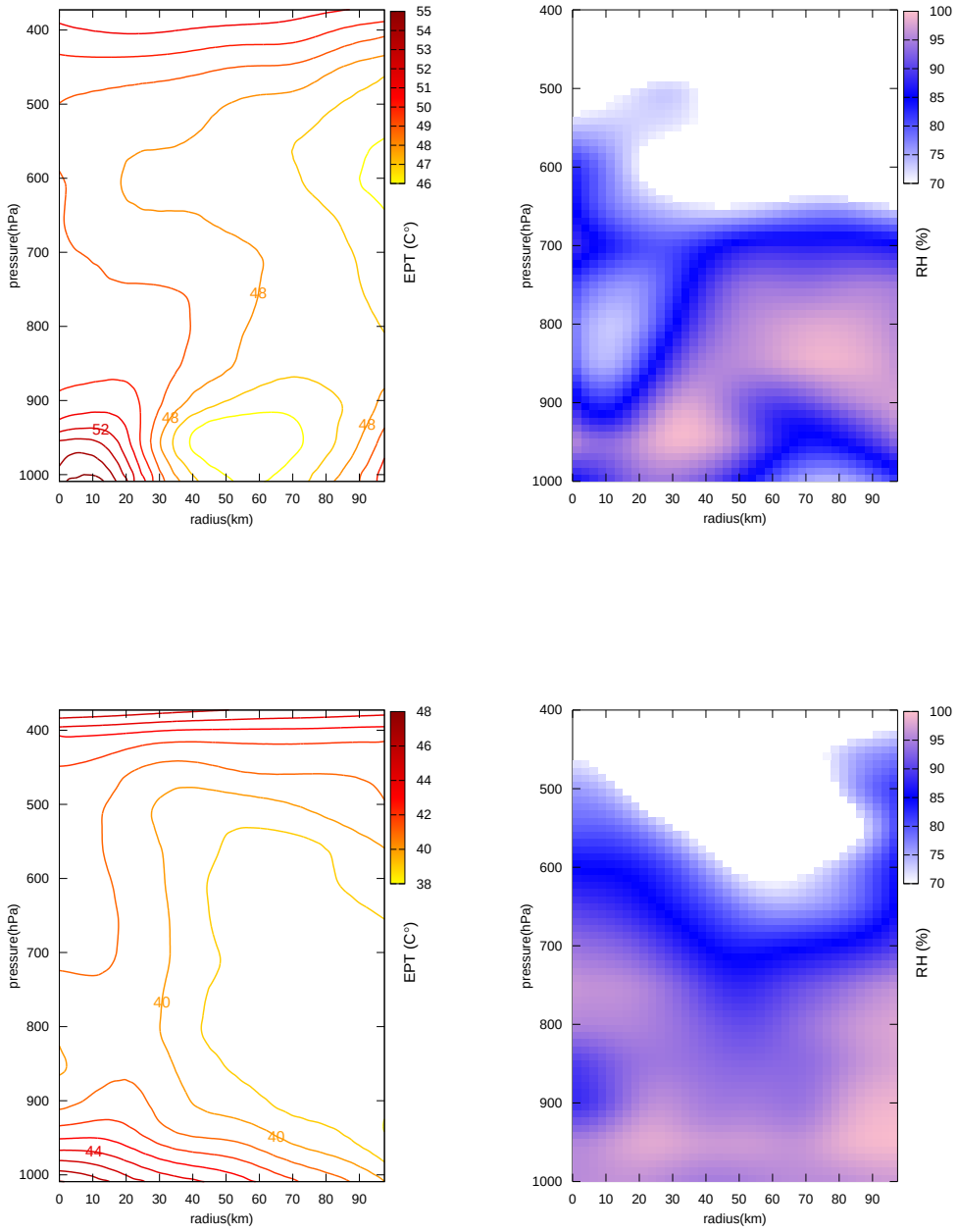

Figure 5.4.3: As in figure 5.4.2, but for 960912 medicane (top) during the period of maximum intensity (from 12th Sept. 96 at 07 UTC to 12th Sept. 96 at 17 UTC) and 030527 medicane (bottom, from 26th May 03 at 11 UTC to 26th May 03 at 20 UTC). Left panels: Equivalent Potential Temperature (every 1. $^{\circ}C$). Right panels: Relative Humidity from 70 % (shaded)

For the sensitivities studies on the latent and sensible surface fluxes will be switched off in the numerical computation of the PBL for all the grid points (LHF is only switched off in grid points located above the sea). The effects of Sea surface temperature will be studied by means of simulations where SST has been decreased $5°C$ from its original value obtained from the ECMWF analyses. Upper level disturbance effects will be studied through the PV Inversion technique. Usually, PV Inversion technique is used to modify the initial conditions of the numerical simulations in order to find sensitivities to these changes (Huo et al., 1999; Romero, 2001). Due to the small dimensions of the selected biggest domain, however, upper level disturbances are not fully captured at the first time step of the simulations. Therefore, the PV Inversion technique is used to modify the upper level characteristics at all the boundary condition times over the ECMWF analyses. Potential Vorticity anomaly field is computed at each ECMWF analyses time (00, 06, 12 and 18 UTC) during the period of MM5 simulations. The inversion of the positive PV anomaly enclosed between 500 hPa and 100 hPa 150 km (10 grid point) away from the border of the first domain is done. Then a subtraction of the 10% of the inverted fields obtained from these selected PV anomalies will be applied to generate the modified boundary conditions at each time step. Thus, the net effect is referred to a slightly weaken the intensity of the upper-level troughs or cut-off lows initially located of later incoming into the simulated domain.

The factor separation (FS) technique (Stein and Albert, 1993) is used to study the effects of the selected factors (1) LHF, (2) SSHF, (3) Upper level PV and (4) SST on a forecast field f. According to this technique, 16 different simulations are necessary to isolated the full collection of individual and synergistic effects due to these four factors (see table 5.4.a). The effect on a forecasted field of individual factors and their synergies is explained in section 2.3

It is very difficult to find a plausible physical meaning of quadruple and even triple synergies due to the complexity of the dynamics of the problem. Therefore, results will be discussed up to the triple synergies only. However, e_{1234} results will be also given, but not interpreted.

Medicanes are the result of both baroclinic development (precursor environment) and the air-sea interaction (genesis and maintenance mechanism). This study focuses on the later dynamical process. Thus, FS on the simulated medicane it self (identified in the simulations as a minimum sea level pressure zone of high vorticity, with circular morphology and small dimensions) will be focused. Numerically simulated fields will be examined around the centre of small vortex. These medicane centred fields will be used in equation 2.3.4 to compute the effect of the 4 factors through the FS technique. Thus, a Lagrangian application of the FS technique will be done in contrast to a previous study which applied

Table 5.4.a: Description of the factors that are included (1) in each effect. LHF factor means a boundary layer without latent heat flux from the sea. SSHF factor means a boundary layer without sensible surface heat flux. ULPV factor means a decrease of 10% of the upper level PV. SST factor means a Sea surfer temperature 5°C colder

effect	**LHF**	**SSHF**	**ULPV**	**SST**
e_0	0	0	0	0
e_1	1	0	0	0
e_2	0	1	0	0
e_3	0	0	1	0
e_4	0	0	0	1
e_{12}	1	1	0	0
e_{13}	1	0	1	0
e_{14}	1	0	0	1
e_{23}	0	1	1	0
e_{24}	0	1	0	1
e_{34}	0	0	1	1
e_{123}	1	1	1	0
e_{124}	1	1	0	1
e_{134}	1	0	1	1
e_{234}	0	1	1	1
e_{1234}	1	1	1	1

FS following the trajectory given by the 'control' simulation of the medicane Homar et al. (2003b). FS defines the effects on a forecast field due to a linear decomposition of the roles of each factor. A Lagrangian use of the FS can be done if it is considered the system it self as a result of the linear combinations of the different systems simulated by each set of factors.

The effects computed according to each methodology differ significantly (see an example in figures 5.4.4 to 5.4.6). However, from a general point of view, effects in both methodologies seem to preserve in some how the sign of their role and even their dual phase dynamics.

The study is focused in three scalar forecasted fields: sea level pressure value at the centre of the storm (Sea lev. pres.), relative vorticity (RVOR) at the centre of the storm at 950 hPa and maximum azimuthally averaged horizontal wind at 950 hPa ($HWind_{max}$, within a radii of 200 km from the centre of the storm). A relation exists between the pressure value at the centre of the storm and the maximum horizontal wind speed (Emanuel, 1986). A cyclogenetic or enhancing role of the air-sea interaction effects will be related to a decrease of the central pressure value of the system and increase of the horizontal wind speed and relative vorticity at the centre.

5.4.2 Sensitivity results

Results of the sensitivity tests will be in three different ways: storm trajectories obtained by each simulation, temporal evolution of the individual and synergistic effects on the three variables. Positive(negative) values for these effects indicate that the corresponding factor increases(decreases) the analysed storm attribute.

Simulated storm trajectories shown similar characteristics in all medicanes (see figure 5.4.7). Trajectories of medicanes are significantly modified with respect to the control one when the upper level trough is altered (simulations without factor 3). Changes in the upper level structure of the trough play two main roles: altered the vertical disequilibrium between upper air and lower-level air and radiative cooling at outer and upper-level parts of the energetic cycle of the air-sea interaction. On the January 1995 case the trajectory of the medicane in the simulation where the upper level disturbance has been modified (f_{124}) is very different to the rest (see top panel left in figure 5.4.7), but without strong differences with respect to the central pressure values (see figure 5.4.8).

Simulated trajectories of the medicanes do not show a clear relation with respect to the trajectories of the upper level maximum vorticity centres (see figure 5.4.9). However, a momentaneous strong influence in the trajectory of the medicane can be observed when upper level vorticity centres are significantly close in space and time to the position of

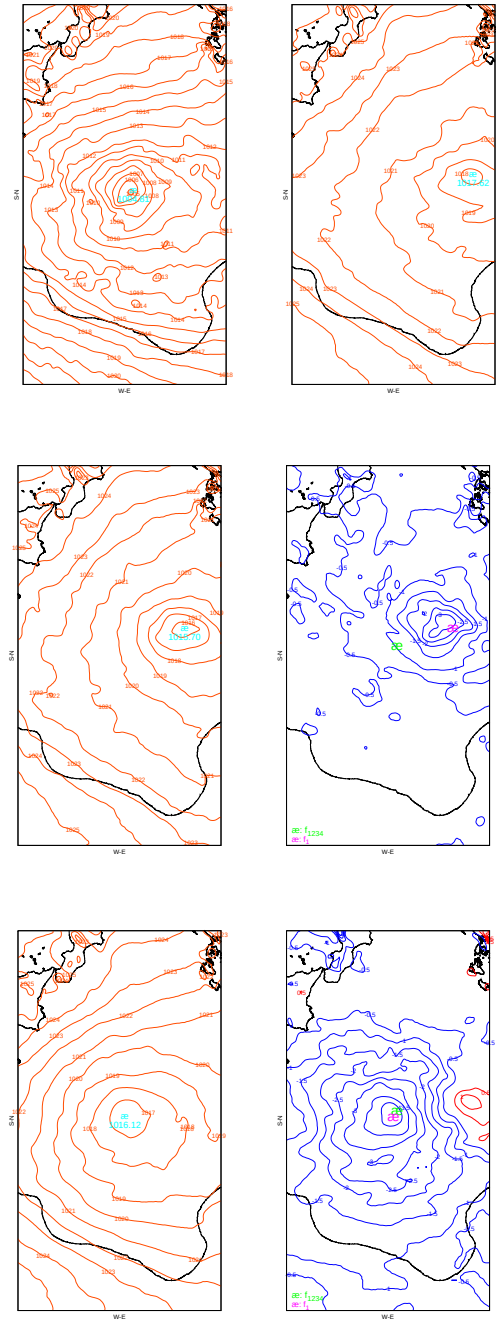

$$f_i^{cont} = f_i(x_{cont}, y_{cont})$$
$$f_i^{lagr} = f_i(x_i, y_i)$$

$f_0^{cont} = 1019.72$ hPa
$f_1^{cont} = 1020.40$ hPa
$f_2^{cont} = 1016.18$ hPa
$f_3^{cont} = 1019.25$ hPa
$f_4^{cont} = 1020.57$ hPa
$f_{1234}^{cont} = 1005.81$ hPa

$e_1^{cont} = -0.85$ hPa
$e_1^{lagr} = -1.92$ hPa

$e_3^{cont} = -4.39$ hPa
$e_3^{lagr} = -1.5$ hPa

Figure 5.4.4: Simulated sea level pressure (every 1 hPa, orange lines) on January 16th at 00 UTC; position and sea level pressure at the centre of the medicane (æ in hPa, light blue). Control simulation (f_{1234}, top left), background (f_0, top right), LHF (f_1, middle 1st), ULd (f_3, bottom 1st). 2-dimensional effect on sea level pressure (every 0.5 hPa; blue lines negative; red positive) and medicane position according to the control simulation (æ green) simulation only with the factor i (æ pink) on January 16th at 00 UTC for the LHF (e_1, middle 2nd), ULd (e_3, bottom 2nd). Effects values following control simulation (Eulerian form; $e_i^{cont} = f_i^{cont} - f_0^{cont}$), according to the position of each medicane (Lagrangian form, $e_i^{lagr} = f_i^{lagr} - f_0^{lagr}$)

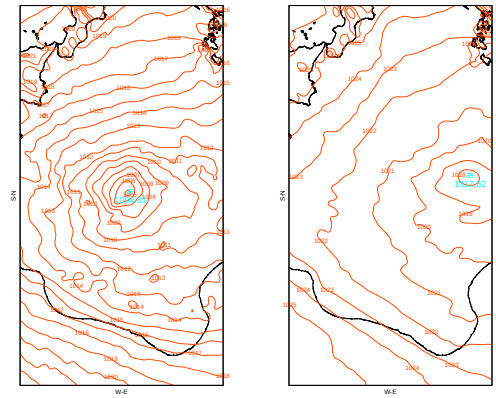

$$f_i^{cont} = f_i(x_{cont}, y_{cont})$$
$$f_i^{lagr} = f_i(x_i, y_i)$$

$$f_0^{lagr} = 1015.70 \text{ hPa}$$
$$f_1^{lagr} = 1016.69 \text{ hPa}$$
$$f_2^{lagr} = 1016.12 \text{ hPa}$$
$$f_3^{lagr} = 1016.75 \text{ hPa}$$
$$f_4^{lagr} = 1017.62 \text{ hPa}$$
$$f_{1234}^{lagr} = 1004.81 \text{ hPa}$$

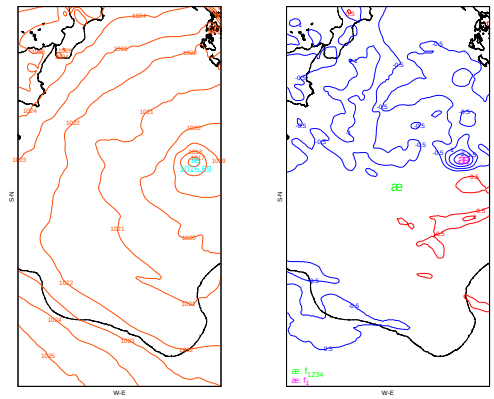

$$e_2^{cont} = -0.17 \text{ hPa}$$
$$e_2^{lagr} = -0.93 \text{ hPa}$$

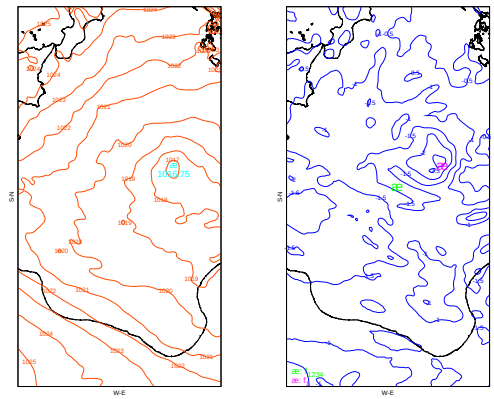

$$e_4^{cont} = -1.32 \text{ hPa}$$
$$e_4^{lagr} = -0.87 \text{ hPa}$$

Figure 5.4.5: As in figure 5.4.4, but for SSHF (f_2, middle 1st), SST (f_4, bottom 1st). SSHF (e_2, middle 2nd), SST (e_4, bottom 2nd)

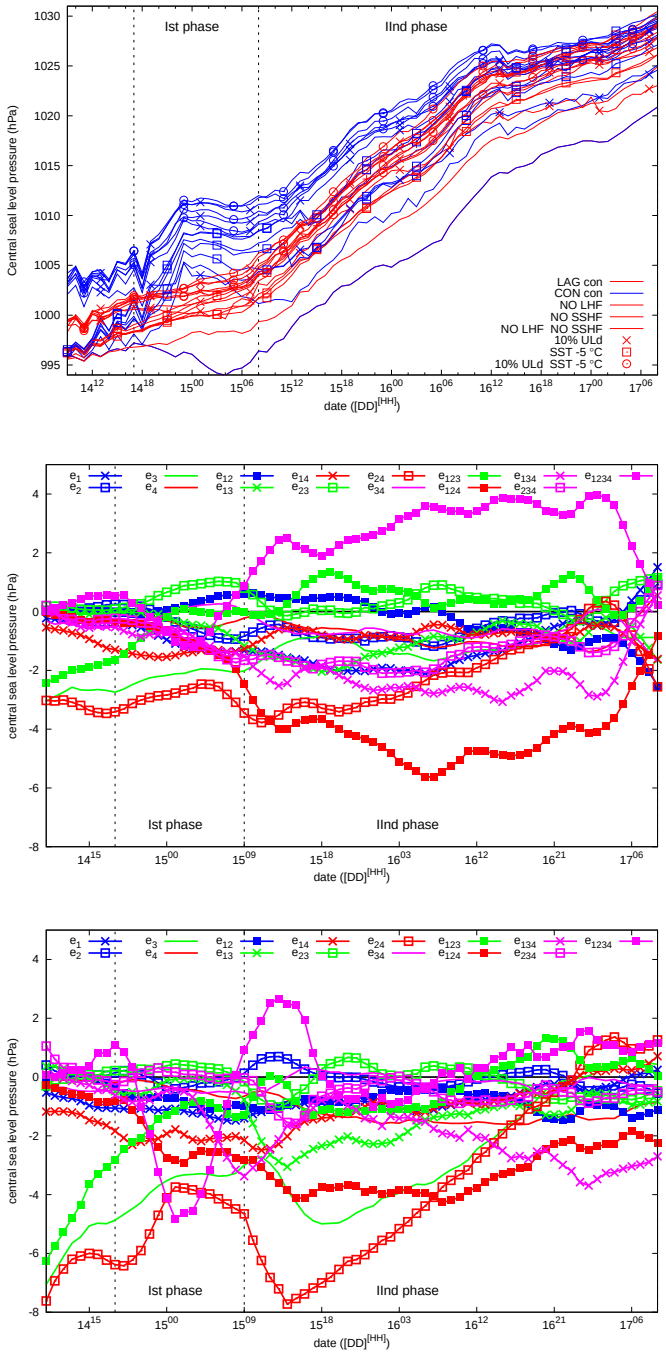

Figure 5.4.6: Top panel: Temporal evolution of the pressure at the centre of the simulated medicane (red lines) and following trajectory of the medicane of the control simulation (blue lines); solid lines without surface fluxes (f_{1234}, f_{234}, f_{134}, f_{34}), lines with crosses with -10% ULd (f_{124}, f_{24}, f_{14}, f_4), with a SST 5° colder (f_{123}, f_{23}, f_{13}, f_3), with -10% ULd and SST -5° (f_{12}, f_2, f_1, f_0). Effects on central sea level pressure on control simulation (middle), central pressure of each simulated medicanes (Lagrangian, bottom)

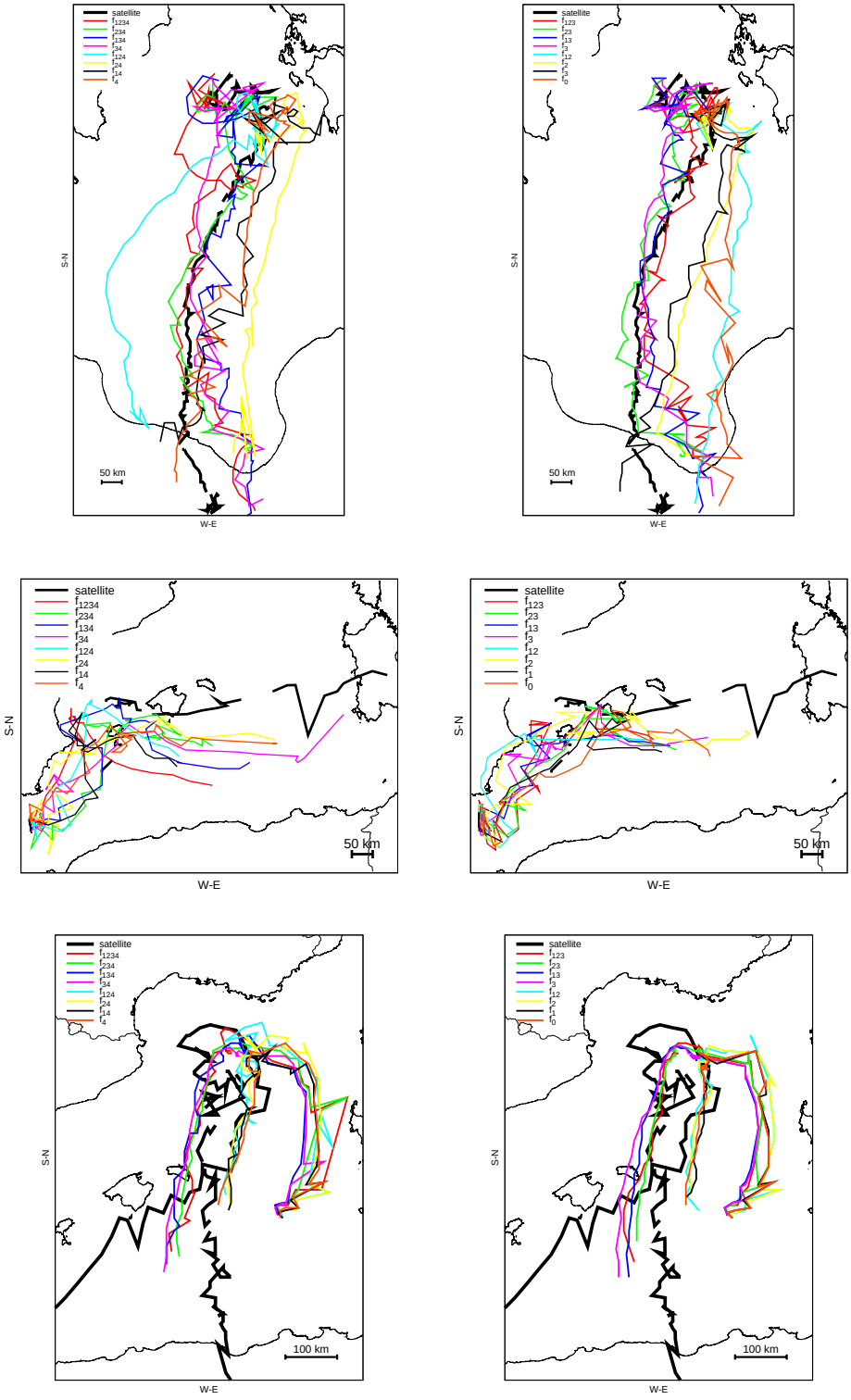

Figure 5.4.7: Simulated trajectories for each simulation. See legend for notation of the lines. January 1995 case (top), September 1996 (middle) and May 2003 case (bottom). Strong differenced blue-light line in 1995 case (top left) is the simulated trajectory of f_{124} experiment

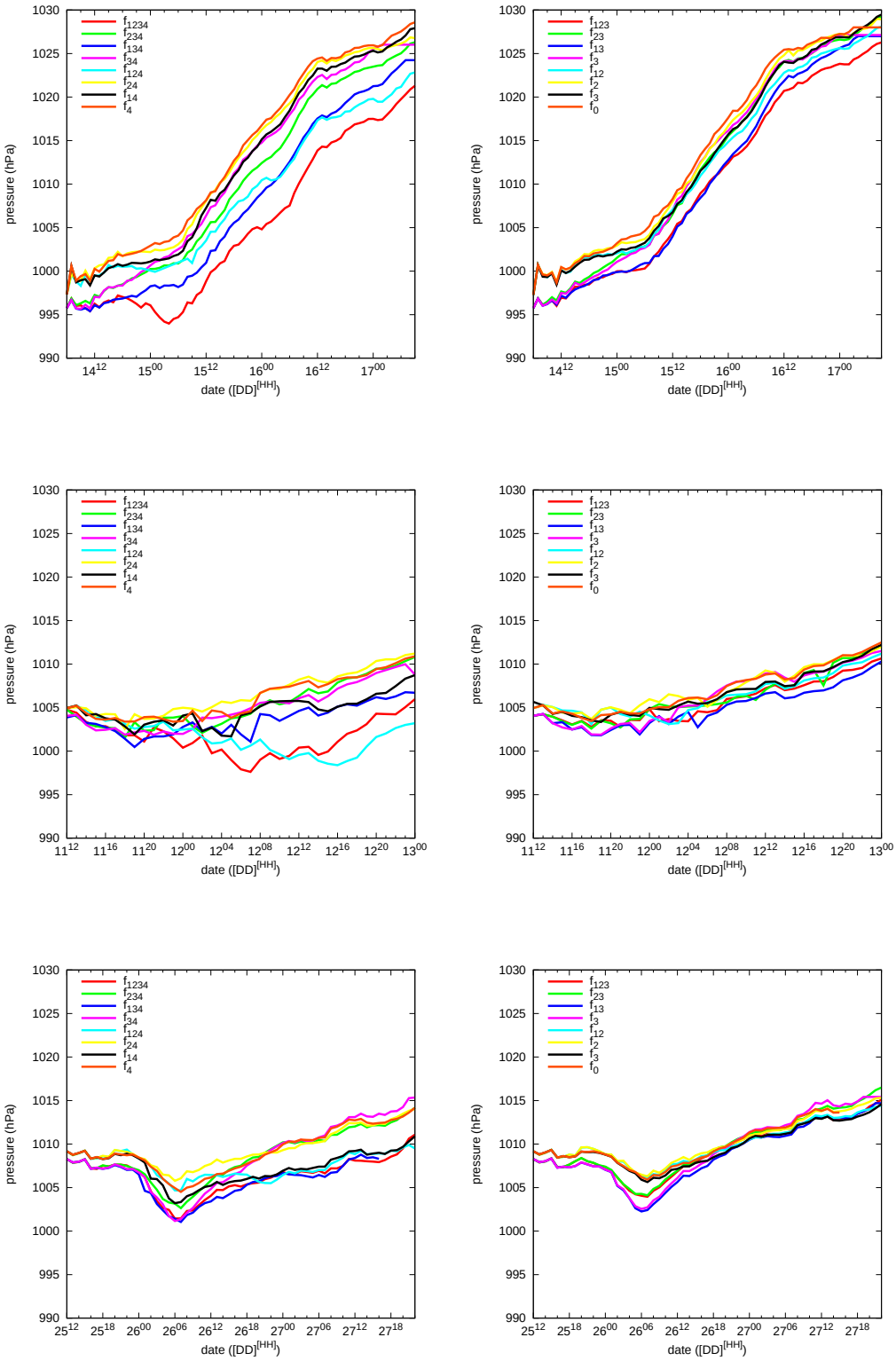

Figure 5.4.8: As in figure 5.4.7 but for the simulated sea level pressure at the centre of the medicane

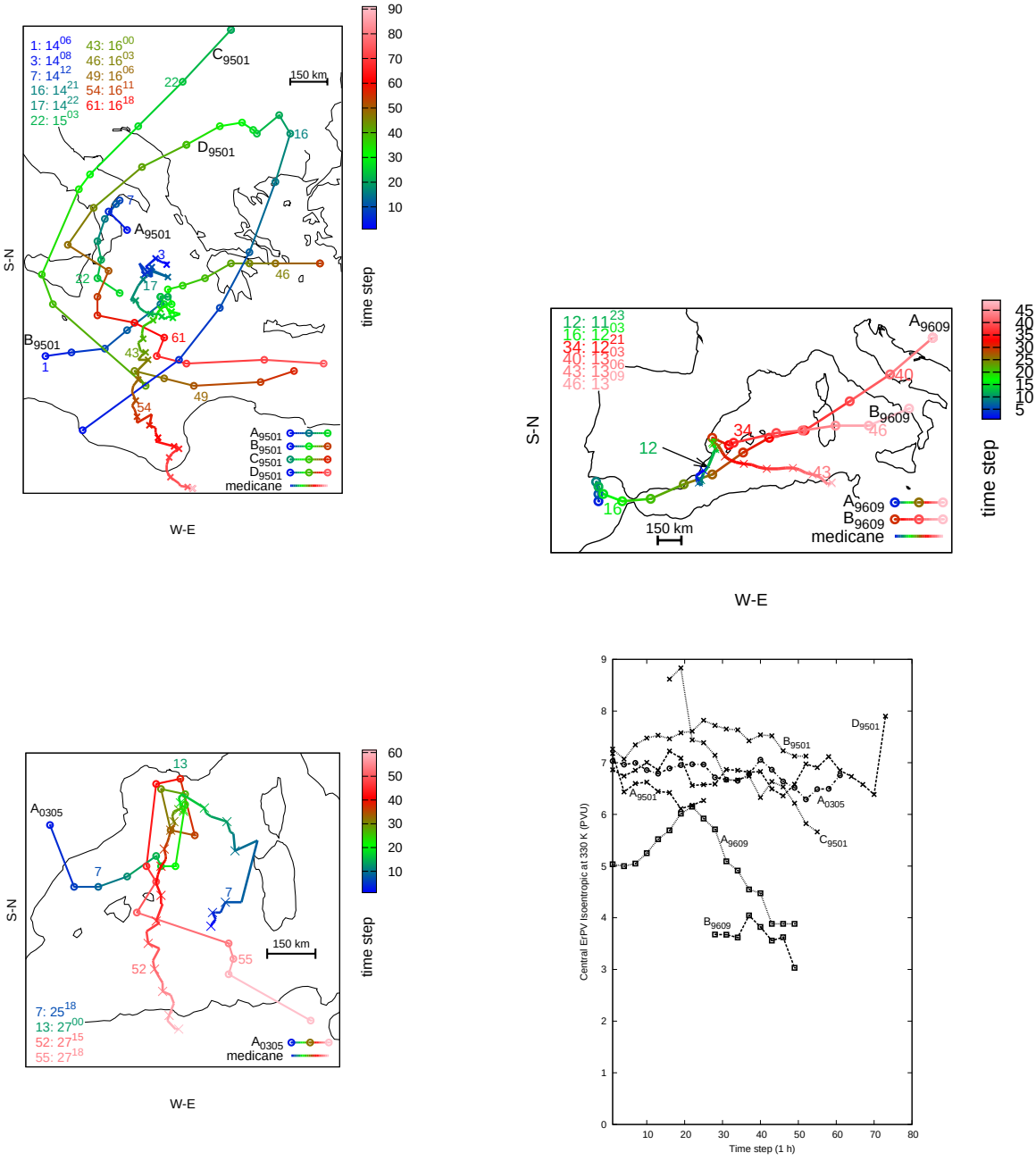

Figure 5.4.9: Trajectories of different Ertel PV maximum centres (coloured lines with circles, at 330 K isentropic surface, labelled as Ξ_{case}) related with the medicane evolution (coloured line with crosses) each circle/cross denotes 3h time-step. Colour lines changes with time step according to colour bar. January 1995 case (top left), September 1996 case (top right) and May 2003 case (bottom left). Date of position of each disturbance is indicated at different time-steps (see dates of time-steps at each graph in $[DD]^{[HH]}$ format). Ertel PV values evolution of each centre (bottom right, $PVU = 10^{-6} m^2 K s^{-1} kg^{-1}$)

the medicane. Some momentaneous similarities might be a reflect of a short-lasted coupling between upper and low-level disturbances (Hoskins et al., 1985; Bleck, 1990) not maintained due to a slower movement of the medicane with respect to the movement of upper-level disturbance assumed to be as a consequence of friction surface phenomena. On January 1995 case (top left panel in figure 5.4.9), initial movement of the medicane follows (shifted about 200 km below) similar trajectory as the A_{9501} maximum. Movement loop on the medicane trajectory occurs with a temporal and spatial coincidence with upper level maximum B_{9501}. South-southeast-ward movement of the medicane seems to be influenced also by the similar tendency of the upper-level maximum centres and the flow pattern attributed to an elongated N-S upper level disturbance.

In the September 1996 case, at the same moment that upper level maximum overpasses the zone where the medicane is located, storm system starts an eastward movement similar to the upper level maximum centres (top right panel in figure 5.4.9). Initial phases of the movement of the May 2003 medicane are dominated by the flow derived by the upper level disturbance (see bottom left panel in figure 5.4.9). Medicane and upper level maximum centre trajectories are temporal and spatial coincidence for a period of time in which upper level maximum centre draws a loop and medicane keeps almost fixed. Once upper level maximum moves southward, medicane also starts to move southwardly.

The temporal evolution of the Ertel PV maximum centres on an isentropic surface (330 K) show that there is a small non-conservative evolution of the Ertel PV. The change of PV values on isentropic surfaces is related to diabatic processes such as deep convection (Hoskins et al., 1985). This is illustrated in the azimuthal averaged radiative tendency and PV values (figure 5.4.10), showing a relation between positive radiative warming and PV positive values at low levels.

Simulated trajectories show also a strong dependency on SST. Almost all these simulated trajectories are clearly different from the other when SST is cooled (simulations containing factor 4 $f_{\chi 4}$).

As has been said (see chapter 2) FS results present a great dependency on the number of factors. That ambiguity in the results can be treated in two different ways: applying the fractional approach of the FS technique (Krichak and Alpert, 2002), and/or studying the response of the pure effects to a change in the number of factors that are used in the FS (Alpert et al., 1995).

Another aspect that could be controlled is the degree of modification introduced when one factor is studied. Intercomparison between results could be improve if in some manner one could equalise the degree of modification of each factor to a same common value. By this way, the resulting effects can be unambiguously associated to a true sensitivity,

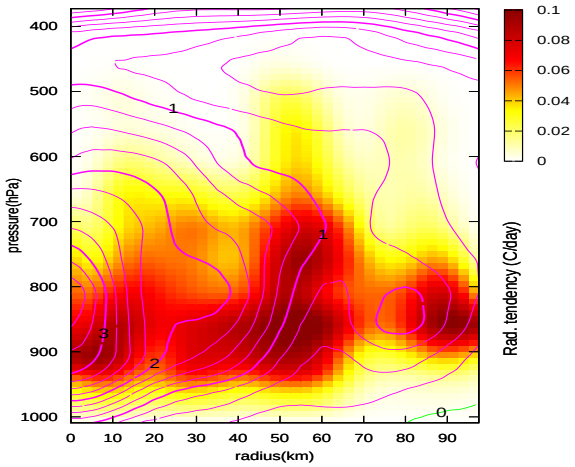

Figure 5.4.10: As in figure 5.4.2, but for the radiative tendency ($°C/day$, shaded) and PV values (PVU, lines)

avoiding the dependency into the strength and morphology of the introduced change (a similar procedure can be found in (Fita et al., 2007b)). In this sensitivity study this has not been considered, due to the difficulty to establish a correct manner to find a same common value. LHF and SSHF are completely removed from the simulations, SST is cooled 5°C and Upper level PV is only modified a 10% of its strength. Each factor have a different impact in the simulations: LHF, SSHF change the dynamics of the atmosphere. Upper level changes affect energy of the whole atmosphere, meanwhile SST modifies the energy content of the Sea.

Due to the limitation in the computational resources, the study on the response of the effects is only done through the modification of the group of selected factors.

5.4.3 Collection dependence

The dependence on the collection of factors of the three fields shows significant differences (see figure 5.4.11). The central sea level pressure of the storm presents more proportionality to the number of factors than the other two fields. The more complex response of the azimuthally-averaged wind speed and relative vorticity may be due to the fact that these fields have been derived from the model prognostic state variables. It is shown how

the non proportionality to the number of factors of some effects is reproduced in the three variables (like in e_{13} in January 1995 and September 1996 cases and e_{12} for May 2005). At the same time, no clear correspondence among effects of Sea lev. press and $HWind_{max}$ are obtained (theoretically development of air-sea mechanism establishes a relation between both variables).

The role of the effects varies among the three cases. All the storms show the strongest sensitivity to the LHF (collection $\{1\}$) and the SST (collection $\{4\}$). Almost all the effects are cyclogenetic, except SSHF in the May case (collection $\{2\}$, top left panel in figure 5.4.14). January 1995 case shows a more linear response than May 2003 case, and this linearity is very poor in the 960912 case. This result could be a reflection of the different characteristics of the storms. January 1995 would be a more similar to a prototype tropical-like storm, May 2003 case more baroclinic-like and September 1996 somewhat within. The four selected factors are shown to be more appropriate to study the January 1995, and September 1996 cases rather than May 2003 case. Such inadequate selection of factors is well observed on the collection sensitivity for the SSHF effect when looking the value of the sea level pressure at the centre of the storm for the 030527 case (top right on figure 5.4.14).

These poor results obtained in the May 2003 case for this effect (large differences and not correlated sensitivities) could also be explained by the interaction with other factors not considered in the study, such as: mixing of the thermal surface gradient due to boundary layer turbulence, diurnal cycle effects (day/night activation/suppression of the turbulence with a maximum at the end of the day, explain a phase of the effect about 18 h is in $\{2\}$ computation of e_2). On a study of an Atlas lee cyclogenetic phase of a cyclone, an afternoon increasing role of SSHF factor was also obtained (Horvath et al., 2006). Besides, the low spread obtained for the Upper level effect (e_3, bottom left panel of figure 5.4.14) might reflect the relevance of this factor in the case.

Similar high group-dependence is obtained for the Upper level PV effect (e_3) of the 960912 case. The non linearity with respect to the number of taken factors is observed and the effect-dependence does not exhibit similar trends or relation between groups (bottom left panel in figure 5.4.13). This wide behaviour could be attributed to the proximity of the Iberian peninsula and the Balearic Islands during the evolution of the case. Orography interactions of a hurricane has been related to its weakening (Bender et al., 1987). Bear in mind that latent heat release of convection (LHR) is a key parameter for the the storm (Homar et al., 2003b) and it has not been considered. The role of this not considered or hidden factor is reflected in the strong non proportionality for the Upper level PV effect to the number of factors. At the same time, almost all the groups with this factor on the other pure effects group-dependence curves have the largest differences with respect to the other ones (see in figure 5.4.13, curves $\{1,3\},\{2,3\},\{3\},\{3,4\}$). This result reflect

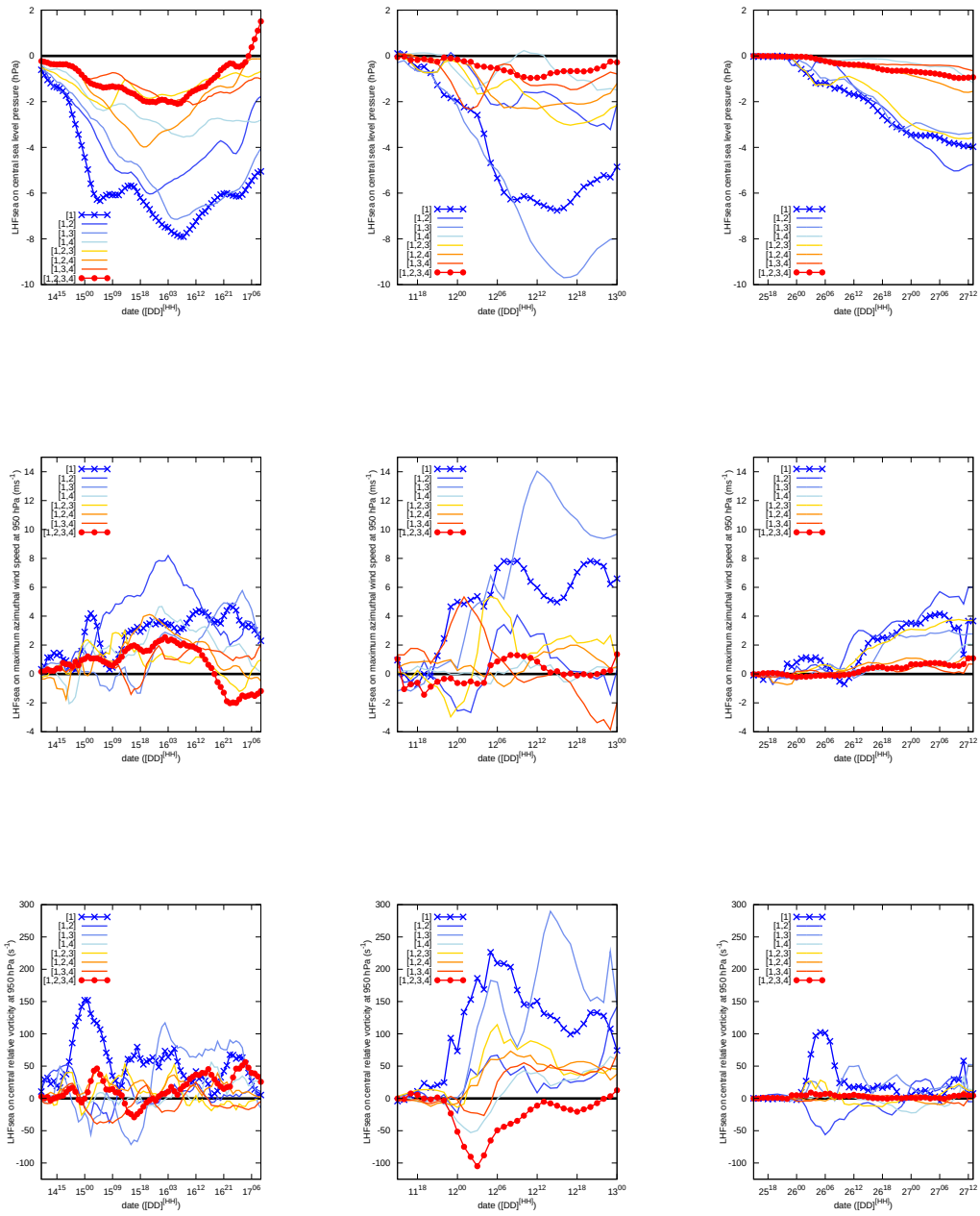

Figure 5.4.11: Collection-dependence of the LHF effect on the sea level pressure at the centre of the storm (top), the maximum azimuthal averaged horizontal wind speed at 950 hPa (middle), and the central relative vorticity at 950 hPa (bottom), for the 950116 case (left), 960912 case (middle) and the 030527 case (right). Results have been filtered with a mobile average filter of five time steps. $\{1\}$ FS effectivity of LHF (e_1) for factor 1; $\{i, j\}$ FS e_1 for two factors i, j; $\{i, j, k\}$ FS e_1 for three factors i, j, k and $\{1, 2, 3, 4\}$ FS e_1 for four factors. Factor 1: LHF, 2: SSHF, 3: Upper level PV, 4: SST. See legend for correspondences with lines

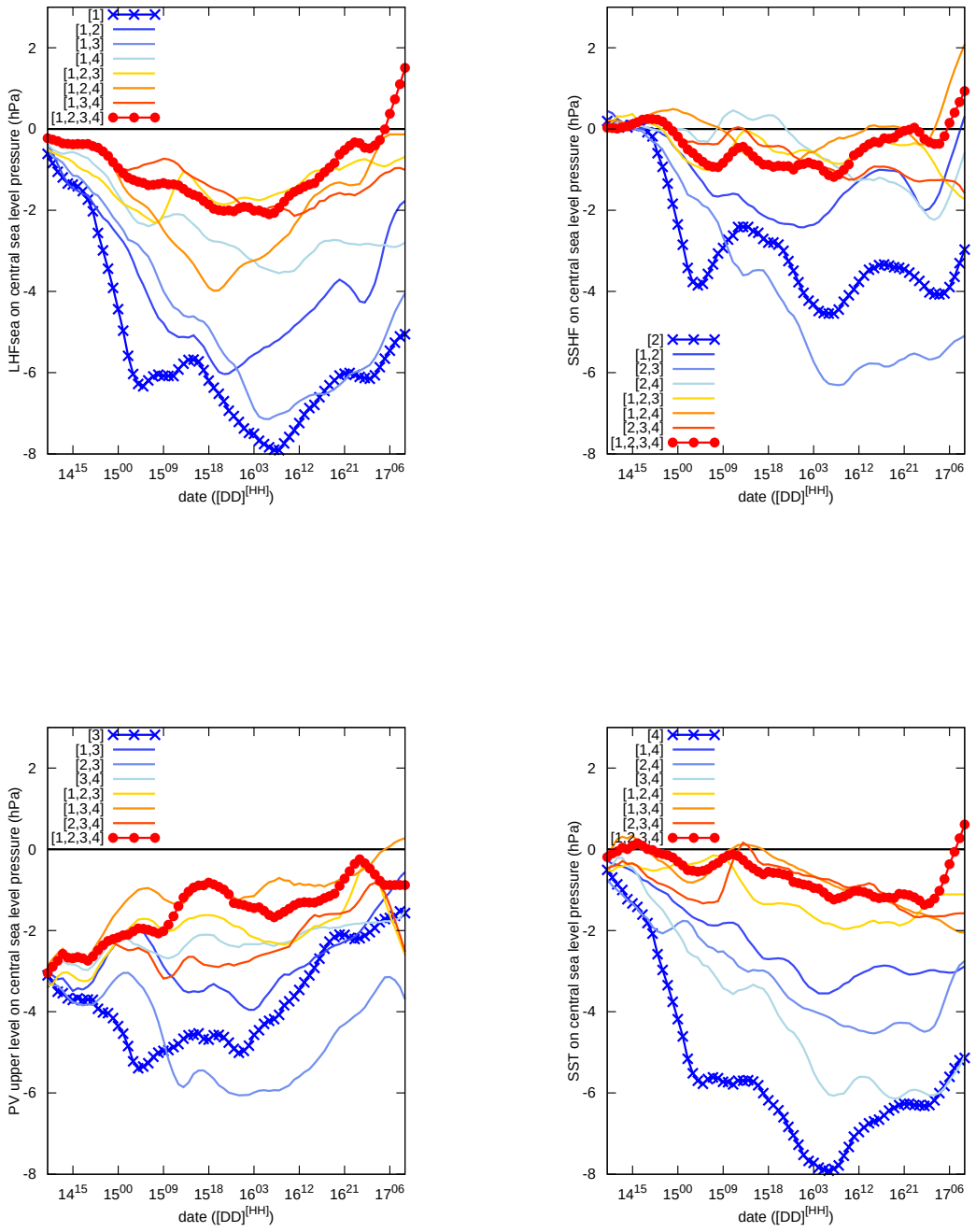

Figure 5.4.12: Collection-dependence of the 950116 case of the effects on the sea level pressure at the centre of the storm (hPa). LHF (top left), SSHF (top right), Upper level PV (bottom left), SST (bottom right). Results have been filtered with a mobile average filter of five time steps. Legend of the lines follows same structure like in figure 5.4.11

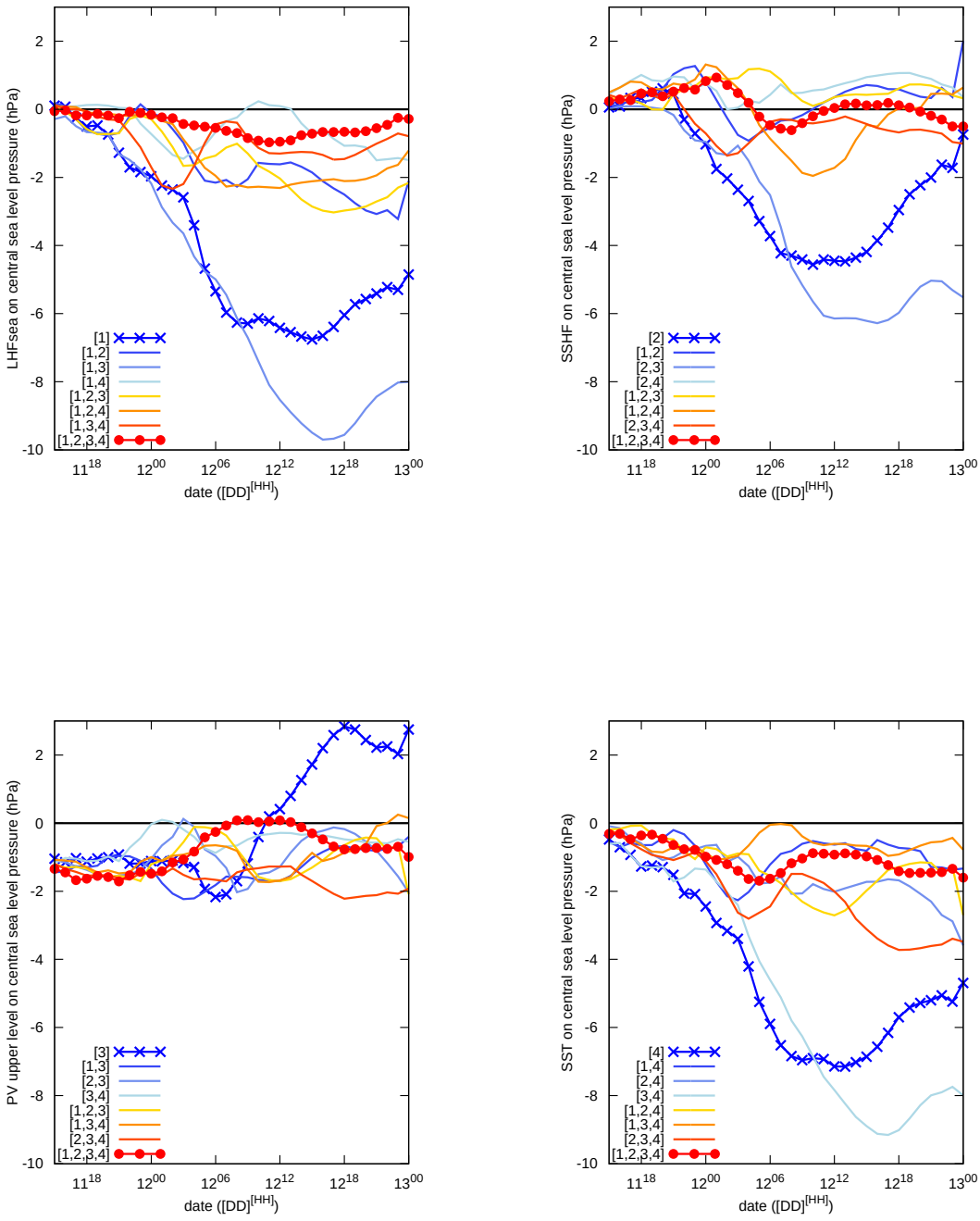

Figure 5.4.13: As in figure 5.4.12 but for the 960912 case (different scale)

the importance of the LHR on the enhancing role on upper level disturbances or on their influences in low-level disturbances (Hoskins et al., 1985; Davis and Emanuel, 1991).

In the sea level pressure value at the centre of the storm of the 950116 case, different 'goodness' are obtained (see figure 5.4.12). The four effects show anomalous dependence when they are obtained from a pair FS with the Upper level PV ($\{1,3\}$ curve in e_1(LHF effect), $\{2,3\}$ curve in e_2(SSHF effect), $\{3,4\}$ for e_4(SST effect), results that reflect some PV processes related to other factors not included in the study such as: PV diabatic generation due to the latent heat release on the strong and deep cloud formation into a medicane and/or Upper-low level PV interaction as a consequence of the baroclinic processes, and/or non PV related interactions between boundary layer and free layer, friction effects (related to efficiency of heat and moist transport from sea to cloud free layer driven by boundary layer). Secondary high sensitivity of the effectivity of the factors is obtained in the synergies with the SST factor ($\{1,4\}$ curve in e_1(LHF),$\{2,4\}$ curve in e_2(SSHF) $\{3,4\}$, $\{1,3,4\}$ curves in e_3(UPV), $\{1,4\}$ curve for e_4(SST)). Effects of SSHF factor show the lightest results during the mature phase of the medicane (between Jan. 15^{16} and 16^{05} UTC, figure 5.4.12). Giving a signature of the complex diabatic processes developed in the boundary layer of the storm like possible sea spray effect, and/or PBL processes related to strong turbulence, convection and winds poor influenced by the SSHF.

5.4.4 Temporal dependence

Effects on the pressure field of the cyclones are very diverse and depended strongly on the time step (see figures 5.4.15 to 5.4.17). From a general perspective, one can detect that 950116 and 030527 cases are different than 960912 case. These notorious differences might be related to the different nature of the cases: 950116 case shows a clear tropical-like structure (a clear and long-lasting central eye is observed see figure 5.1.2); 030527 case shows strong low-level vorticity, but an eye is not observed (see figure 5.1.6); 960912 case exhibits a clear eye (see figure 5.1.4), but for a short period of time (less than 5 hours, see table 5.1.a). These differences between the cloud structures of the storms could confirm the different nature of the systems. Meanwhile 950116 case would be mainly a system in which convection has strongly been self-organised around a vortex, 030527 case could reflect a major dominance of the baroclinic processes, and 960912 case could be the result of a combination of both processes. These aspects should be confirmed by the results.

Temporal evolution of the effects is divided in two phases in order to obtain a better understanding of the systems and as a way of summarise the results. This two-phase evolution is observed (see figure 5.4.15) as a change of the most relevant effects of the medicane evolution. First phase reached the formation of the system, meanwhile second phase reached mature state and dissipation. First phase is taken some time later of the

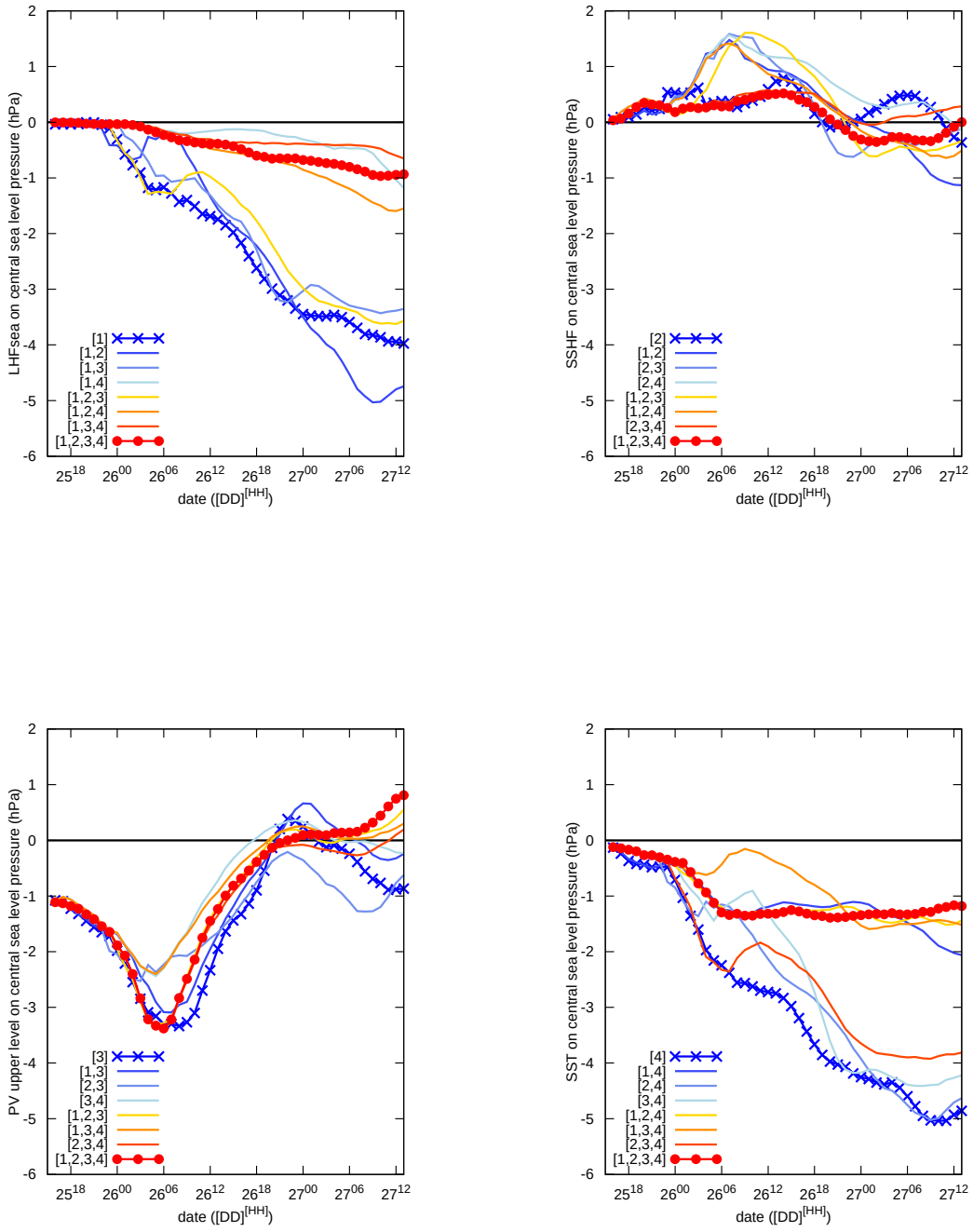

Figure 5.4.14: As in 5.4.12 but for the 030527 case (different scale)

Table 5.4.b: Phases of evolution of each medicane based on effect trends. Dates are in $[DD]^{[HH]}$ format

Medicane	Ist phase	IInd phase
950116	$14^{18} - 15^{17}$	$15^{18} - 17^{09}$
960912	$11^{22} - 12^{04}$	$12^{05} - 13^{00}$
030527	$26^{00} - 26^{11}$	$26^{12} - 27^{22}$

beginning of the simulations in order to avoid spin-up model processes and to make sure that the specific formation of the system is captured. Periods of the phases for each case are shown in the table 5.4.b. The total integrated effect per hour of each factor has been computed during each phase as a temporal integration of the effect at each time step divided for the length of the phase (negative and positive values is allowed, see results in tables 5.4.c, 5.4.d and 5.4.e). By this way is obtained a general idea of the mean role per hour of the effect during each phase.

There is a change of importance between the two phases. Meanwhile the fifth most important effects in the 3 variables (central sea level pressure, maximum azimuthally averaged horizontal wind speed at 950 hPa and relative vorticity at the centre of the storm) in the first phase are: $e_3, e_{24}, e_{14}, e_{134}$, on second phase they are: e_{14}, e_{123}, e_{124}, e_{134}. It is shown the dominance of the baroclinic evolution of the first phase (shown by strong role of e_3) as such as the triggering effect of the surface moist and heat fluxes derived from sea (factor number 4). Coinciding results of the polar low dynamics derived from a three-dimensional nonlinear geostrophic momentum model (Montgomery and Farrell, 1992). However, in second phase the evolution of the system is dominated by the heat of evaporation from the sea influenced by boundary layer and upper level disturbance (LHF as number 1 appeared in all the most important factors). Second phase reveal a more complex dynamics (triple synergies are important), as a possible reflection of the role of the air-sea mechanism. Some particularities for each case and variable can be given.

Effects on central pressure

During the formation phase, effects show a main clear enhancing role for the January 1995 case (2 cyclolitic of the 15 effects), meanwhile for May 2003 is not that clear (9 and 10). Results reveal that in selected cases the initial phase of the central sea level pressure effect is mainly driven by Upper level disturbance (effect e_3), the synergy between LHF and SST (effect e_{14}), synergy between SSHF and SST (e_{24}) and in lower degree by different synergies between the surface fluxes and SST. This dual dependence reflects the interaction between

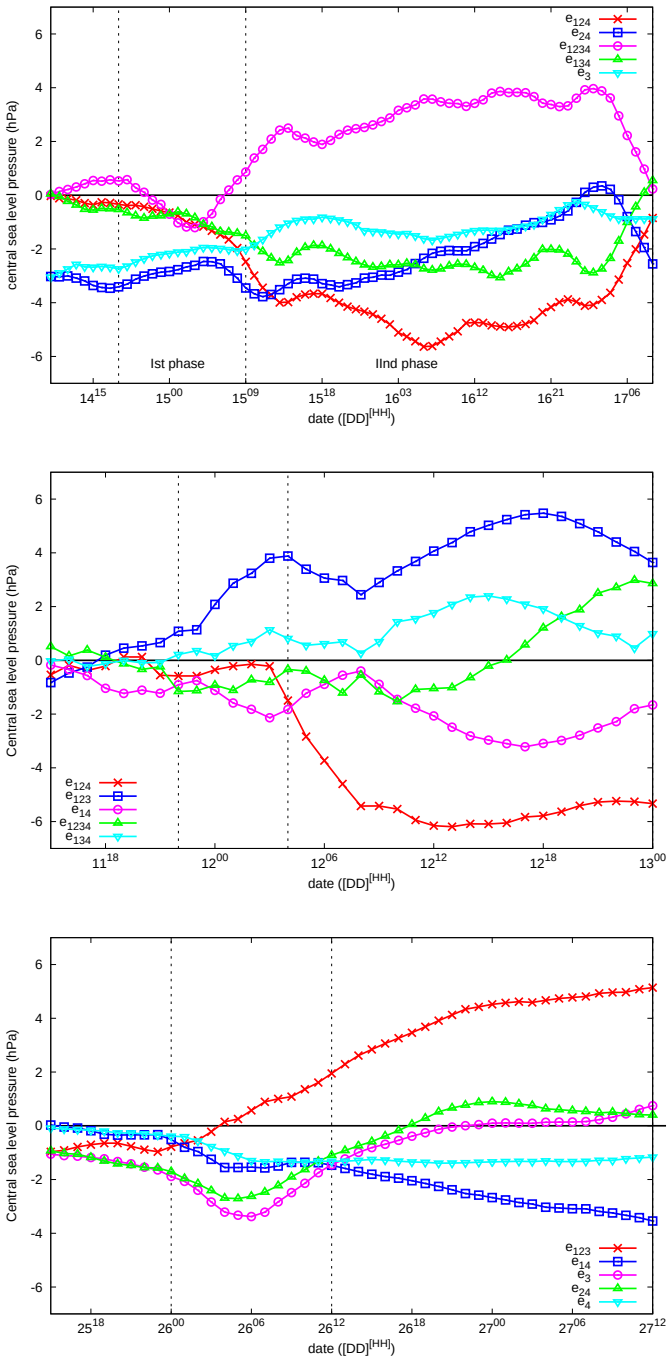

Figure 5.4.15: Temporal evolution of the fifth most important effects on the sea level pressure at the centre of the storm. January 1995 medicane (top), September 1996 medicane (middle) and May 2003 medicane (bottom). Results have been filtered with a mobile average filter of 5 time-steps (5 h). Vertical slashed lines mark each phase (labelled in top panel).

the baroclinic and diabatic sea surface induced processes assumed to be necessary for the formation of a medicane. Upper level disturbance as a way to enhance vorticity at the surface trough the baroclinic development and increasing vertical thermodynamic disequilibrium with the warm and moistened air above sea surface from which air-sea mechanism can be established in the Mediterranean area (Emanuel, 2005). The existence of a low level weak vortex has been shown as a necessary element from which a tropical-storm developed (Rotunno and Emanuel, 1987). This dynamical genesis aspect is shown by September 1996 case in which approaching movement of the upper level disturbance towards the zone of formation of the system (in which deep convection was developing, see figure 5.4.9) can be associated to a surface weak vortex around which convection is organised and the medicane is generated. Importance of the SST is a signature of its high influence on the heat and moist vertical transport in the boundary (as it is described in bulk parametrisation of the LHF and SSHF fluxes (Emanuel, 1986)) that acts as the initial source of heat and moisture for the convection. In all the cases, secondaries effects are synergies between SST, the LHF and SSHF fluxes. Some particular behaviours could be obtained from each case. The most clear is found in 030527 case a strong peak of the effectivity of the upper level disturbance (e_3 as line-circles in figure 5.4.15 on 26th at 06 UTC), could reflect a typical baroclinic Mediterranean role of the storm rather than a tropical like.

Secondary phases do not present a clear similarity between cases. Moreover, cyclogenetic and cyclolitic effects are present during this phase. Nevertheless, during this phase medicanes reached their mature state, but with the results of the three cases, one can not derive a general description of a medicane dynamics. Cyclones do not reflect the same effects with cyclogenetic/cyclolitic changes of some effects among episodes, and their stronger effects are different. January 1995 case reflect a multi-dependence during this phase. Double and triple synergies between the four different factors are the most important effects. This aspect could be a signature of the importance of the air-sea interaction for the development of the 950116 case. Different result is obtained for the September 1996 case. Instead synergies are still important effects, they exhibited a mixture of cyclolitic and cyclogenetic roles. This can be an indication of a short period of importance of the air-sea mechanism for the case. Bear in mind that in September 1996 case a cloud central free cloud area (eye) was only observed for few hours. May 2003 case does not show a similar dominance of the synergies like in the other two cases. A clear enhancing role is obtained from the SST and LHF. SST effect on the LHF (e_{14}, and the individual effect e_4 see table 5.4.c) is probably relevant because storm formation is mainly due to the moist fluxes from the sea, rather than as a consequence of a vertical disequilibrium as a combination of upper level disturbances and surface warm and moistened air. Important increasing in time cyclolitic role of the e_{123} effect is obtained for the three cases. Cyclolitic role of the e_{123} becomes stronger as more baroclinic-like is the storm (see significant differences between cyclolitic roles of the effect in table 5.4.c